ONE-DIMENSIONAL ANALYSIS OF HALL THRUSTER OPERATING MODES

Eduardo Ahedo
Pablo Martínez
Juan M. Gallardo

E.T.S.I. AERONAUTICOS
UNIVERSIDAD POLITECNICA DE MADRID
SPAIN

Contract number: F61775-00-WE034
Contracting Entity: EOARD-AFOSR
Final report, August 2001, version 2.

REPORT DOCUMENTATION PAGE

Form Approved OMB No. 0704-0188

Public reporting burder for this collection of information is estibated to average 1 hour per response, including the time for reviewing instructions, searching existing data sources, gathering and maintaining the data needed, and completing and reviewing this collection of information. Send comments regarding this burden estimate or any other aspect of this collection of information, including suggestions for reducing this burder to Department of Defense, Washington Headquarters Services, Directorate for Information Operations and Reports (0704-0188), 1215 Jefferson Davis Highway, Suite 1204, Arlington, VA 22202-4302. Respondents should be aware that notwithstanding any other provision of law, no person shall be subject to any penalty for failing to comply with a collection of information if it does not display a currently valid OMB control number. PLEASE DO NOT RETURN YOUR FORM TO THE ABOVE ADDRESS.

1. REPORT DATE (DD-MM-YYYY) 31-08-2001	2. REPORT TYPE Final	3. DATES COVERED (FROM - TO) 10-08-2000 to 10-08-2001

4. TITLE AND SUBTITLE One-Dimensional Analysis of Hall Thruster Operating Modes Unclassified	5a. CONTRACT NUMBER F61775-00-WEO34 5b. GRANT NUMBER 5c. PROGRAM ELEMENT NUMBER
6. AUTHOR(S) Ahedo, Eduardo ; Martinez, Pablo ; Gallardo, Juan M. ;	5d. PROJECT NUMBER 5e. TASK NUMBER 5f. WORK UNIT NUMBER
7. PERFORMING ORGANIZATION NAME AND ADDRESS Polytechnic University Madrid ETSI Aeronautics Plaza Cardenal Cisneros Madrid, Spain28040	8. PERFORMING ORGANIZATION REPORT NUMBER
9. SPONSORING/MONITORING AGENCY NAME AND ADDRESS EOARD PSC 802 BOX 14 FPO, 09499-0014	10. SPONSOR/MONITOR'S ACRONYM(S) 11. SPONSOR/MONITOR'S REPORT NUMBER(S)

12. DISTRIBUTION/AVAILABILITY STATEMENT
APUBLIC RELEASE
,

13. SUPPLEMENTARY NOTES

14. ABSTRACT

The very simplicity of the Hall thruster structure with no screens or other control surfaces makes it difficult to understand the interrelationships which, in the end, localize and shape the various plasma regions existing in the accelerating channel. Since the radial magnetic field is usually shaped with a peak near the channel exit, the plasma structure has often been explained as simply a reflection of the magnetic field distribution. However, this is inadequate to explain the plasma dynamics inside the accelerating channel. We develop a macroscopic model gathering reliability and clarity. Quantitative accuracy in the predictions is not the main goal. Instead, emphasis is given to the consistency of the governing equations and their boundary conditions, and to include enough basic physics to illuminate the complex interplay of phenomena which shape the Hall thruster plasma. A basic model is presented along with a supplementary model of the radial interaction of the plasma with the lateral walls of the thruster. An analysis is presented of the effects of the radial plasma/wall interactions on the basic steady-state solution. The effects of heat conduction and plasma oscillations are discussed.

15. SUBJECT TERMS
EOARD; Hall effect thruster; electric propulsion; spacecraft propulsion; modeling

16. SECURITY CLASSIFICATION OF:			17. LIMITATION OF ABSTRACT Public Release	18. NUMBER OF PAGES 105	19. NAME OF RESPONSIBLE PERSON Fenster, Lynn lfenster@dtic.mil
a. REPORT Unclassified	b. ABSTRACT Unclassified	c. THIS PAGE Unclassified			19b. TELEPHONE NUMBER International Area Code Area Code Telephone Number 703767-9007 DSN 427-9007

Standard Form 298 (Rev. 8-98)
Prescribed by ANSI Std Z39.18

REPORT DOCUMENTATION PAGE	Form Approved OMB No. 0704-0188

Public reporting burden for this collection of information is estimated to average 1 hour per response, including the time for reviewing instructions, searching existing data sources, gathering and maintaining the data needed, and completing and reviewing the collection of information. Send comments regarding this burden estimate or any other aspect of this collection of information, including suggestions for reducing the burden, to Department of Defense, Washington Headquarters Services, Directorate for Information Operations and Reports (0704-0188), 1215 Jefferson Davis Highway, Suite 1204, Arlington, VA 22202-4302. Respondents should be aware that notwithstanding any other provision of law, no person shall be subject to any penalty for failing to comply with a collection of information if it does not display a currently valid OMB control number.

PLEASE DO NOT RETURN YOUR FORM TO THE ABOVE ADDRESS.

1. REPORT DATE ***(DD-MM-YYYY)*** **31-Aug-2001**	**2. REPORT TYPE** Final Report	**3. DATES COVERED** *(From – To)* 8/10/2000 - 10-Aug-01

4. TITLE AND SUBTITLE One-Dimensional Analysis of Hall Thruster Operating Modes	**5a. CONTRACT NUMBER** F61775-00-WE034
	5b. GRANT NUMBER
	5c. PROGRAM ELEMENT NUMBER
6. AUTHOR(S) EDUARDO AHEDO, PABLO MARTINEZ, JUAN M. GALLARDO	**5d. PROJECT NUMBER**
	5d. TASK NUMBER
	5e. WORK UNIT NUMBER

7. PERFORMING ORGANIZATION NAME(S) AND ADDRESS(ES) POLYTECHNIC UNIVERSITY MADRID ETSI Aeronauticos Plaza Cardenal Cisneros Madrid 28040 Spain	**8. PERFORMING ORGANIZATION REPORT NUMBER** N/A
9. SPONSORING/MONITORING AGENCY NAME(S) AND ADDRESS(ES) EOARD PSC 802 BOX 14 FPO 09499-0200	**10. SPONSOR/MONITOR'S ACRONYM(S)**
	11. SPONSOR/MONITOR'S REPORT NUMBER(S) SPC 00-4034

12. DISTRIBUTION/AVAILABILITY STATEMENT

Approved for public release; distribution is unlimited.

13. SUPPLEMENTARY NOTES

14. ABSTRACT

The very simplicity of the Hall thruster structure with no screens or other control surfaces makes it difficult to understand the interrelationships which, in the end, localize and shape the various plasma regions existing in the accelerating channel. Since the radial magnetic field is usually shaped with a peak near the channel exit, the plasma structure has often been explained as simply a reflection of the magnetic field distribution. However, this is inadequate to explain the plasma dynamics inside the accelerating channel. We develop a macroscopic model gathering reliability and clarity. Quantitative accuracy in the predictions is not the main goal. Instead, emphasis is given to the consistency of the governing equations and their boundary conditions, and to include enough basic physics to illuminate the complex interplay of phenomena which shape the Hall thruster plasma. A basic model is presented along with a supplementary model of the radial interaction of the plasma with the lateral walls of the thruster. An analysis is presented of the effects of the radial plasma/wall interactions on the basic steady-state solution. The effects of heat conduction and plasma oscillations are discussed.

15. SUBJECT TERMS

Hall effect thruster, electric propulsion, spacecraft propulsion, modeling, EOARD

16. SECURITY CLASSIFICATION OF:			**17. LIMITATION OF ABSTRACT**	**18, NUMBER OF PAGES**	**19a. NAME OF RESPONSIBLE PERSON**
a. REPORT UNCLAS	**b. ABSTRACT** UNCLAS	**c. THIS PAGE** UNCLAS	UL	104	Ingrid Wysong
					19b. TELEPHONE NUMBER *(Include area code)* +44 (0)20 7514 4285

Standard Form 298 (Rev. 8/98)
Prescribed by ANSI Std. Z39-18

The Contractor, UNIVERSIDAD POLITECNICA DE MADRID, hereby declares that, to the best of its knowledge and belief, the technical data delivered herewith under Contract No F61775-00-WE034 is complete, accurate, and complies with all requirements of the contract.

August 31, 2001

Javier UCEDA
Vice President for Research
and Institutional Relations

I certify that there were no subject inventions to declare as defined in FAR 52.227-13, during the performance of this contract.

August 31, 2001

Javier UCEDA
Vice President for Research
and Institutional Relations

Contents

1 INTRODUCTION 1

2 FORMULATION OF THE 1-D MODEL 3
- 2.1 Model hypotheses and geometry . . . 3
- 2.2 Plasma macroscopic equations . . . 4
  - 2.2.1 The 2D axisymmetric equations . . . 5
  - 2.2.2 The approximate 1D axial model . . . 5
- 2.3 Collisional processes . . . 6
  - 2.3.1 The ionization rate . . . 6
  - 2.3.2 Charge-exchange collisions . . . 7
  - 2.3.3 Electron-neutral elastic collisions . . . 8
  - 2.3.4 Electron-ion collisions . . . 8
  - 2.3.5 Anomalous electron diffusion . . . 9
- 2.4 Equations for electrons . . . 9
  - 2.4.1 Electron current . . . 9
  - 2.4.2 Internal energy losses . . . 10
  - 2.4.3 Heat conduction . . . 11
- 2.5 Summary of axial equations . . . 12
  - 2.5.1 Plume divergence law . . . 12
- 2.6 The anode sheath . . . 13

3 BASIC STEADY-STATE SOLUTION 17
- 3.1 Governing equations . . . 17
  - 3.1.1 Singular/sonic points . . . 18
  - 3.1.2 Boundary conditions . . . 19
- 3.2 Types of solutions . . . 20
- 3.3 Structure of the plasma flow . . . 22
- 3.4 Thruster performances . . . 23
- 3.5 Asymptotic analysis . . . 24
- 3.6 Influence of control/design parameters . . . 26
- 3.7 Discussion . . . 29

4 THE RADIAL MODEL 39
- 4.1 Introduction . . . 39
- 4.2 Presheath/sheath model . . . 39

4.2.1 The presheath . . . 41
4.2.2 The sheath . . . 43
4.2.3 The charge saturation regime . . . 46
4.3 Wall-source terms in the axial model . . . 48
4.3.1 Particle losses . . . 48
4.3.2 Near-wall conductivity . . . 49
4.3.3 Energy losses . . . 50
4.4 Conclusions . . . 51

5 EFFECTS OF LATERAL LOSSES 56
5.1 Governing equations . . . 56
5.1.1 Frequencies for wall-source terms . . . 57
5.1.2 Singular points and boundary conditions . . . 58
5.2 Axial plasma structure . . . 59
5.3 Influence of control/design parameters . . . 60

6 EFFECTS OF HEAT CONDUCTION 72
6.1 Governing equations . . . 72
6.1.1 Singular points and boundary conditions . . . 72
6.1.2 Restriction on the ion backflow . . . 74
6.2 Solution for zero-ionization regions . . . 74
6.3 Plasma structure and thruster performances . . . 75

7 SELF-OSCILLATIONS 80
7.1 Perturbation equations . . . 80
7.2 Model of linear perturbations . . . 81
7.2.1 Boundary conditions . . . 82
7.2.2 Integration procedure . . . 83
7.3 Self-excited modes . . . 84

8 SUMMARY 91

A Expansion around sonic points 93
A.1 Stationary model . . . 93
A.1.1 Singular sonic point . . . 93
A.1.2 Regular sonic point . . . 93
A.2 Perturbation model . . . 95
A.2.1 Singular sonic point . . . 95
A.2.2 Regular sonic point . . . 95

Chapter 1

INTRODUCTION

The very simplicity of the Hall thruster structure with no screens or other control surfaces, makes it difficult to understand the interrelationships which, in the end, localize and shape the various plasma regions existing in the accelerating channel. Bishaev and Kim[1] distinguish, in their experiments i) an upstream diffusion region, with negligible electric field, no ion production, predominant ion motion towards the anode, and low plasma temperature; ii) an intense ionization layer, placed near the channel exit, with peaks of plasma density and temperature; and iii) an acceleration region, where most of the potential drop takes place, and extending outside the channel into iv) the plume. These characteristics of the plasma flow are confirmed by other experimental observations[2, 3] and by two-dimensional(2-D) plasma simulations[4]. Since the radial magnetic field is usually shaped with a peak near the channel exit, the above plasma structure has often been explained as simply a reflection of the magnetic field distribution.

V. Kim, in a recent review paper on Hall thruster physics[5], recognizes that there is still no model describing adequately the plasma dynamics inside the accelerating channel. The importance of developing a reliable model that improves our understanding of the factors which control plasma structure becomes evident when we attempt to improve upon existing Hall thruster designs, particularly regarding (i) thrust efficiency, (ii) erosion, and (iii) control of oscillations. Present design criteria are based mainly on testing experience. Erosion of the thruster walls is the main factor limiting the thruster lifetime. The erosion rate is governed by local plasma density, electron temperature, and sheath drop, and each of these may show order-of-magnitude variations within the channel making it crucial to have theoretical guidance for steering their peaks to the least damaging locations possible. Plasma self-oscillations are manifested by a modulation of the discharge current, which sometimes is fairly deep, but at other times it is much weaker or almost absent, and the reasons for these widely different and badly-predictable behaviors are not understood at present.

One-dimensional(1D) macroscopic models can be simple but powerful tools to understand the physics and parameters that govern the thruster response and to determine the basic scaling laws for thruster magnitudes. Furthermore, these fast-to-solve models can be the ideal complement to time-consuming PIC-MCC 2D simulations[6, 7], for Hall thruster design and analysis. In general, published 1D analyses (Refs. [8, 9, 10, 11] are some of them) put the emphasis on achieving satisfactory performance prediction which, if a few reasonable assumptions are introduced about the flow structure, is not too difficult to achieve (particularly regarding thrust).

However, these models fail to describe the whole plasma structure described by Bishaev and Kim, and, in general, the model formulation was not consistent enough.

In 1998, E. Ahedo and M. Martínez-Sánchez decided to develop and analyze a macroscopic model gathering reliability and clarity. Quantitative accuracy in the predictions should not be the main goal. Instead emphasis will be given to the consistency of the governing equations and their boundary conditions, and to include enough basic physics to illuminate the complex interplay of phenomena which shape the Hall thruster plasma. Preliminary results[12, 13] were promising and constitute the seed of the present Project.

We have organized the main body of this work in six chapters. In Chap. 2 we discuss the general formulation of the model, from the discussion of the phenomena to be included in the plasma equations and their function form to the geometry and unavoidable simplifications (in the plume treatment, for instance). In Chap. 3 we discuss the basic model, that is the model we think 'minimum' to reproduce the rich plasma structure described by Bishaev and Kim. In Chap. 4 we discuss a supplementary model of the radial interaction of the plasma with the lateral walls of the thruster. In Chap. 5 we analyze the effects of the radial plasma/wall interaction on the basic steady-state solution of Chap. 3. In Chap. 6 we solve a model that includes heat conduction effects (but no radial effects). Finally, In Chap. 7 we approach the problem of self-oscillations from a stability analysis of the steady-state plasma structure of Chap. 5.

Chapter 2

FORMULATION OF THE 1-D MODEL

2.1 Model hypotheses and geometry

Geometrical sketches of the thruster and the main features of the model are drawn in Figs. 2.1(a) and 2.1(b). The macroscopic model considers the plasma to be composed by three independent fluids: electrons (e), ions (i), and neutrals (n), and formulates equations for particle, momentum, and energy conservation of each species.

The channel is cylindrical of length L and has a constant radial area A_c (and radial thickness h_c); if x is the axial variable, we take $x_A = 0$ at the anode, and $x_E = L$ at the channel exit. The plume is modeled as a divergent cylindrical jet with a radial area $A(x)$, which will be determined as part of the solution. Electrons are injected into the plasma plume through a virtual cathode or neutralization surface (point P) placed at a distance $L_{EP}(= x_P - x_E)$ from the channel exit. The voltage difference between points A and P is the discharge voltage $V_d = \phi_A - \phi_P$.

The applied magnetic field is assumed radial

$$\boldsymbol{B}(x) = B(x)\boldsymbol{e}_r, \tag{2.1}$$

and its strength is such that ions can be assumed unmagnetized whereas electrons are strongly magnetized, and follow a quasi-closed drift motion across magnetic field lines.

The electron current delivered at the neutralization surface is the discharge current I_d. One part of this current diffuses inwards (into the near-plume and the channel) and ionizes the mass flow of neutrals, $\dot{m}$, injected at the anode. The other part of the electron current flows outwards (into the far plume) and neutralizes the ion current; subscript ∞ will refer to downstream conditions far away from the cathode. To facilitate this flow of electrons out of the cathode the voltage profile, $\phi(x)$, is expected to be minimum at point P. The voltage difference $\phi_\infty - \phi_P > 0$ can be interpreted as the cost of the electron emission.

Since the Debye length is generally very small (of the order of $10 - 100\mu$m) compared to the channel length, the plasma is considered quasineutral everywhere except in an electron-repelling sheath attached to the anode; this is region AB in Fig. 2.1(b), with point B marking the transition to the sheath. In this sheath, a self-adjusted potential bias,

$$\phi_{sh} = \phi_B - \phi_A > 0,$$

equates the electron thermal flow collected at the anode to the quasineutral diffusion flow of electrons across the thruster channel. We consider that only neutral gas is supplied externally through the anode. Then, since the anode sheath is thin and ion-attracting, ions must flow *into* the sheath from the quasineutral region adjacent to the anode. The presence of a region with reverse ion flow between the anode and the ionization layer is well reported in Refs. [1] and [5]. The reverse ion flow is recombined at the anode, and re-emitted as neutral gas to the channel, adding itself to the gas flow supplied externally.

The interaction of the plasma discharge with the lateral walls of the thruster makes the plasma flow two-dimensional (2D). Instead of tackling directly this 2D problem, which would require a sophisticated numerical procedure, our proposal is to solve separately two approximate 1D problems, for the axial and radial directions, and then, to couple them with adequate parameters and variables. The main 1D axial model will use variables averaged radially, and includes the interaction of the plasma with lateral walls through source terms for production/loss of particles, momentum and energy. The 1D radial model must provide the way to compute these source terms. Of course, this 1D + 1D procedure is not exact but presents the advantages of (i) to reduce the problem to conservation and ordinary differential equations, (ii) to lead to a quicker resolution, and (iii) to provide a lot of physical insight.

2.2 Plasma macroscopic equations

From the Boltzmann equation, the three basic macroscopic equations for a given plasma species (species subscript is omitted) are:

i) Particle conservation,

$$\frac{\partial n}{\partial t} + \nabla \cdot n\boldsymbol{v} = S. \tag{2.2}$$

ii) Momentum conservation,

$$m\frac{\partial n\boldsymbol{v}}{\partial t} + m\nabla \cdot (n\boldsymbol{v}\boldsymbol{v}) = -\nabla p + Zen(\boldsymbol{E} + \boldsymbol{v} \wedge \boldsymbol{B}) + \boldsymbol{M}. \tag{2.3}$$

iii) Energy conservation,

$$\frac{\partial}{\partial t}\Big(\frac{1}{2}nm\boldsymbol{v}^2 + \frac{3}{2}nT\Big) + \nabla \cdot \Big(\frac{1}{2}nm\boldsymbol{v}^2 + \frac{3}{2}nT\Big)\boldsymbol{v} + \nabla \cdot \boldsymbol{q} = -\nabla \cdot p\boldsymbol{v} + Zen\boldsymbol{v} \cdot \boldsymbol{E} + Q. \tag{2.4}$$

where: $\boldsymbol{v}$ is the macroscopic velocity; $\boldsymbol{q}$ is the conductive heat flux; S, $\boldsymbol{M}$, and Q represent external sources and collisional processes with other species; and other symbols are conventional. To complete these macroscopic equations, a transport equation for $\boldsymbol{q}$, and expressions for the three source terms must be specified.

From the above fundamental equations related equations of interest are:

– Velocity evolution,

$$mn\Big(\frac{\partial}{\partial t} + \boldsymbol{v} \cdot \nabla\Big)\boldsymbol{v} = -\nabla p + Zen(\boldsymbol{E} + \boldsymbol{v} \wedge \boldsymbol{B}) + \boldsymbol{M}', \tag{2.5}$$

with $\boldsymbol{M}' = \boldsymbol{M} - Sm\boldsymbol{v}$.

– Mechanical energy evolution,

$$n\Big(\frac{\partial}{\partial t} + \boldsymbol{v} \cdot \nabla\Big)\frac{1}{2}m\boldsymbol{v}^2 = -\boldsymbol{v} \cdot \nabla p + Zen\boldsymbol{v} \cdot \boldsymbol{E} + \boldsymbol{v} \cdot \boldsymbol{M} - Sm\boldsymbol{v}^2. \tag{2.6}$$

– Mechanical energy conservation,

$$\frac{\partial}{\partial t}\Big(\frac{1}{2}nm\boldsymbol{v}^2\Big)+\nabla\cdot\Big(\frac{1}{2}nm\boldsymbol{v}^2\boldsymbol{v}\Big)=-\boldsymbol{v}\cdot\nabla p+Zen\boldsymbol{v}\cdot\boldsymbol{E}+\boldsymbol{v}\cdot\boldsymbol{M}-\frac{1}{2}Sm\boldsymbol{v}^2. \tag{2.7}$$

– Internal energy conservation,

$$\frac{\partial}{\partial t}\Big(\frac{3}{2}nT\Big)+\nabla\cdot\Big(\frac{3}{2}nT\boldsymbol{v}\Big)+\nabla\cdot\boldsymbol{q}=-p\nabla\cdot v+Q', \tag{2.8}$$

with $Q'=Q-\boldsymbol{v}\cdot\boldsymbol{M}+\frac{1}{2}Sm\boldsymbol{v}^2$.

– Internal energy evolution,

$$n\Big(\frac{\partial}{\partial t}+\boldsymbol{v}\cdot\nabla\Big)\frac{3}{2}T+\nabla\cdot\boldsymbol{q}=-p\nabla\cdot v+Q'-\frac{3}{2}TS. \tag{2.9}$$

The set of conservation equations for all plasma species is completed with Poisson equation for the electric field $\boldsymbol{E}$ or the electric potential ϕ,

$$\epsilon_0\nabla\cdot\boldsymbol{E}=e\sum_{\alpha}Z_\alpha n_\alpha,\qquad\text{with}\qquad\boldsymbol{E}=-\nabla\phi. \tag{2.10}$$

2.2.1 The 2D axisymmetric equations

Assuming azimuthal symmetry, $\partial/\partial\theta=0$, and taking into account that the magnetic field is radial, the equations for the density, the velocity and the internal energy become

$$\frac{\partial n}{\partial t}+\frac{\partial}{\partial x}nv_x+\frac{1}{r}\frac{\partial}{\partial r}nrv_r=S, \tag{2.11}$$

$$mn\Big(\frac{\partial}{\partial t}+v_x\frac{\partial}{\partial x}+v_r\frac{\partial}{\partial r}\Big)v_x=-\frac{\partial nT}{\partial x}+Zen(E_x-Bv_\theta)+M'_x, \tag{2.12}$$

$$mn\Big(\frac{\partial}{\partial t}+v_x\frac{\partial}{\partial x}+v_r\frac{\partial}{\partial r}+\frac{v_r}{r}\Big)v_\theta=ZenBv_x+M'_\theta, \tag{2.13}$$

$$mn\Big(\frac{\partial}{\partial t}+v_x\frac{\partial}{\partial x}+v_r\frac{\partial}{\partial r}\Big)v_r-\frac{v_\theta^2}{r}=-\frac{\partial nT}{\partial r}+ZenE_r+M'_r, \tag{2.14}$$

$$\frac{\partial}{\partial t}\big(\frac{3}{2}nT\big)+\frac{\partial}{\partial x}\big(\frac{5}{2}nTv_x+q_x\big)+\frac{1}{r}\frac{\partial}{\partial r}r\big(\frac{5}{2}nTv_r+q_r\big)-v_x\frac{\partial}{\partial x}nT-\frac{v_r}{r}\frac{\partial}{\partial r}rnT=Q'. \tag{2.15}$$

2.2.2 The approximate 1D axial model

This is defined by assuming plasma variables independent of r and including the effects of radial boundaries as extra source terms in the axial equations. From Eqs. (2.11)-(2.15), the axial equations for the radially-averaged magnitudes (represented with a hat) are

$$\frac{\partial\hat{n}}{\partial t}+\frac{\partial}{\partial x}\hat{n}\hat{v}_x=\hat{S}+\hat{S}_w, \tag{2.16}$$

$$m\hat{n}\Big(\frac{\partial}{\partial t}+\hat{v}_x\frac{\partial}{\partial x}\Big)\hat{v}_x=-\frac{\partial\hat{n}\hat{T}}{\partial x}+Ze\hat{n}(\hat{E}_x-B\hat{v}_\theta)+\hat{M}'_x+\hat{M}'_{wx}, \tag{2.17}$$

$$m\hat{n}\Big(\frac{\partial}{\partial t}+\hat{v}_x\frac{\partial}{\partial x}\Big)\hat{v}_\theta=Ze\hat{n}B\hat{v}_x+\hat{M}'_\theta+\hat{M}'_{w\theta}, \tag{2.18}$$

$$\frac{\partial}{\partial t}\big(\frac{3}{2}\hat{n}\hat{T}\big)+\frac{\partial}{\partial x}\big(\frac{5}{2}\hat{n}\hat{T}\hat{v}_x+\hat{q}_x\big)-\hat{v}_x\frac{\partial}{\partial x}\hat{n}\hat{T}=\hat{Q}'+\hat{Q}'_w, \tag{2.19}$$

where $\hat{S}_w$, $\hat{M}'_{wx}$, $\hat{M}'_{w\theta}$, $\hat{Q}'_w$ represent the wall source terms. Notice that Eq.(2.14) is not used in the axial model.

In the cylindrical thruster, the convenient radial average for a generic magnitude f seems to be

$$\hat{f}(x,t) =< rf(r,x,t) >\equiv \frac{2}{r_2^2 - r_1^2}\int rf(r,x,t)dr, \tag{2.20}$$

where r_1 and r_2 are the inner and outer radius, respectively. Then, the wall-source terms take the form

$$\hat{S}_w = - < \frac{\partial}{\partial r} rnv_r >, \tag{2.21}$$

$$\hat{M}_{wx} = - < \frac{\partial}{\partial r}(rmnv_r v_x) >, \tag{2.22}$$

$$\hat{M}_{w\theta} = - < (\frac{1}{r} + \frac{\partial}{\partial r})(rmnv_r v_\theta) >, \tag{2.23}$$

$$\hat{Q}'_w = - < \frac{\partial}{\partial r} r\big(\frac{5}{2}nTv_r + q_r\big) - v_r \frac{\partial}{\partial r} rnT > . \tag{2.24}$$

2.3 Collisional processes

We discuss here the different collisional phenomena among the plasma species and the contributions they yield to terms S, $\boldsymbol{M}$, and Q', in Eqs.(2.16)-(2.19). Wall-source terms, Eqs.(2.21)-(2.24) will be discussed in Chap. 4.

2.3.1 The ionization rate

We consider that (i) ionization is produced by electron-neutral collisions exclusively, and (ii) we neglect double ionization (i.e., $Z_i = 1$). Here we look for an analytical expression of the ionization source term, which reproduces correctly enough its dependence with the electron temperature.

The ion production can be expressed as

$$S_i = n_e \nu_i \quad \nu_i = n_n R_i(T_e),$$

where $R_i(T_e)$ is the effective ionization rate. Since the dependence of R_i on the electron temperature is going to be crucial in shaping the ionization region, it is important to use a correct expression for it.

Assuming that the electron motion satisfies

$$|\boldsymbol{v}_e| \ll \sqrt{T_e/m_e}, \tag{2.25}$$

the electron distribution function can be taken local-Maxwellian,

$$f_e(E) = \Big(\frac{m_e}{2\pi T_e}\Big)^{3/2} \exp -\frac{E}{T_e},$$

where E is the electron energy. Then, the ionization rate can be written as

$$R_i(T_e) = \frac{8\pi}{m_e^2}\int_0^\infty \sigma_i(E) E f_e(E) dE, \tag{2.26}$$

where $\sigma_i(E)$ is the ionization cross-section.

To work with simple analytical expressions, $\sigma_i(E)$ (for xenon) is given by

$$\begin{aligned} \sigma_i(E) &= \sigma_{i0}\Big[1 - \exp(E/E_i - 1)\Big], \\ E_i &= 12.1 \text{ eV}, \quad \sigma_{i0} = 5 \times 10^{-20} \text{ m}^2, \end{aligned} \tag{2.27}$$

for $E > E_i$, and $\sigma_i(E) = 0$ for $E < E_i$; E_i is the energy for primary ionization. Figure 2.2(a) compares this expression with experimental values, showing that it is a good approximation for electron energies E up to 100eV, which is the range of interest for a Hall thruster.

Substituting $f_e(E)$ and $\sigma_i(E)$ in Eq. (2.26), one obtains

$$R_i(T_e) = \bar{\sigma}_i(T_e)\bar{c}_e, \qquad \text{with} \quad \bar{\sigma}_i(T_e) = \sigma_{i0}\Big(1 + \frac{T_e E_i}{(T_e + E_i)^2}\Big) \exp\Big(-\frac{E_i}{T_e}\Big), \tag{2.28}$$

and $\bar{c}_e = \sqrt{8T_e/\pi m_e}$. Figure 2.2(b) compares this expression of $\bar{\sigma}_i(T_e)$ with the one obtained numerically from experimental values of $\sigma_i(E)$. The agreement is very good up to $T_e \sim 40$eV and satisfactory up to $T_e \sim 100$ eV. Although it is easy to obtain better improvements with more accurate expressions of $\sigma_i(E)$, we find it worthless for the objectives of the present model.

The ionization frequency can be computed from

$$\nu_i \simeq \frac{n_n}{10^{20} \text{ m}^{-3}} \times \Big(\frac{T_e}{1 \text{ eV}}\Big)^{1/2} \times \frac{\tilde{\sigma}_i}{5 \times 10^{-20}\text{m}^2} \times 3.34 \times 10^6 \text{ s}^{-1}.$$

The neutral density of xenon ($m_i \simeq 2.19 \cdot 10^{-25}$kg) follows

$$n_n = \frac{\dot{m}}{m_i A v_n} \simeq \frac{\dot{m}}{1 \text{ mg/s}} \times \frac{10 \text{ cm}^2}{A} \times \frac{300 \text{ m/s}}{v_n} \times 1.47 \times 10^{19} \text{ m}^{-3}. \tag{2.29}$$

For the mass flow, the equivalences

$$1 \text{ mg/s} = 0.731 \text{ amp-eq}, \quad 1 \ \ \text{sccm} \simeq \frac{131}{22.4}\frac{\text{gr cm}^3}{\text{lit min}} \simeq 0.0975 \text{ mg/s},$$

can be useful.

Ionization produces a momentum exchange between ions and neutrals given by

$$\boldsymbol{M}_{in} = \pm m_i S_i \boldsymbol{v}_n. \tag{2.30}$$

2.3.2 Charge-exchange collisions

Charge-exchange collisions between ions and neutrals produce a momentum exchange given by

$$\boldsymbol{M}_{cx} = \pm m_i S_{cx}(\boldsymbol{v}_i - \boldsymbol{v}_n), \tag{2.31}$$

where the charge-exchange source term can be expressed as

$$S_{cx} = n_i \nu_{cx}, \quad \nu_{cx} = n_n c_{in} \sigma_{cx}, \tag{2.32}$$

with $c_{in} = |\boldsymbol{v}_i - \boldsymbol{v}_n|$ and σ_{cx} given by[14]

$$\sigma_{cx} \simeq \left[1 - 0.1 \ln\left(\frac{c_{in}}{1 \text{ km/s}}\right)\right]^2 \times 8.16 \times 10^{-19} \text{m}^2. \tag{2.33}$$

Computing the frequency for charge-exchange from

$$\nu_{cx} = \simeq \frac{n_n}{10^{20} \text{ m}^{-3}} \times \frac{c_{in}}{1 \text{km/s}} \times \frac{\sigma_{cx}}{5 \times 10^{-19} \text{m}^2} \times 5 \times 10^4 \text{ s}^{-1},$$

one finds that it is a secondary effect which can be neglected in the fundamental model of the plasma flow.

2.3.3 Electron-neutral elastic collisions

The electron-neutral collision frequency is expressed as

$$\nu_{en} = n_n \sigma_{en} \bar{c}_e,$$

with σ_{en} depending on T_e. Since these collisions are important only in the upstream part of the channel we just take

$$\sigma_{en} \simeq \text{const} = 27 \times 10^{-20} \text{ m}^2.$$

Using this average value one has

$$\nu_{en} \simeq \frac{n_n}{10^{20} \text{ m}^{-3}} \times \left(\frac{T_e}{1 \text{ eV}}\right)^{1/2} \times \frac{\sigma_{en}}{27 \times 10^{-20} \text{ m}^2} \times 1.78 \times 10^7 \text{ s}^{-1}.$$

Since, in general, $\sigma_i \ll \sigma_{en}$, the contribution of ionization collisions to ν_{en} is small.

2.3.4 Electron-ion collisions

The electron-ion collision frequency is expressed as[15, 16]

$$\nu_{ei} = \frac{2^{1/2} n_e Z^2 e^4 \ln\Lambda}{12\pi^{3/2} \epsilon_0^2 m_e^{1/2} T_e^{3/2}} = \left(\frac{n_e}{10^{18} \text{m}^{-3}}\right) \times \left(\frac{1 \text{ eV}}{T_e}\right)^{3/2} \times \ln\Lambda \times 2.9 \times 10^6 \text{ s}^{-1}. \tag{2.34}$$

with

$$\ln\Lambda \sim 9 + \frac{1}{2} \ln\left[\left(\frac{10^{18} \text{m}^{-3}}{n_e}\right) \left(\frac{T_e}{1 \text{ eV}}\right)^3 .\right]$$

Momentum exchange for ions and electrons is

$$\boldsymbol{M}_{ei} = \pm \nu_{ei} m_e n_e (\boldsymbol{v}_i - \boldsymbol{v}_e). \tag{2.35}$$

2.3.5 Anomalous electron diffusion

Near the channel exhaust, where the neutral density is low, classical collisions, $\nu_{ei} + \nu_{en}$, are insufficient to explain the plasma behavior observed there, which suggests the presence of an anomalous collisionality. There is controversy about which is the phenomenon responsible for that collisionality. Some authors[17, 11] suggest electron exchanges at lateral walls, but experimental data[9, 18] seems to favor Bohm diffusion. Anomalous diffusion due to electron interaction with lateral walls will be discussed in Chap. 5.

Bohm diffusion is usually included in electron momentum equation by adding to the frequency for classical collisions the Bohm diffusion frequency

$$\nu_{Bohm} = \alpha_B \omega_e,$$

with

$$\omega_e = \frac{eB}{m_e} \simeq \frac{B}{0.01 \text{ Tesla}} \times 1.758 \times 10^9 \text{ s}^{-1}$$

the electron gyro frequency, and α_B the Bohm parameter, with a classical empirical value of $\alpha_B \sim 1/16$. The Bohm diffusion frequency is computed from

$$\nu_{Bohm} = \frac{B}{0.01 \text{ Tesla}} \times 16\alpha_B \times 1.1 \times 10^8 \text{ s}^{-1}.$$

2.4 Equations for electrons

2.4.1 Electron current

From Eq. (2.5), the electron velocity field follows

$$m_e n_e \frac{D\boldsymbol{v}_e}{Dt} \simeq -\nabla n_e T_e + e n_e \nabla\phi - e n_e \boldsymbol{v}_e \wedge \boldsymbol{B} + \boldsymbol{M}'_e + \boldsymbol{M}'_{we} \tag{2.36}$$

where

$$D/Dt \equiv \partial/\partial t + \boldsymbol{v}_e \cdot \nabla$$

is the substantial derivative,

$$\boldsymbol{M}'_e \simeq \boldsymbol{M}_e \simeq -m_e n_e (\nu_e \boldsymbol{v}_e - \nu_{ei} \boldsymbol{v}_i) \tag{2.37}$$

is the frictional force, and the collision frequency

$$\nu_e = \nu_{en} + \nu_{ei} + \nu_{Bohm}. \tag{2.38}$$

includes the different collisional processes; in Eq. (2.37) we assumed $\nu_i \ll \nu_e$ and $\nu_{en}\boldsymbol{v}_n \ll \nu_e \boldsymbol{v}_e$.

The conditions for a quasi-closed, diffusive motion of the electron fluid are

$$D/Dt \ll \nu_e \ll \omega_e. \tag{2.39}$$

The condition on the left, allows us to neglect inertia effects in Eq. (2.36), which becomes algebraic for the velocity field,

$$0 \simeq -\nabla n_e T_e + e n_e \nabla\phi - e n_e \boldsymbol{v}_e \wedge \boldsymbol{B} + m_e n_e(-\nu_e \boldsymbol{v}_e + \nu_{ei} \boldsymbol{v}_i). \tag{2.40}$$

This simplifies the problem greatly, since writing

$$0 \simeq \boldsymbol{F} - n_e \boldsymbol{v}_e \wedge e\boldsymbol{B} - m_e \nu_e n_e \boldsymbol{v}_e, \tag{2.41}$$

with

$$\boldsymbol{F} \equiv e n_e \nabla \phi - \nabla n_e T_e + \nu_{ei} m_e n_e \boldsymbol{v}_i$$

the total driving force, we can solve for the velocity field. Using the right condition in Eq.(2.39), the velocity components satisfy

$$0 \simeq \omega_e v_{xe} + \nu_e v_{\theta e}, \tag{2.42}$$

$$-F_x = m_e n_e (\omega_e v_{\theta e} - \nu_e v_{xe}) \simeq \omega_e m_e n_e v_{\theta e}, \tag{2.43}$$

$$F_r = \nu_e m_e n_e v_{re}, \tag{2.44}$$

where ω_e is the electron gyro-frequency. These equations show that the dominant electron motion is azimuthal and is due the $\boldsymbol{F} \wedge \boldsymbol{B}$ drift, whereas the axial motion is due to the drift generated by the magnetic field and the azimuthal frictional force. Solving Eqs. (2.42)-(2.43) for the axial component one has

$$n_e v_{xe} \simeq \frac{F_x}{m_e \nu_d}, \tag{2.45}$$

with

$$\nu_d \simeq \frac{\omega_e^2}{\nu_e} \tag{2.46}$$

the effective collision frequency for the electron axial motion; notice that $\nu_{ei} m_e n_e \boldsymbol{v}_i$ can be neglected in F_x.

More adequate than ν_d to evaluate the relevance of electron diffusion in the whole plasma response is going to be the frequency

$$\bar{\nu}_d = \frac{m_e}{m_i} \nu_d \simeq \frac{\omega_c^2}{\nu_e}, \tag{2.47}$$

where

$$\omega_c = \frac{eB}{\sqrt{m_e m_i}} \simeq \frac{B}{0.01 \text{ Tesla}} \times 3.585 \times 10^6 \text{ s}^{-1}$$

is the electron hybrid gyrofrequency. Estimates of $\bar{\nu}_d$ can be obtained from

$$\bar{\nu}_d = \left(\frac{B}{0.01 \text{ Tesla}}\right)^2 \left(\frac{10^7 \text{s}^{-1}}{\nu_e}\right) \times 1.29 \times 10^6 \text{ s}^{-1}. \tag{2.48}$$

2.4.2 Internal energy losses

Taking into account that $\nu_i \ll \nu_e$ and $m_e \ll m_i$, the term for internal energy losses, Eq. (2.8), can be reduced to

$$Q_e' \simeq -\boldsymbol{v}_e \cdot \boldsymbol{M}_e' + (Q_i + Q_{exc}). \tag{2.49}$$

The first term on the right is the Joule heating, which using Eqs.(2.43) and (2.46), satisfies

$$-\boldsymbol{v}_e \cdot \boldsymbol{M}'_e \simeq m_e n_e (\nu_e \boldsymbol{v}_e^2 - \nu_{ei} \boldsymbol{v}_e \cdot \boldsymbol{v}_i) \simeq m_e n_e \nu_e v_{\theta e}^2 \simeq m_e n_e \nu_d v_{xe}^2. \tag{2.50}$$

Ionization losses are

$$Q_i = -S_i E_i,$$

and Q_{exc} accounts for excitation energies that are lost by radiation. It is common to group ionization and excitation losses in a single term proportional to Q_i:

$$Q_i + Q_{exc} = -\alpha_i Q_i = -\nu_i n_e \alpha_i E_i,$$

with α_i given by

$$\alpha_i(T_e) \simeq 2 + \frac{1}{4} \exp \frac{2E_i}{3T_e},$$

according to Dugan *et al.*[19]. [However, in most of this work we will just take $\alpha_i = \text{const} = 2.5$.]

2.4.3 Heat conduction

To close the equations for electron dynamics, a transport equation is needed for the heat conduction term $\nabla \cdot \boldsymbol{q}_e$. The diffusive behavior of the electrons, expressed by condition (2.39) justifies the following diffusive law for $\boldsymbol{q}_e$ [20]

$$\frac{5}{2} p_e \nabla T_e + e \boldsymbol{q}_e \wedge \boldsymbol{B} + m_e \nu_e \boldsymbol{q}_e \simeq 0, \tag{2.51}$$

which can be expressed as

$$\boldsymbol{q}_e + \frac{\omega_e}{\nu_e} \boldsymbol{q}_e \wedge \boldsymbol{e}_r \simeq -K_0 \nabla T_e, \qquad K_0 = \frac{5 n_e T_e}{2 m_e \nu_e}. \tag{2.52}$$

The azimuthal and axial components of $\boldsymbol{q}_e$ satisfy

$$\begin{aligned} 0 &\simeq -\omega_e q_{xe} - \nu_e q_{\theta e}, \\ 0 &\simeq -\frac{5 p_e}{2 m_e} \frac{\partial T_e}{\partial x} + \omega_e q_{\theta e}, \end{aligned} \tag{2.53}$$

where from we have the following Fourier-like law for the axial component,

$$q_{xe} = -\frac{5 n_e T_e}{2 m_e \nu_d} \frac{\partial T_e}{\partial x}. \tag{2.54}$$

2.5 Summary of axial equations

Taking into account all the effects discussed above, the macroscopic equations for the axial dynamics of a weakly divergent jet of quasineutral plasma ($n_e \simeq n_i$) are

$$
\begin{aligned}
&\frac{\partial n_e}{\partial t} + \frac{1}{A}\frac{\partial}{\partial x}(A n_e v_{xi}) = n_e \nu_i + S_w, \\
&\frac{\partial n_e}{\partial t} + \frac{1}{A}\frac{\partial}{\partial x}(A n_e v_{xe}) = n_e \nu_i + S_w, \\
&\frac{\partial n_n}{\partial t} + \frac{1}{A}\frac{\partial}{\partial x}(A n_n v_n) = -n_e \nu_i - S_w, \\
&\frac{\partial}{\partial t}(m_i n_n v_n) + \frac{1}{A}\frac{\partial}{\partial x}(A m_i n_n v_n^2) = -m_i v_n n_e \nu_i + m_i (v_{xi} - v_n) n_e \nu_{cx} - m_i v_{nw} S_w, \\
&\frac{\partial}{\partial t}(m_i n_e v_{xi}) + \frac{1}{A}\frac{\partial}{\partial x}(A m_i n_e v_{xi}^2) = -e n_e \frac{\partial \phi}{\partial x} + m_i v_n n_e \nu_i - m_i (v_{xi} - v_n) n_e \nu_{cx} + m_i v_{xi} S_w, \\
&0 = e n_e \frac{\partial \phi}{\partial x} - \frac{\partial}{\partial x} n_e T_e - \nu_d m_e n_e v_{xe}, \\
&\frac{\partial}{\partial t}\left(\frac{3}{2} n_e T_e\right) + \frac{1}{A}\frac{\partial}{\partial x} A \left(\frac{3}{2} T_e n_e v_{xe} + q_{xe}\right) = n_e \left(\nu_d m_e v_{xe}^2 - T_e \frac{\partial v_{xe}}{\partial x} - \nu_i \alpha_i E_i\right) + Q'_{we}, \\
&\frac{\partial T_e}{\partial x} = -\frac{2 m_e \nu_d}{5 n_e T_e} q_{xe}.
\end{aligned}
\tag{2.55}
$$

The ion temperature and pressure have been neglected, based on the consideration that the region of ion production is thin and therefore $T_i \ll T_e$. Inside the channel $A(x)$ is constant and drops off from Eqs. (2.55), and the law $A(x)$ for the divergent area of the plasma plume is derived next.

2.5.1 Plume divergence law

The external plasma plume is considered a cylindrically divergent jet. with the same angle of divergence, δ, at the inner and outer boundaries. Thus the radial area, $A_(x)$, and thickness, $d(x) = r_2(x) - r_1(x)$, satisfy

$$
\frac{\partial}{\partial x} \ln A = \frac{\partial}{\partial x} \ln d = \frac{2}{d} \tan \delta, \tag{2.56}
$$

The simplest approximation[21] would be to assume $\delta = \text{const}$. Instead, experimental measurements by Pollard and Beiting[22] indicate that what remains practically constant (in the near-plume) is the radial velocity of expansion of the plume boundaries, which we will call c_p. This suggests a law

$$
\tan \delta = \frac{c_p}{v_{xi}}. \tag{2.57}
$$

The value for c_p will be discussed later for each particular model.

Of course, this 1-D model of the plume will be more correct the smaller is the divergent angle, that is the largest is the relative ion velocity at the thruster exhaust. Also, we expect the model to be correct only in the near-plume; far-plume profiles are computed with this model just to estimate the thrust and the thrust efficiency.

2.6 The anode sheath

The Debye sheath attached to the anode (region AB in Fig. 2.1) completes the 1-D model of the channel and defines two boundary conditions at point B for the quasineutral model. The sheath is needed to assure the continuity of the electric current from the channel to the anode. A space-charge field adjusts the potential jump in the sheath, $\phi_{sh} \equiv \phi_B - \phi_A$, to a value such that the flow of electrons reaching the anode is equal to the diffusive flow coming from the quasineutral channel.

In the distinguished limit $\lambda_D/L \to 0$, the problem in the sheath is quasisteady and collisionless. Conservation equations across the sheath are:

$$\begin{aligned}
&n_i v_{xi} = \text{const} = (n_i v_{xi})_B, \\
&\tfrac{1}{2} m_i v_{xi}^2 + e\phi = \text{const} = \tfrac{1}{2} m_i v_{xiB}^2 + e\phi_{sh}, \\
&n_e v_{xe} = \text{const} = (n_e v_{xe})_A, \\
&T_e \ln n_e - e\phi = \text{const} = T_{eB} \ln n_{eB} - e\phi_B, \\
&n_e v_{xe}\big(\frac{5}{2} T_e - e\phi\big) + q_{xe} = \text{const} = (\frac{5}{2} n_e v_{xe} T_e + q_{xe})_A.
\end{aligned} \tag{2.58}$$

Assuming a quasi-Maxwellian distribution with temperature T_{eB}, the diffusive fluxes of particles and energy deposited by electrons at the anode are

$$\begin{aligned}
(n_e v_{xe})_A &= -\frac{\bar{c}_{eB}}{4} n_{eB} \exp \frac{-e\phi_{sh}}{T_{eB}}, \\
\left(q_{xe} + \frac{5}{2} T_e n_e v_{xe}\right)_A &= 2 T_{eB} (n_e v_{xe})_A,
\end{aligned} \tag{2.59}$$

with $\bar{c}_{eB}$ the electron thermal velocity at B.

Then, the potential jump across the sheath, ϕ_{sh}, and the heat conduction at the sheath boundary, q_{xeB}, satisfy

$$\frac{e\phi_{sh}}{T_{eB}} = \ln \frac{\bar{c}_{eB}}{4|v_{xeB}|}, \tag{2.60}$$

$$\frac{q_{xeB}}{n_{eB} v_{xeB} T_{eB}} = \frac{e\phi_{sh}}{T_{eB}} - \frac{1}{2}. \tag{2.61}$$

The deposition of electrons and ions at the anode produces anode heating, which should be considered in the evaluation of thruster performances. The heat flow deposited by the electrons at the anode is

$$Q_{eA} = 2(T_e n_e |v_{xe}|)_B A_c.$$

Back-flowing ions are accelerated by the sheath and impinge the anode with a large kinetic energy. In the anode they are recombined and then are re-emitted to the channel with a much lower kinetic energy, of the order of the anode temperature. The heat flow deposited by the ions is

$$Q_{iA} \simeq \frac{1}{2} m_i v_{xiA}^2 n_{eB} |v_{xiB}| A_c = (\frac{1}{2} m_i v_{xiB}^2 + e\phi_{sh}) n_{eB} |v_{xiB}| A_c. \tag{2.62}$$

Thus, the total heat flow to the anode is

$$Q_A = Q_{iA} + Q_{eA} \simeq T_{eB} n_{eB} A_c \Big[2|v_{xeB}| + (\frac{5}{6} + \ln \frac{\bar{c}_{eB}}{4|v_{xeB}|}) |v_{xiB}|. \Big] \tag{2.63}$$

The internal structure of the sheath is obtained from the integration of Poisson equation with the aid of the above conservation equations. Boundary conditions for Poisson equation are:

i) in the sheath scale, the electric field is zero at the presheath/sheath transition,

$$\left. \frac{d(e\phi/T_e)}{d(x/\lambda_D)} \right|_B \to 0. \tag{2.64}$$

ii) $\phi_A = 0$.

A first integral of Poisson equation is

$$\frac{\epsilon_0}{2} \left(\frac{d\phi}{dx} \right)^2 = U(e\phi) - U(e\phi_B), \tag{2.65}$$

where,

$$U(e\phi) = n_e T_e + m_i n_i v_{xi}^2 \tag{2.66}$$

is known as the Sagdeev's potential and condition (2.64) has been applied. At point B, the quasineutrality condition yields

$$U(e\phi)'_B = n_{eB} - n_{iB} = 0.$$

Therefore, for a valid solution to exist around point B, Eq. (2.65) requires

$$U''_B \equiv \frac{n_{eB}}{T_{eB}} - \frac{n_{iB}}{m_i u_{iB}^2} \geq 0,$$

that is

$$v_{xiB}^2 \geq \frac{T_{eB}}{m_i}, \tag{2.67}$$

which is known at Bohm condition. Conditions (2.60), (2.61), and (2.67) are boundary conditions for the quasineutral plasma at point B.

Finally, we point out that a 1-D model of the sheath and the region around it is an idealized situation, since, in general, the gas is ejected from a small orifice into the channel, yielding a two-dimensional potential distribution.

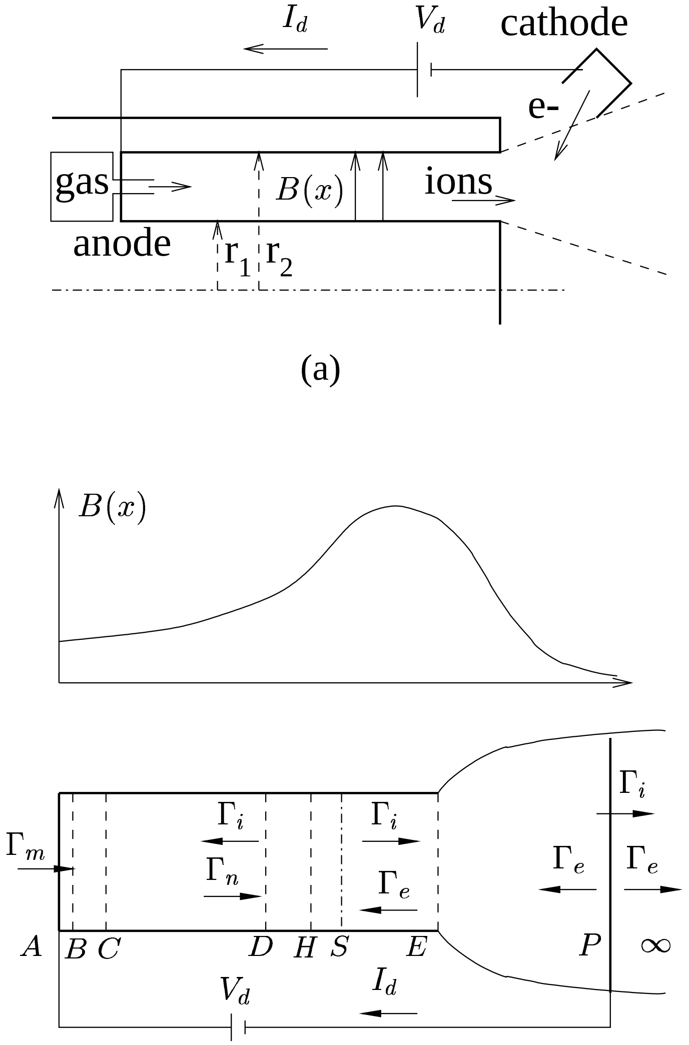
I_d
V_d
cathode
e-
gas
$B(x)$
ions
anode
r_1
r_2
$B(x)$
Γ_m
Γ_i
Γ_n
Γ_i
Γ_e
Γ_i
Γ_e
Γ_e
A
B
C
D
H
S
E
P
∞
V_d
I_d

(a)

(b)

Figure 2.1: Sketches of (a) the Hall thruster and (b) the 1D macroscopic model. $B(x)$ is the magnetic field profile; V_d is the discharge voltage; I_d the discharge current; $\dot{m}$ the flow of neutral gas; $\Gamma_\alpha = n_\alpha v_\alpha A, (\alpha = i, e, n, ...)$ are particle flows of the different species. Surface P is the cathode (beam neutralizer). For usual operating conditions the following plasma regions will be identified: anode sheath (AB), anode presheath (BC), diffusion region (CD), ionization layer (DH), internal acceleration region (HE), near-plume (EP), and far-plume (P∞). Point B is a singular sonic point for the reverse ion flow and point S is a regular sonic point of the forward ion flow.

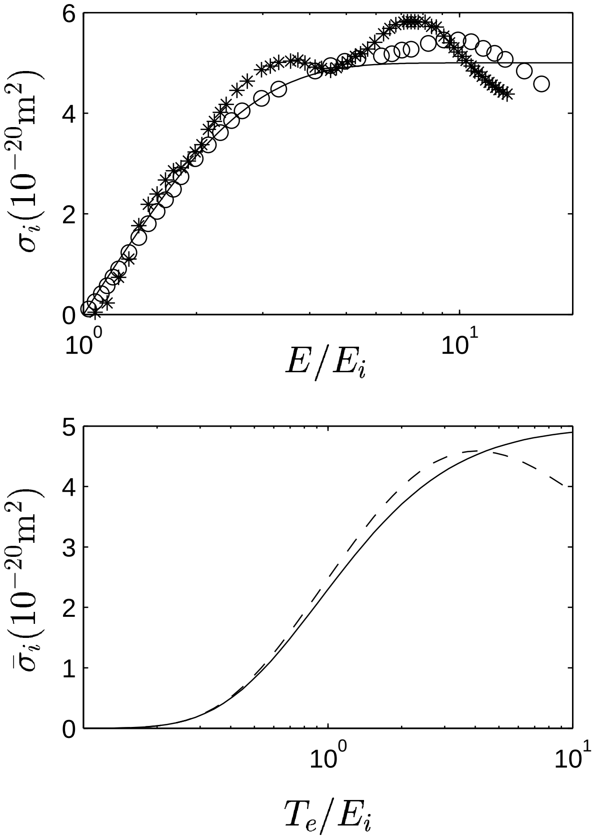

Figure 2.2: Individual (σ_i) and collective ($\bar{\sigma}_i$) cross-section for single-ionization of xenon by electron impact; E is the energy of an individual electron and T_e is the temperature of the Maxwellian electron distribution. Asterisks and circles are experimental values taken from Refs. [23] and [24], respectively. The dashed line for $\bar{\sigma}_i$ corresponds to the integration of the (average) experimental points of $\sigma_i(E)$. Solid lines represent the analytical fittings given by Eqs.(2.27) and (2.28) for $\sigma_{i0} = 5 \times 10^{-20}\mathrm{m}^2$.

Chapter 3

BASIC STEADY-STATE SOLUTION

3.1 Governing equations

We make here the following simplifications on the axial model:

(i) steady-state solution: $\partial/\partial t = 0$
(ii) no wall losses: $S_w, Q'_{we}, \boldsymbol{M}_w = 0$
(iii) no ion-electron collisions: $\nu_{ei} = 0$
(iv) no charge-exchange collisions: ν_{cx}
(v) no heat conduction $\boldsymbol{q}_e = 0$
(vi) The axial profile of the magnetic field is taken Gaussian,

$$\boldsymbol{B} = B\boldsymbol{e}_r, \quad B(x) = B_m \exp\Big[-\frac{(x-x_m)^2}{L_m^2}\Big], \tag{3.1}$$

with B_m, x_m, and L_m constants, and x_m close to x_E.

Then, Eqs.(2.55) simplify into

$$\begin{aligned}
&\frac{d}{dx}(An_e v_{xi}) = \frac{d}{dx}(An_e v_{xe}) = -\frac{d}{dx}(An_n v_n) = An_e\nu_i,\\
&v_n = \text{const},\\
&m_i v_{xi}\frac{dv_{xi}}{dx} = -e\frac{d\phi}{dx} - \nu_i m_i(v_{xi} - v_n),\\
&0 = en_e\frac{d\phi}{dx} - \frac{d}{dx}n_eT_e - \nu_d m_e n_e v_{xe},\\
&v_{xe}\frac{d}{dx}\big(\frac{3}{2}T_e\big) = -T_e\frac{dv_{xe}}{dx} + \nu_d m_e v_{xe}^2 - \nu_i\big(\alpha_i E_i + \frac{3}{2}T_e\big).
\end{aligned} \tag{3.2}$$

These equations are completed with Eq. (2.57) for the variation of the radial area, $a = \ln d = \ln A + \text{const}$, in the plume.

Using the particle axial flows of the different species as $\Gamma_\alpha = An_\alpha v_{x\alpha}$, the mass flow and the discharge current are written as

$$\begin{aligned}
\dot{m} &= m_i\Gamma_m, & \Gamma_m &= \Gamma_i + \Gamma_n,\\
I_d &= e\Gamma_d, & \Gamma_d &= \Gamma_i - \Gamma_e.
\end{aligned}$$

Then, continuity equations show that these two magnitudes are constant along the plasma jet (except for Γ_d dropping abruptly to zero at the cathode). Notice that $\dot{m}$ includes only the gas flow delivered at the anode. Another useful equation, derived from Eqs.(3.2), is the ambipolar momentum equation

$$\frac{d}{dx}(Am_i n_e v_{xi}^2) + A\frac{d}{dx}(n_e T_e) = An_e(\nu_i m_i v_n - \nu_d m_e v_{xe}). \tag{3.3}$$

Finally, important ratios for a discussion of the plasma response are (i) the ratio between the discharge current and the emitted gas flow,

$$i_d = \frac{m_i I_d}{e\dot{m}} \equiv \frac{\Gamma_d}{\Gamma_m}, \tag{3.4}$$

and (ii) the local ion current fraction,

$$\eta_i(x) = \Gamma_i(x)/\Gamma_m. \tag{3.5}$$

The propellant utilization is defined as $\eta_u = \eta_{i\infty}$. For $i_d > 1$ (the usual case in practice) η_u can be near unity[17]; in this case, i_d^{-1} coincides with the electrical efficiency $\Gamma_{i\infty}/\Gamma_d$. However, for $i_d < 1$, the maximum propellant utilization can be just i_d.

3.1.1 Singular/sonic points

We discuss now the properties of the mathematical model. Solving Eqs.(3.2) for the spatial derivatives we obtain a matrix equation of the form

$$(1 - M^2)\frac{d\boldsymbol{Y}}{dx} = \boldsymbol{F}(\boldsymbol{Y}), \tag{3.6}$$

where $\boldsymbol{Y} = (n_e, v_{xi}, T_e, ...)$ groups 7 plasma variables, $\boldsymbol{F}$ is a regular function (different from the one in the zero conduction model), and M is the isentropic Mach number,

$$M = \frac{v_{xi}}{\sqrt{5T_e/3m_i}}. \tag{3.7}$$

For instance, the equations for n_e and v_{xi} are

$$\begin{aligned} \frac{dn_e}{dx} &= n_e\frac{G}{P}, \\ \frac{dv_{xi}}{dx} &= \nu_i - v_{xi}\Big(\frac{G}{P} + \frac{da}{dx}\Big), \end{aligned} \tag{3.8}$$

with

$$\begin{aligned} P &= T_e - \frac{3}{5}m_i v_{xi}^2 \equiv T_e(1 - M^2), \\ v_{xe}G \equiv \bar{G} &= \nu_i\Big[\frac{2}{5}\alpha_i E_i + T_e - \frac{3}{5}m_i v_{xe}(2v_{xi} - v_n)\Big] - \nu_d m_e v_{xe}^2 + \frac{3}{5}m_i v_{xi}^2 v_{xe}\frac{da}{dx}. \end{aligned} \tag{3.9}$$

Therefore, the spatial problem may present singular points where the Mach number is equal to -1 or +1. The definition of an ion Mach number is *natural* to the macroscopic approach adopted to describe plasma dynamics. It characterizes the propagation of pressure perturbations, and clarifies, therefore, the interpretation of the steady and unsteady plasma responses. Sonic points are *regular* or *singular* depending on G being equal or not to zero at them. In a *singular sonic point* the derivatives of all plasma variables become infinite, so it is a turning point of spatial profiles. These points are admissible only at the boundaries of the quasineutral channel. On the contrary, in *a regular sonic point* the ion flow changes smoothly from subsonic to supersonic, like in the classical problem of a convergent-divergent nozzle. The expansion of the ion beam from the channel into the rarefied ionosphere implies that the ion flow will be sonic or supersonic at the channel exit (point E). Therefore, a forward sonic point –point S in Fig. 2.1(b)– with $M_S = 1$ is always expected in the channel. For a choked exit, point S is singular and coincides with point E. For a supersonic exit, point S is regular and its position within the channel must be determined as part of the solution.

3.1.2 Boundary conditions

The integration of Eqs. (3.2) between points B and P require seven boundary conditions, which are distributed between points B, S, E, and P$^-$. Taking into consideration the singular points, the sheath conditions discussed in Sec.2.6 and the parameters that are controlled experimentally, a *natural* set of boundary conditions is the following

i)-ii) The externally supplied mass flow rate $\dot{m}$ and the neutral velocity v_{nA} are known.

iii) The electron temperature at the cathode, T_{eP}, (of the order of the electron emission temperature) is known.

iv) The discharge voltage $V_d = \phi_A - \phi_P$ is known.

v) The quasineutral solution in the channel requires that $-M_B \leq 1$ [were $-M_B > 1$, there would be a point within the channel with $M = -1$ and $G = 0$, which is not possible, as the solution will make evident.] On the other hand, the Bohm condition (2.67) at the sheath entrance states that $-M_B \geq \sqrt{3/5}$. Here, we will assume that the sheath transition occurs at the singularity of the quasineutral solution, that is

$$M_B = -1. \tag{3.10}$$

vi) The voltage difference at the sheath satisfies Eq. (2.60). (Placing the arbitrary origin of ϕ at point A, one has $\phi_B = \phi_{sh}$ and $\phi_P = -V_d$). Using Eq.(3.10), Eq.(2.60) becomes

$$\frac{e\phi_{sh}}{T_{eB}} = \ln\left(\frac{\Gamma_{iB}}{\Gamma_{eB}}\sqrt{\frac{3m_i}{10\pi m_e}}\right). \tag{3.11}$$

vii) For the *supersonic exit regime*, sonic point S is regular:

$$G_S = 0 \quad \text{at} \quad M_S = 1. \tag{3.12}$$

Instead, for the *choked exit regime* we set that the flow at point E is sonic:

$$M_E = 1. \tag{3.13}$$

For the velocity of radial expansion in the plume, Eq. (2.57), we make the choice

$$c_p = \sqrt{\frac{5T_{eE}}{3m_i}}. \tag{3.14}$$

Apart from V_d, $\dot{m}$, and T_{eP}, other input variables are v_{nA}, L, L_{EP}, A_c and the profile of the magnetic field, Eq.(3.1). The main output variables of the model are the discharge current I_d, the relative ion reverse flow η_{iB}, the position x_S of the sonic point S (for a supersonic exit), the plume divergence profile, the thrust, and the thrust efficiency.

The continuation of the solution from point P to ∞ is straightforward. It just requires us to modify the electron current at point P$^+$, setting $\Gamma_{eP}^+ = \Gamma_{iP}$, in order that the net electric current in the plume far-field be zero.

3.2 Types of solutions

It is convenient to use dimensionless variables and parameters to integrate the equations and to characterize the solutions. Three magnitudes are enough to nondimensionalize Eqs.(3.2). The energy $T_* = E_i$, the cross-section $\sigma_* = \sigma_{i0}(m_i/m_e)^{1/2}$, and a typical particle flow Γ_* are the best choice. Then, magnitudes related to these three are

$$v_* = \sqrt{T_*/m_i}, \quad n_* = \Gamma_*/A_c v_*, \quad l_* = 1/n_*\sigma_*, \quad \nu_* = v_*/l_*.$$

When necessary, dimensionless magnitudes will be represented by an over-tilde over the respective dimensional ones. We omit to write down the dimensionless form of plasma equations, which is immediate.

The dimensionless form of Eqs. (3.2) is integrated as an initial-value problem with a Runge-Kutta algorithm. We focus the discussion here in the region between points B and P, the continuation to the far-plume being straightforward. The use of the auxiliary variable ξ, defined by

$$dx/d\xi = P,$$

instead of x, avoids unnecessary numerical problems in reaching or departing from singular sonic points, like point B. However, this does not solve the crossing of regular sonic point S in the supersonic-exit regime. A Taylor expansion of Eqs. (3.2) is needed to determine the derivatives of the plasma variables there; the details of that expansion are omitted here.

Due to the character of point S, the less time-consuming procedure is clearly to integrate from the neighborhood of point S towards points B and P separately. At point B, the integration stops where condition $M_B = -1$ is reached; at point P, it ends where $T = T_{EP}$. This initial-value procedure requires setting all variables at point S. For the choked-exit regime, this implies taking output parameters η_{iS}, i_d, and $\tilde{T}_{eS}$ as initial parameters, while input parameters $\tilde{V}_d$, $\tilde{x}_A$, and $\tilde{x}_P$ are outputs of the integration. For the supersonic-exit regime, output parameters i_d, η_{iS}, and $\tilde{x}_S$ are used as initial parameters, and $\tilde{T}_{eS}$ comes from condition $G_S = 0$; as before, input parameters $\tilde{V}_d$, $\tilde{x}_A$, and $\tilde{x}_P$ are outputs of the integration. A subsequent iteration is needed to adjust these input parameters to their desired values.

In addition, not all sets of 'initial parameters' lead to valid solutions. A first restriction to these parameters comes from the condition that the plasma flow be accelerating at point

S: $dv_{xi}/dx|_S > 0$. For a supersonic-exit solution this means choosing the appropriate set of derivatives from the two solutions given by the Taylor expansion. For a choked-exit solution it reduces the region of valid parameters to those satisfying

$$\bar{G}_S^- > 0 \quad \text{and} \quad \bar{G}_S^+ < 0; \tag{3.15}$$

observe in Eq. (3.9) that the difference between $\bar{G}_S^+$ and $\bar{G}_S^-$ is due to the term containing $da/dx \propto (\tan\delta)/d$.

A second restriction to 'initial parameters' at point S comes from the fact that there are solutions departing from S$^-$ towards B, which never reach a negative ion velocity and finish instead in a singular point with $M = +1$. These solutions are disregarded since they have no physical meaning for the plasma in a conventional Hall thruster. The limit condition $\Gamma_{iB} \simeq 0$ is going to be very important since it is going to indicate a real physical condition for the disappearance of steady solutions.

Figure 3.1 illustrates, in the parametric plane $(\tilde{T}_{eS}, \eta_{iS})$ and for two values of i_d, Eq.(3.4), the different solutions that are obtained from the integration between points S and B. Four parametric regions are found: *region 1*, with $\bar{G}_S^- < 0$, and *region 2*, with $\bar{G}_S^- > 0$ and $\eta_{iB} > 0$, are forbidden regions for the reasons exposed above; *region 3*, with $\bar{G}_S^- > 0$ and $\eta_{iB} < 0$, corresponds to the *choked-exit regime*; and (line) *region 4*, with $G_S = 0$ and $\eta_{iB} < 0$, corresponds to the *supersonic-exit regime*. For the choked-exit regime, the continuity of the solutions into the plume requires that $\bar{G}_S^+ < 0$, Eq.(3.15). Figure 3.1 depicts the limit line $\bar{G}_S^+ = 0$ for two values of $(\tan\delta)/\tilde{d}$.

For $i_d = 1.25$, region 4 of supersonic-exit solutions consists of high and low ionization branches. The low-ionization branch yields propellant utilizations well below 50% and corresponds, then, to inefficient thruster operation. Since, in addition, it does not lead to different plasma dynamics than the high-ionization branch, it will be disregarded hereafter in this paper. The high-ionization branch is actually a near-total ionization branch and corresponds to the near-complete ionization mode referred by Morozov *et al.*[17]. Notice that, since $\eta_{iS} \simeq 1$, point S must be placed near the downstream end of the ionization layer (point H in Fig. 2.1). As i_d increases from 1.25, the line $\eta_{iB} \simeq 0$ (separating regions 3 and 4 from region 2) moves left, towards lower T_{eS}, and region 2 disappears eventually (at $i_d \sim 1.65$ for the case of Fig. 3.1). For the same reason, as i_d decreases from 1.25 the line $\eta_{iB} \simeq 0$ moves right and restricts, in particular, the domain of supersonic-exit solutions with large ionization. For $i_d \leq 1$, two features are to be pointed out: first, the high-ionization branch of the supersonic-exit regime, instead of approaching the asymptotic line $\Gamma_{iS} = \Gamma_d$ (i.e., $\eta_{iS} = i_d$), disappears; second, the line $\eta_{iB} \simeq 0$ forbids choked-exit solutions with large ionization and moderate temperatures.

The presence and characteristics of the two supersonic-exit branches can be explained from the analytical expression of $G_S = 0$. From Eq.(3.9), that condition yields

$$\frac{3\Gamma_{iS}}{5\Gamma_m}(\Gamma_m - \Gamma_{iS})\frac{(2\Gamma_d - \Gamma_{iS})T_{eS} + (2/5)\Gamma_{iS}\alpha_i E_i}{T_{eS}(\Gamma_d - \Gamma_{iS})^2} \simeq \frac{\bar{\nu}_{dS}}{\nu_i^*}, \tag{3.16}$$

with $\bar{\nu}_d = \nu_d m_e/m_i$ and $\nu_i^* = n_{nA}R_i(T_{eS})$, and this last magnitude is of the order of the maximum ionization frequency in the channel. Then, for plasmas satisfying

$$\bar{\nu}_{dS} \ll \nu_i^*, \tag{3.17}$$

it is readily seen that Eq.(3.16) is verified by two types of solutions: the low-ionization branch with $\Gamma_{iS} \ll \Gamma_m$; and the near-total ionization branch with $\Gamma_{iS} \simeq \Gamma_m$, which exists only for $\Gamma_d > \Gamma_m$.

In conclusion, we have shown that a *regular* sonic point (with no discontinuity in plasma derivatives) may exist inside a channel of constant area in a *natural* way by compensation of diffusion and ionization effects. This implies that the sonic point is within or close to the ionization layer. The position of the sonic point is not set *a priori*, it depends on the control parameters and is part of the solution of the problem. Regular sonic transitions were also discussed by Fruchtman and Fisch[10]. In addition, they suggested forcing a choked internal point by introducing a current discontinuity; thus, their solution matches two choked flows (with $\bar{G}_S^- > 0, \bar{G}_S^+ < 0$) at the prescribed discontinuity point.

3.3 Structure of the plasma flow

The preceding section has shown that supersonic-exit solutions with i_d moderately above 1 seems to be the most efficient operating regime of a Hall thruster. The results we show next on the plasma structure and the thruster output parameters will confirm this. These results are presented in dimensional form to facilitate the comparison with real experiments.

Figures 3.2(a)-(i) show spatial profiles of the main plasma variables for a supersonic-exit solution and geometrical and operational parameters typical of a SPT-100 thruster[25]; all parameters are listed in the figure caption. We observe that the structure of the plasma response can be divided into the six regions sketched in Fig. 2.1(b). The first significant feature is that the *ionization region* is placed in the middle of the channel, more or less between points D and H, which can be defined as the places where v_{xi} changes sign and T_e is maximum, respectively; this yields $x_D \sim 13.6$ mm and $x_H \simeq 17.4$ mm, with $T_{eH} \sim 91.3$ eV. Notice in Fig. 3.2(b) the peaked shape of $\nu_i(x)$. The point of maximum electron pressure, $p_e = n_e T_e$, is at $x \simeq 14.1$mm, very near to the proposed entrance of the ionization layer. The sonic point S is downstream of point H ($x_S \simeq 19$ mm) and the temperature there ($T_{eS} \simeq 89.6$ eV) is close to the peak temperature; notice that point S cannot be far from point H since the ionization terms are needed to define the crossing condition $G_S = 0$, Eq. (3.16).

Upstream of the ionization layer is the large *diffusion region* (region CD), characterized by a reverse, low-velocity ion flow, a low electron temperature ($\sim$ 2eV), an insignificant electric field ($\phi_C - \phi_D \sim 1$ V) and a quasi-linear pressure gradient as the force driving the electron diffusion. The relative value of the reverse ion flow is $|\eta_{iB}| \simeq 0.24$ (of the order of the one measured in Ref. [1]). Tied to the anode, there is the *anode sheath* (region AB) characterized by a potential jump $\phi_{sh} \simeq 3.8$ V and a negligible thickness in the channel scale ($x_B \simeq x_A = 0$ for $\lambda_D/L \to 0$.). The *anode presheath* (region BC) is a transition region between the sheath and the diffusion region, where the reverse ion flow is accelerated to meet the Bohm condition at the sheath entrance; it is rather thin ($x_C - x_B \sim$ 1mm) and observable in Fig. 3.2(f) only.

The sharp transition from the diffusion region to the ionization region is related to the exponential dependence of the ionization cross-section on the electron temperature T_e, as we will further comment on below. The large value of T_e in the ionization region – and its low value in the diffusion region– are consequences of excluding the heat conduction and the losses to lateral walls. The electric potential remains practically constant until well inside the ionization layer, then it starts decreasing; the total potential variation across the ionization layer is $\phi_D - \phi_H \simeq 51.4$ V.

Downstream of the ionization layer there is the *internal acceleration region* (region HE), where the ion flow is accelerated by the electric field. The potential decrement in this region is $\phi_H - \phi_E \simeq 91.0$ eV and the temperature at the channel exhaust is still large ($T_{eE} \simeq 65.3$eV) so the effects of the electron pressure are significant there still. The *plume* is the extension of the internal acceleration region. The form of the plume profile shown in Fig. 3.2(b) comes from the solution for $A(x)$ in Eqs.(3.2). The semi-angle of divergence is maximum at the channel exit, $\delta_E \simeq 32.3^o$, but it does not change much since most of the increase of the ion velocity took place inside the channel; the typical range of δ in experiments[26, 27] is $30^o - 40^o$. In the near-plume (region EP) the radial area increases from $A_E = A_c \simeq 45$ cm^2 to $A_P \simeq 76$ cm^2. The potential variation in the near-plume is $\phi_E - \phi_P \simeq 150$ V, about 53% of the total discharge voltage. The minimum of the electric potential at the cathode (point P) provides the electric field required to move the electrons into the beam. Indeed, the potential variation in the far-plume, $\phi_\infty - \phi_P \simeq 34.8$ V, can be considered as a part of the energy loss associated to the cathode.

There are two 'free' parameters in the solution of Fig.3.2: L_{EP} and α_B. The first parameter seems to affect weakly the plasma response except when it becomes too small. On the contrary, the plasma response is very dependent on the value of the Bohm parameter. In fact, the best fit with experimental results is obtained with $16\alpha_B \sim 0.2$ instead of the classical value, $16\alpha_B = 1$. For the chosen value of α_B anomalous diffusion becomes dominant only downstream the ionization region, as the quick change in the derivative of ν_d around point D, in Fig.3.2(i), illustrates.

The plasma structure for a choked-exit solution is very similar to the one presented here except that (i) ionization might not be near-total, (ii) the region of supersonic acceleration is totally external, and (iii) the plume divergence is large. Indeed for practical values of h/L, the condition $G_S^+ = 0$, depicted in Fig.3.1, leads to divergence angles above 45°. Clearly, the 1-D plume model is hard to apply there. This consideration and the fact that the experimental data fits in general well with supersonic-exit solutions makes advisable to continue the investigation of choked-exit solutions.

3.4 Thruster performances

Looking again at the case of Fig.3.2, we show now that the main output parameters for thruster performances agree rather well with experimental values[25]. The discharge current is $I_d \simeq 4.36$ A (versus 4.5 A experimentally) The thrust, computed at the channel exhaust as

$$F = m_i(\Gamma_i v_{xi})_E + (p_E - p_\infty)A_c, \tag{3.18}$$

is $F \simeq 92.8$mN (versus 82 mN experimentally). The thrust efficiency, defined in the usual way as

$$\eta = F^2/2\dot{m}I_dV_d, \tag{3.19}$$

is $\eta \simeq 63\%$ (versus 52% experimentally, excluding cathode flow). Energy losses neglected in this model will reduce somehow these two last magnitudes. It is interesting to measure how different phenomena affect the thrust efficiency. This can be factorized as

$$\eta = \eta_u^2 \eta_c \eta_e \eta_p, \tag{3.20}$$

with $\eta_u = \eta_{i\infty}$ the propellant utilization, Eq.(3.5), $\eta_c = 1/i_d$ the current efficiency, $\eta_e = m_i v_{xi\infty}^2/2eV_\infty$ the energy efficiency, and $\eta_p \equiv \eta_{pc}\eta_{pd}$ the plume efficiency, this last one split into the cathode efficiency: $\eta_{pc} = V_\infty/V_d$, and the divergence efficiency: $\eta_{pd} = F^2/F_\infty^2$, with $F_\infty = m_i(\Gamma_i v_{xi})_\infty$. For the case of Fig. 3.2, one has, first, that the propellant utilization and the energy conversion are practically total: $\eta_u \simeq 100\%$, and $\eta_e \simeq 99.3\%$. Efficiency losses are distributed among the other three contributions: $\eta_c \simeq 88.7\%$, $\eta_{pc} \simeq 88.1\%$, and $\eta_{pd} \simeq 81.1\%$.

The present model does not consider the gas spent in the cathode for electron emission, which amounts to a 5-10% of the total gas flow, typically[26], and most of it (above 90%) is ejected into the plume without ionizing. On the one hand, this gas flow contributes as a loss to the thruster efficiency; on the other hand it is responsible for charge-exchange and backflow effects in the plume.

3.5 Asymptotic analysis

We derive here approximate solutions for the different plasma regions that explain most of the features observed in the exact solution studied in the preceding section.

Since ionization is limited to a thin layer, the zero-ionization form of the plasma equations will be applicable to most of the plasma flow. Making $\nu_i \to 0$ in Eqs. (3.2), one has conservation equations for particles, ion energy and electron enthalpy,

$$\Gamma_\alpha = \text{const} \quad (\alpha = i, e, n), \tag{3.21}$$

$$m_i v_{xi}^2/2 + e\phi = \text{const}, \tag{3.22}$$

$$5T_e/2 - e\phi = \text{const}. \tag{3.23}$$

To avoid integral terms with the electron diffusion frequency and simplify thus the analytical expressions, we will use, instead of a continuous function, two constant (i.e., average) values: $\nu_d = \nu_{d0}$, for the whole back-flow region AD, and $\nu_d = \nu_{d1}$, for the whole acceleration region DP.

We proceed to integrate Eqs.(3.2) from point B (with $x_B \simeq x_A = 0$, $M_B = -1$) towards the cathode P. To neglect ionization in the rear part of the channel we assume that $T_{eB} \ll E_i$. Then, from Eqs.(3.21)-(3.23) and (3.3) the ion velocity satisfies

$$\frac{v_{xi}}{v_{xiB}} = \frac{n_{eB}}{n_e} \simeq 1 + \frac{x}{x_C} - \sqrt{\left(1 + \frac{x}{x_C}\right)^2 - 1}, \tag{3.24}$$

where $v_{xiB} = -\sqrt{5T_e/3m_i}$ and

$$x_C = \frac{8}{5}\frac{m_i|v_{xiB}|}{m_e\nu_{d0}}\frac{\Gamma_{iB}}{\Gamma_{eB}}$$

is the characteristic thickness of the anode presheath. Observe that x_C tends to zero with Γ_{iB}.

The *diffusion region* corresponds to $x \gg x_C$. From Eq. (3.24), the asymptotic behavior of the ion velocity is

$$v_{xi}/v_{xiB} \simeq x_C/2x \to 0.$$

The plasma temperature and the voltage also tend to constant values,

$$T_e \to T_{eC} = (4/3)T_{eB}, \quad e\phi \to e\phi_C = e\phi_B + (5/6)T_{eB}, \tag{3.25}$$

so the electric field tends to zero. On the contrary, the electron pressure increases monotonically:

$$p_e \simeq p_{eB} + |\Gamma_e/A_c| m_e \nu_{d0} x, \tag{3.26}$$

and provides the driving force for the electron axial motion in the diffusion region. Since $T_e \simeq$ const, the plasma density changes in the same way as the pressure. Weak electric fields and nonzero density gradients upstream of the ionization layer are confirmed by experiments[1].

The *transition to the ionization region* (around point D) requires the inclusion of small ionization effects. The evolution of T_e there is governed by the exponential dependence of the ionization rate on T_e, for $T_e/E_i \ll 1$. Keeping $d\phi/dx \simeq 0$ and using Eq.(3.26) for p_e, the electron temperature in this transition layer satisfies

$$\frac{dT_e}{R_i(T_e)} \simeq -n_n \frac{T_e + \bar{\alpha}_i E_i}{T_e} m_e \nu_{d0} x dx$$

($\bar{\alpha}_i = 2\alpha_i/5$), and its approximate solution is

$$x^2 \simeq L_{AD}^2 - \frac{2T_e^3}{(T_e + \bar{\alpha}_i E_i) E_i m_e \nu_{d0} n_n R_i(T_e)}, \tag{3.27}$$

with

$$L_{AD}^2 \simeq \frac{2T_{eC}^2}{\bar{\alpha}_i E_i^2} \times \frac{T_{eC}}{m_e \nu_{d0} \nu_{iC}}. \tag{3.28}$$

Equation (3.27) yields $T_e(x)$ implicitly, showing a large gradient around $T_e/E_i = O(1)$, where the ionization rate $R_i(T_e)$ increases sharply. This justifies that L_{AD}, as defined by the two last equations, is effectively the length of region AD. Equation (3.28) shows also how the position of the ionization layer is influenced by different factors. The pressure satisfies Eq. (3.26) up to the ionization layer and, setting its maximum around point D, one has

$$p_{eD} \simeq |\Gamma_{eB}/A_c| m_e \nu_{d0} L_{AD}. \tag{3.29}$$

The plasma density, obtained from p_e/T_e, gets its maximum before point D, due to the fast increase of T_e.

A complete analytical solution for the *ionization layer* is not available, but there are several useful expressions relating point D and point S (just downstream of point H, as we commented on previously). Conditions $v_n/v_{xiS} \ll 1$ and (3.17) are enough, generally, to neglect electron diffusion in the bulk of the ionization layer, and the right-hand side of the ambipolar momentum equation (3.3). Then, one has

$$m_i n_e v_{xi}^2 + p_e \simeq p_{eD},$$

across that layer. Particularizing at point S and using $M_S = 1$ we obtain two relations,

$$p_{eS} = \frac{3}{8} p_{eD}, \qquad T_{eS} = \frac{5 p_{eS}^2 A_c^2}{3 m_i \Gamma_{iS}^2}, \tag{3.30}$$

and $\Gamma_{iS} \simeq \Gamma_m$ for a supersonic-exit solution. From Eqs.(3.2) and (3.29), the estimated thickness of the ionization layer is

$$L_{DH} \sim L_{DS} \sim \frac{v_{xiS}}{\nu_i^*} \sim \frac{m_e \nu_{d0}}{m_i \nu_i^*} L_{AD},$$

and $L_{DS} \ll L_{AD}$, as expected. From the equation for ion momentum in Eqs.(3.2), the potential jump across the ionization layer is

$$e\phi_D - e\phi_S \simeq \frac{5}{6} T_{eS} + m_i \int_{x_D}^{x_S} v_{xi} \nu_i dx \equiv (1 + \delta_i) \frac{5}{6} T_{eS}, \tag{3.31}$$

with parameter δ_i small (~ 0.10) in the cases we have analyzed.

In the *acceleration region* and the *plume* of a supersonic-exit solution, there are practically no neutrals to ionize and Eqs.(3.21)-(3.23) are applicable again. For $T_{eP} \ll T_{eS}$ and $\eta_{iS} \simeq 1$ one finds

$$v_{xiP} \simeq 2 v_{xiS}, \quad e\phi_S - e\phi_P \simeq (5/2) T_{eS}. \tag{3.32}$$

The area variation in the plume frustrates an exact integration of Eq.(3.3). Nevertheless, an approximate integration, useful to evaluate the influence of different parameters, is

$$p_{eS} \simeq \frac{3(\Gamma_d - \Gamma_m)}{2\bar{A}} m_e \nu_{d1} L_{SP},$$

with $\bar{A}$ an average value of the the radial area of the jet. This completes the analysis on the different plasma regions.

3.6 Influence of control/design parameters

We restrict the discussion to supersonic-exit solutions. Before showing exact numerical results, let us use the preceding asymptotic analysis on the plasma behavior, to obtain an approximate idea of the scaling laws among the the thruster parameters. Since that analysis corresponds to a rather ideal situation (no losses to lateral walls and no heat conduction) some laws must be taken with prudence.

First, adding the potential jumps in the different regions [Eqs.(3.25), (3.31), and (3.32)], one has,

$$qV_d + q\phi_{sh} \simeq \frac{5}{6} T_{eB} + \frac{20 + 5\delta_i}{6} T_{eS}; \tag{3.33}$$

observe that the potential discharge in the acceleration region is about three times that of the ionization region. Next, keeping only dominant terms, the maximum plasma temperature turns to be proportional to the discharge voltage,

$$T_{eH} \sim T_{eS} \simeq (3/10) e V_d.$$

This law agrees well with the numerical results of Fig. 3.2, which indicates that the overestimate of the maximum temperature is intrinsic to the present model. Therefore, energy losses at lateral walls and heat diffusion cannot be excluded in order to estimate correctly the plasma temperature.

From Eq.(3.32) and for $L_{EP} \to 0$, the thrust, Eq.(3.18), satisfies

$$F \simeq \dot{m}\sqrt{\frac{2qV_d}{m_i}}. \tag{3.34}$$

From Eq.(3.30), the maximum pressure in the channel verifies

$$p_{eD} \simeq \frac{8}{3}p_{eS} \simeq \frac{4F}{5A_c}. \tag{3.35}$$

The mean temperature in the diffusion region is $T_{eC} \simeq (4/3)T_{eB}$. From Eq. (3.28), one has

$$T_{eC} \propto \ln^{-1}\left(\eta_c^2 V_d \dot{m}/\nu_d\right). \tag{3.36}$$

From Eq.(3.5), the length of the acceleration region verifies

$$L_{SE} \simeq \frac{\eta_c}{(1-\eta_c)}\frac{1}{5\nu_{d1}}\sqrt{\frac{qV_d}{m_i}}, \tag{3.37}$$

which differs from the law

$$L_{SE} \simeq \sqrt{qV_d/m_i\nu_d\nu_i},$$

proposed by Erofeev and Zharinov (cited in [5]). Adding L_{SE} to L_{AD}, deduced from Eq. (3.29), one has

$$L \simeq \frac{4\eta_c}{5\nu_{d0}}\sqrt{\frac{qV_d}{m_i}}\left[1+\frac{\nu_{d0}}{4(1-\eta_c)\nu_{d1}}\right], \tag{3.38}$$

which is an implicit equation for η_c.

Figures 3.3 to 3.8 show the effects of V_d, $\dot{m}$, B_m, L, L_{EP}, and α_B on the plasma response and the thruster performances. These plots have been obtained from continuation routines, departing from the solution of Fig. 3.2. The main remarks are:

1. The thrust depends on the gas flow and the discharge voltage, and follows rather closely Eq.(3.34), which is in good agreement with experimental data.
2. Contrary to the thrust,the efficiency η depend on (and increase with) the channel length and the magnetic field. The increase with B_m agrees well with experimental data [5]. However, experiments indicate often that η presents a maximum with L, instead of the monotonic behavior found here; losses at lateral walls, which seem to increase with L, would explain the difference.
3. Since the energy and ionization efficiencies are practically total ($\eta_u, \eta_e \simeq 1$) in our model, the variation of the thruster efficiency depends basically on η_c and η_p; notice also that η_c is a dimensionless representation of the inverse of the discharge current, $1/I_d$.

4. Contrary to common ideas, the distance from the ionization layer to the thruster exhaust depends more on V_d and L than on the magnetic field profile and strength. For usual conditions, the ionization layer is placed in the outer half of the channel, and never next to the anode. This is consequence of the role of the electron pressure on the plasma response.

5. The average temperature in the inner part of the thruster, T_{eC}, depends mainly on $\dot{m}$ and L. In our model, possibly because of the zero heat conduction, this temperature is too low.

6. Except $\dot{m}$, the rest of the control parameters affect significantly the relative reverse flow of ions, η_{iB}. Experimental data on the ion flow in the deepest part of the thruster is difficult to obtain. Few experiments have identified the existence of a reverse flow and we did not find anyone that measures the changes in the reverse flow with the control parameters.

7. There is an indirect experimental confirmation that our predictions on the reverse ion flow are correct. Our model predicts that stationary solutions fail to exist when the plasma cannot sustain a reverse ion flow; this corresponds to points with $\eta_{iB} \simeq 0$ in the Figures. If we take, for instance, the case of Fig. 3.5, where the magnetic field strength is varied, we observe that there is a maximum value of the magnetic field for a steady-state solution. This is exactly what happens experimentally: strong oscillations appear when the magnetic field becomes too high; see, for instance, Fig. 3 of Ref.[5]. We come back to the limit $\eta_{iB} \simeq 0$ below.

8. A parameter difficult to choose is the position of the virtual cathode, L_{EP}. Figure 3.8 shows that the position of point P affects more the thrust and the efficiency, when L_{EP} becomes small. The two efficiencies involved in the plume, η_{pt} and η_{pc}, behave in an opposite way with L_{EP}, η_{pt} decreasing with L_{EP}. Although this issue requires further analysis, it would seem desirable to choose L_{EP} in the range where it affects the least the thruster performances.

9. Figure 3.7 shows that α_B affects strongly the reverse ion flow. If we want to keep a low value for that flow, there is no much tolerance in the value of α_B, unless other parameters are changed simultaneously.

The evolution of η and η_{iB} with B_m and L, seems to indicate that optimum operation conditions correspond to very low reverse flows. But operating the thruster in these conditions has the drawback of that a small change in any control parameter can lead the thruster response into the non-stationary regime. This scenario seems to be the one taking place in practice: the thruster is operated near the limit of the stationary regime and there appear periods of a strong oscillatory response. If this is the case, the observed oscillatory response would not be due to a plasma instability. For given $B(x)$ and L, stationary solutions fail to exist for low discharge voltages because the plasma temperature is too low to produce enough ions to maintain a supersonic region downstream of the ionization layer and quasineutrality upstream of it. Longer channels and higher magnetic fields mean larger plasma pressures and steeper profiles which can be sustained steadily only by higher voltage discharges.

3.7 Discussion

The preceding results show that the basic axial 1-D model proposed in this chapter reproduces correctly the whole structure of the plasma in a Hall thruster: diffusion region, ionization layer, acceleration region, and near-plume. Although the main objective of the model was to understand the plasma behavior in the thruster, quantitative results for output parameters like thrust, efficiency, and discharge current agree well with experimental cases, which adds reliability to the model.

Attention has been paid to identifying the main phenomena that control the plasma response. We summarize the main aspects here, since previous models omit one or another. First, there is the dependence of the ionization rate on the electron temperature: the strong gradient of $R_i(T_e)$ around the ionization energy separates rather sharply the ionization and acceleration regions from the diffusion region and leaves this last region with a low temperature. Second, we have shown that a reverse ion flow is forced by physical conditions around the anode: solutions with $v_{xi} \geq 0$ at the anode boundary are not compatible with an ion-attracting sheath and therefore do not satisfy the condition of current continuity there. Since the ionization layer starts around $v_{xi} = 0$, the slow reverse ion flow is necessary to sustain the long diffusion region, also. The third and main aspect to emphasize is the crucial role of the electron pressure in all plasma regions: i) the pressure term explains the subsonic to supersonic transition of the ion beam; ii) the electron pressure is the only driving force for the electrons in the diffusion region, where the electric field is practically zero; iii) the pressure drop, instead of the diffusion losses, balances the gain in ion momentum in the ionization layer; iv) the maximum pressure is a central parameter controlling the position of the ionization layer.

Boeuf and Garrigues[11], in spite of neglecting the electron pressure, recovers a zero-electric field upstream the ionization region, by making the B-field (and, therefore, the diffusion frequency) negligible there. From our preceding conclusions we find their solution debatable on the following grounds: i) such a small B-field, which does not correspond to usual settings, violates the closed-drift condition sustaining the diffusive model of the electrons; ii) they neglect the pressure term in the momentum equation in spite of being much larger than the electrostatic force; and iii) the compression work is kept, however, in the energy equation.

The existence of a *regular* sonic point inside the thruster is not just a mathematical artifice. Physically, it implies the local balance between Ohmic heat dissipation into the electron gas and heat removal from it by ionization. The latter effect is strongly dominant near the ionization peak, whereas dissipation, although weaker, dominates outside the layer. Hence, the sonic balance can only be struck at a point where ionization has nearly ended or has just barely started. The second option is precluded by the fact that there is no mechanism ahead of the ionization layer that would provide the potential drop to accelerate the ions to their forward speed of sound. There is an interesting analogy between this ionization layer and the shock/combustion layer in a strong detonation front. In both cases, the downstream exit point of the layer is found to be sonic, although, of course, the layer inlet is supersonic in a detonation and subsonic in the ionization layer. The underlying mechanism is the same in both problems, the condition of a smooth sonic passage here being equivalent to the Chapman-Jouguet condition in combustion fronts, which states the local balance between the chemical heating and the heat diffusion. One interesting conclusion, valid for both, detonation and ionization layers, is that the occurrence of this 'Chapman-Jouguet condition' is a consequence of the smallness of the ratio of two kinetic rates, and will only be as precise as this ratio is small.

A relevant conclusion, not fully investigated yet, is that the presence of a reverse ion flow seems essential for the existence of stationary solutions, the zero-reverse flow condition indicating the transition to some non-stationary type of solutions. The parametric investigation on the effects of the main design parameters (discharge voltage, magnetic field, channel length, mass flow,...) on the thruster performance indicates, for instance, that the excessive magnetic field eventually suppress the reverse ion flow and make it impossible to maintain steady-state quasineutrality in the diffusion region, in agreement with testing experience.

Another issue requiring further research is whether the transition from the complete to the incomplete ionization modes[17] corresponds to the transition from the supersonic-exit to the choked-exit solutions, or, on the contrary, from the high- to the low-ionization branches of supersonic exits.

The main flaw of the present model is the extremely high peak temperature. We will try to improve this issue in Chapters 5 and 6 by including plasma interaction with lateral walls and heat conduction, respectively into the electron energy balance.

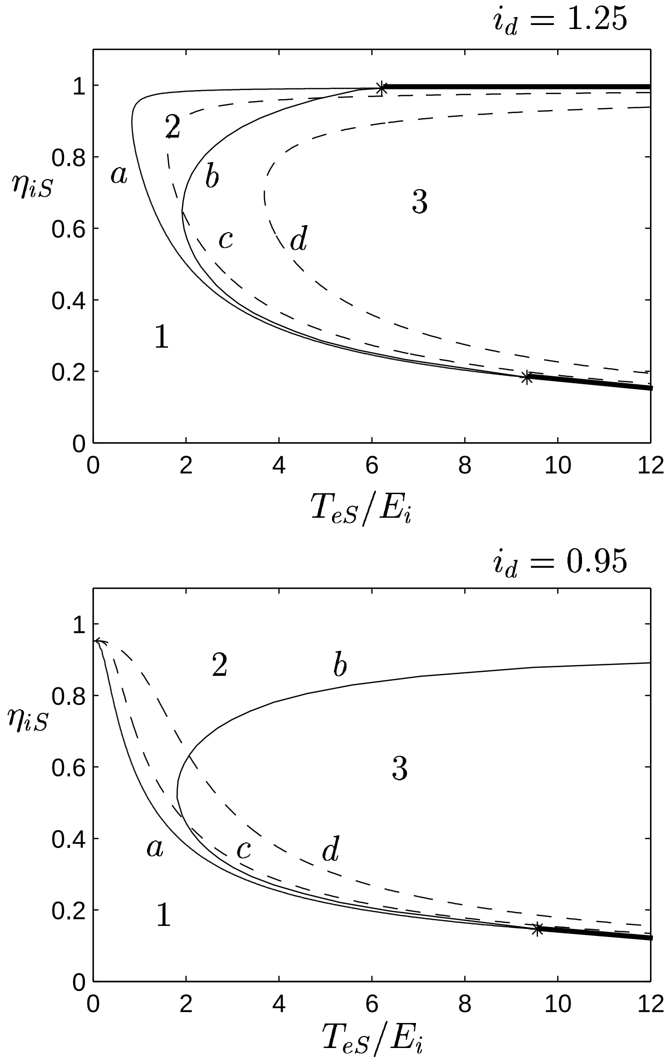

Figure 3.1: [gcerotit] Regions leading to different types of solutions between points S and B for two values of i_d and a constant B-profile. Line a corresponds to $G_S^- = 0$; line b to $\eta_{iB} \to 0$; lines c and d to $G_S^+ = 0$ for $\tilde{d}/\tan\delta = 0.3$ and 0.1, respectively. Region 2 is between lines a and b; region 4 (supersonic-exit regime) corresponds to the thick parts of line a, to the right of the intersections (asterisks) with line b. Some parameter values are: $\Gamma_* = \Gamma_m$, $\omega_e/\nu_* = 84.6\sqrt{m_i/m_e}$, $\tilde{v}_{nA} = 0.1$, $\alpha_i = 2.5$, and $\alpha_B = 1/80$.

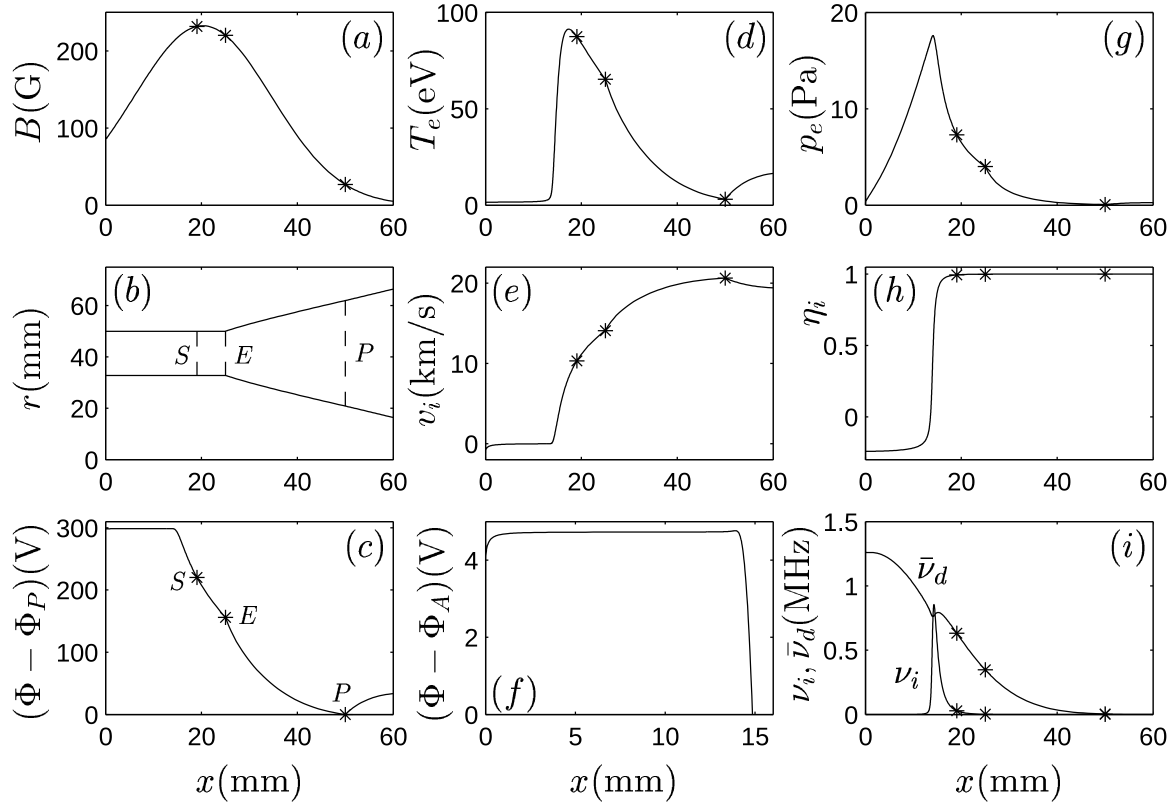

Figure 3.2: [basetit] Supersonic-exit solution for: xenon, $B(x)$ as shown in (a) [$B_m \simeq 233$G, $x_m \simeq 20.3$mm, $L_m \simeq 20.2$mm], the channel geometry shown in (b)[$L \simeq 25$mm, $h_c \simeq 17.2$mm, $A_c \simeq 45\text{cm}^2$, $L_{EP} \simeq 25$mm], $\dot{m} \simeq 5.32$ mg/s, $V_d \simeq 293.3$ V, $T_{eP} \simeq 2.7$ eV, $v_n \simeq 300$ m/s, and $\alpha_B \simeq 1/80$. The profile of the plume in (b) is part of the solution; subplot (f) is a magnified copy of subplot(c) for region AS; asterisks represent points S, E and P; and $\bar{\nu}_d \equiv (m_e/m_i)\nu_d$ in (i).

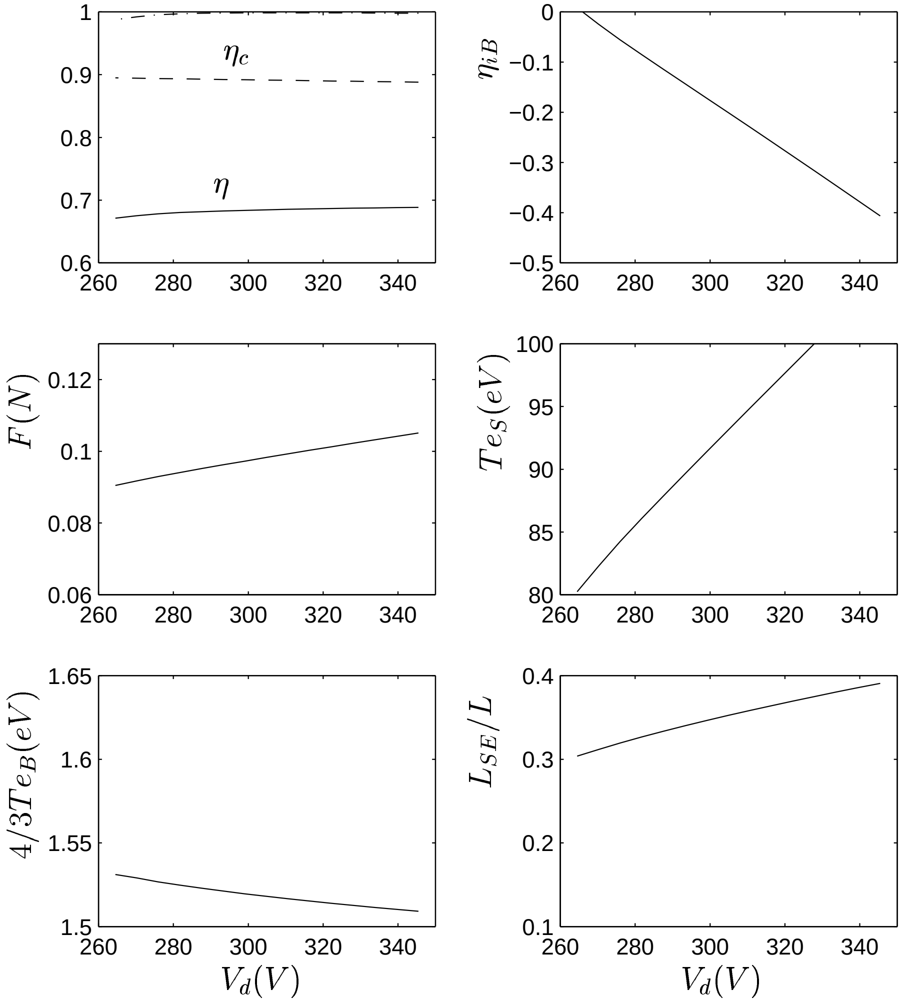

Figure 3.3: Influence of the discharge potential on the plasma response. Other parameters are as in Fig. 3.2.

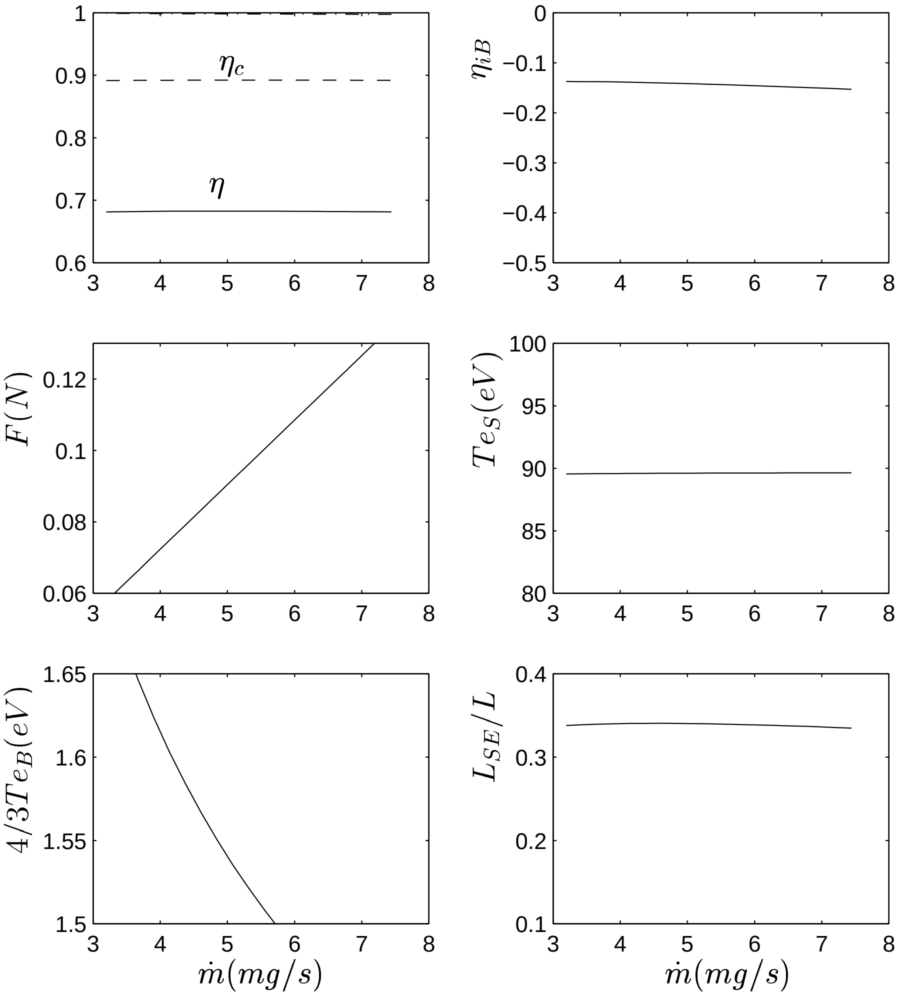

Figure 3.4: Influence of the gas flow on the plasma response. Other parameters are as in Fig. 3.2.

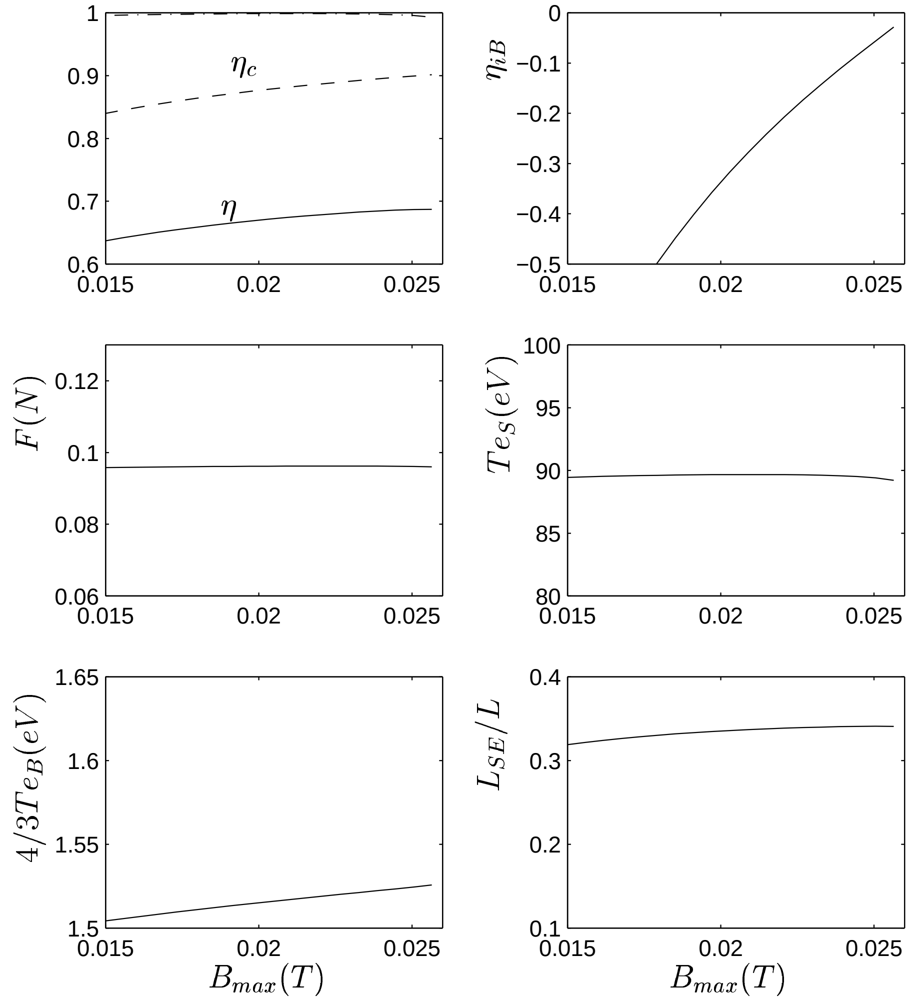

Figure 3.5: Influence of the maximum B-field on the plasma response. Other parameters are as in Fig. 3.2.

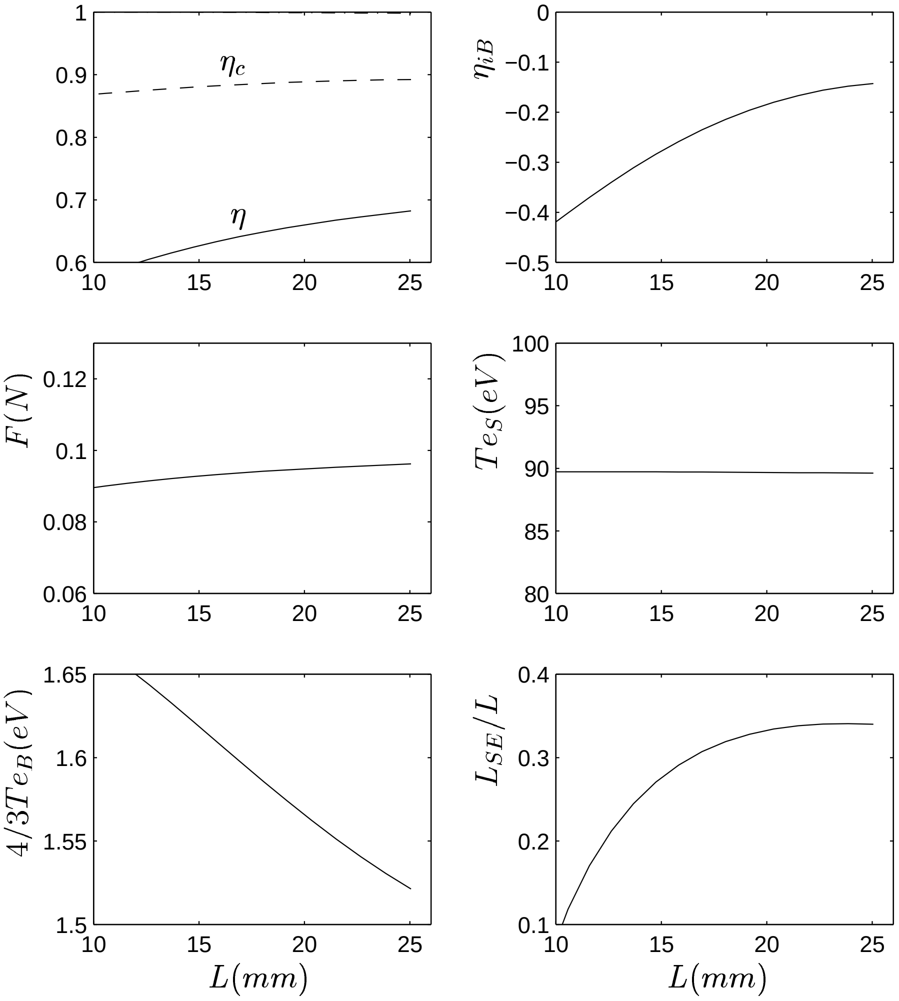

Figure 3.6: Influence of the channel length on the plasma response. Other parameters are as in Fig. 3.2.

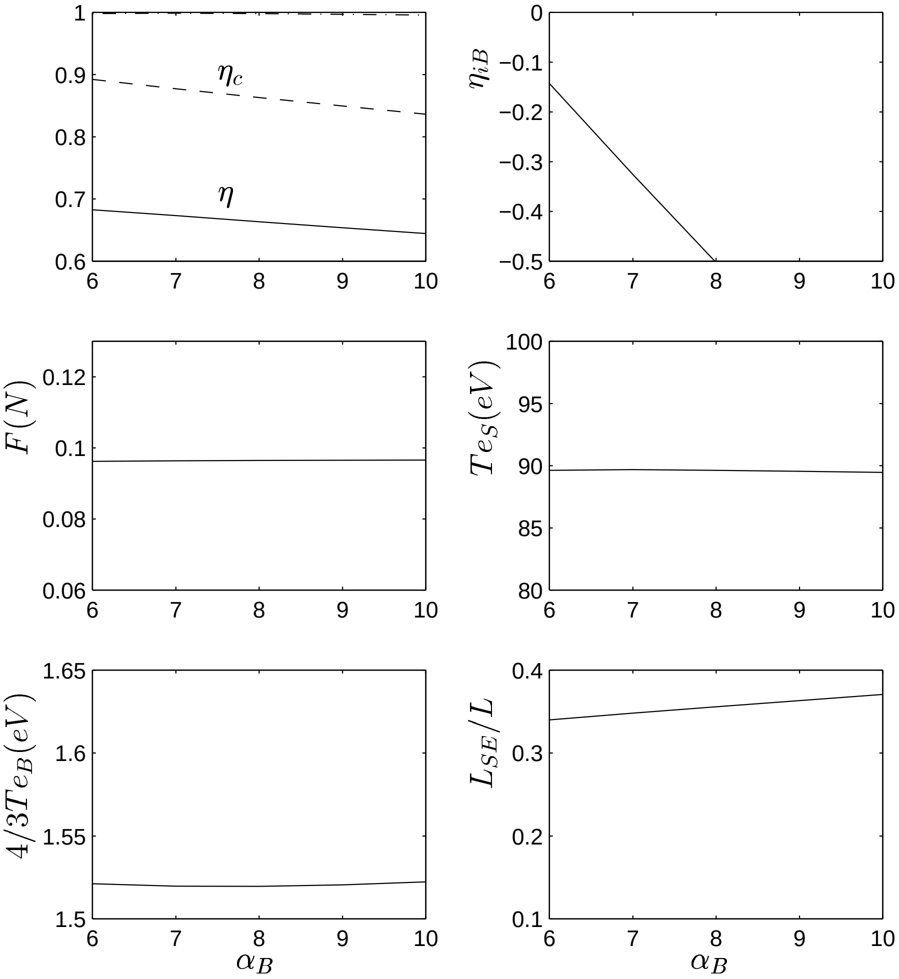

Figure 3.7: Influence of the Bohm diffusion parameter on the plasma response. [Please, notice that α_B in the plots is $\alpha_B\sqrt{m_i/m_e}$ in the text.] Other parameters are as in Fig. 3.2.

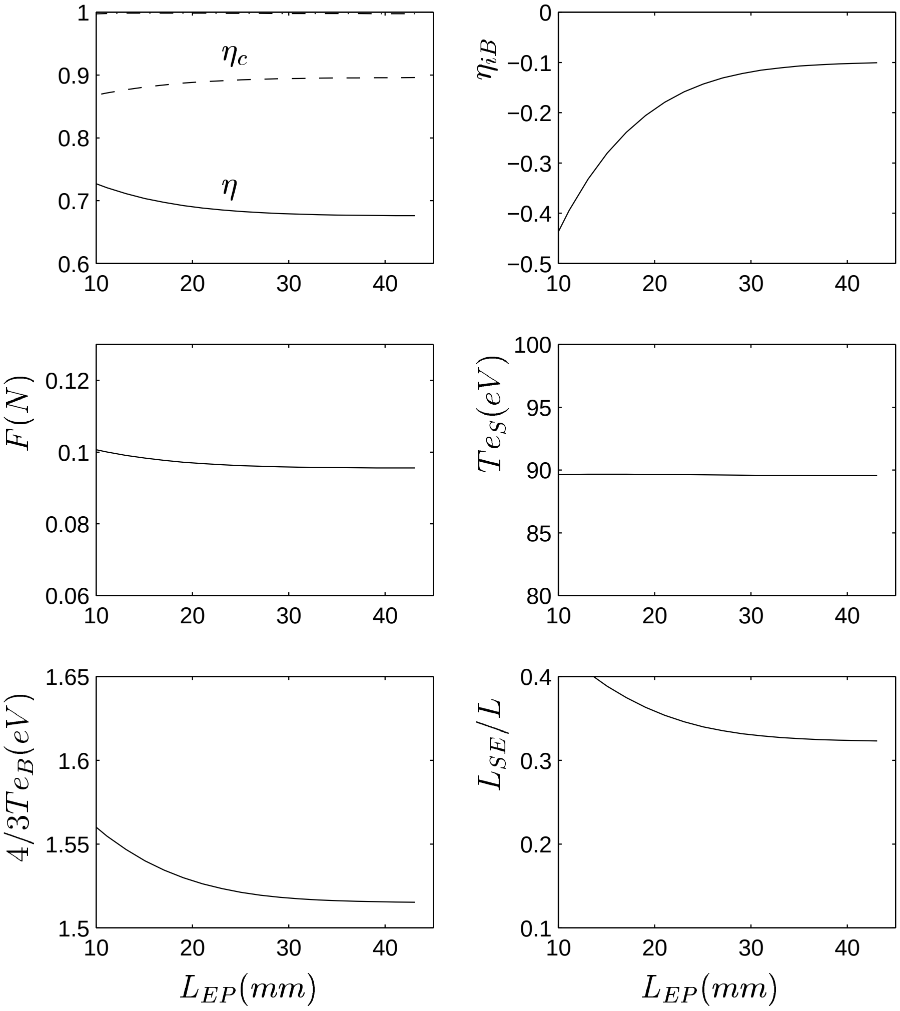

Figure 3.8: Influence of the cathode distance on the plasma response. Other parameters are as in Fig. 3.2.

Chapter 4

THE RADIAL MODEL

4.1 Introduction

The walls of the discharge channel of the SPT class of Hall thrusters is made of a ceramic insulator. The interaction of the plasma with these dielectric walls seems to affect greatly the plasma discharge and the thruster characteristics[28, 29, 12, 30]. From simple reasoning several phenomena are expected. First, the zero current condition at the dielectric wall implies, in general, the formation of an electron-repelling sheath there. Second, ions attracted to the walls are recombined, thus reducing the actual propellant utilization and the thruster efficiency. Third, energetic electrons arriving at the wall deposit their energy there, affecting the average temperature of the plasma in the channel and, consequently, the ionization process. Four, ceramic materials present large yields for secondary electron emission. On the one hand, these electrons modify the sheath structure, which could attain charge saturation conditions[31, 32]. On the other hand, since these electrons are replacing primary electrons, which were magnetically-guided, an extra near-wall conductivity for the average electron population has been suggested[33].

4.2 Presheath/sheath model

Here we analyze the radial structure of the plasma in a fixed axial position of the thruster. Fife, Martínez-Sánchez, and Szabo[29] were the first to obtain consistent expressions for the particle, electron momentum, and electron energy wall-source terms by studying the behavior of the space-charge sheaths around the lateral walls; the effect of the potential drop in the radial presheath was added later by Ahedo and Martínez-Sánchez[12].

More recently, Stephens and Ordonez [31] and Jolivet and Roussel[32] have shown that large enough secondary emission yields these radial sheaths can charge-saturate the radial sheaths, a situation not considered in the previous models and with important consequences. Both Refs. [31] and [32] (i) use a particle approach (either kinetic equations or particle-in-cell formulations), and (ii) force thermalization of the secondary emission at an artificial 'edge plasma source', placed at the center of the channel cross-section. Our model adopts the two-scale (i.e. asymptotic), macroscopic framework already used in Ref.[12], and includes trapped secondary electrons as a part of the confined electron population in the bulk of the plasma. In addition, our model includes diffusion effects on the ion radial motion, due to collisional processes and the axial ion transport. The validity of the macroscopic approach for a similar problem was shown in Ref. [34]. With respect to kinetic models, a macroscopic model presents the advantages of: (i) following directly the evolution of macroscopic variables (like density, velocity, ...), and (ii) being more tractable since it solves ordinary differential equations, exclusively, instead of integro-differential ones.

Figure 4.1 sketches the radial model. Macroscopic variables are functions of r, and the axial position x appears just as a parameter in the equations. To highlight the fundamental aspects of the solution, cylindrical effects are neglected in the present version; thus the radial structure is symmetrical with respect to the middle-plane (point M in Fig. 4.1). In principle, the potential profile is assumed monotonic (in each half-channel); the transition to a charge-saturated regime, with local minima of the potential, will be investigated afterwards.

The model is supported on three main hypotheses:

(1) There are two disparate scales on the radial profile of the electric potential: the Debye length λ_d, and the channel radial width d, with

$$\lambda_d \ll d.$$

As it is well known from the seminal work of Tonks and Langmuir[35], this justifies a two-scale analysis, where, except for the two thin *non-neutral sheaths* tied to the lateral walls, the bulk of the plasma is quasineutral (*the radial presheath*). The electron-repelling sheaths are needed to satisfy the zero-current condition at the walls.

(2) Secondary electron emission is due mainly to the diffusive radial flux, g_p, of primary electrons (population p) reaching the walls. As noticed in Ref. [32], the secondary electrons can be classified into those becoming trapped in the channel and eventually thermalized (population s), and those crossing the presheath (in both ways) and being collected back at the opposite wall (two free populations f). The present study is restricted to the *total trapping* case, with no free populations.

(3) A consistent treatment of the s-population is the major challenge of the model. Secondary electrons flow continuously from the two walls and are expected to thermalize through multiple reflections at both sheaths. Therefore, in the bulk of each cross-section (i.e. the presheath, basically) there are trapped electrons with different time histories, and any stationary model must figure out which is the mean collective distribution in time of this process. Our proposed model consists of: (a) treating primary(p) and secondary(s) electrons as independent populations within each sheath; (b) to group all electrons into a single electron population (e) in the presheath. The details of the trapping process are out of the scope of a macroscopic model. Density, temperature, and diffusion flux of the population e are defined through conservation conditions at the two presheath/sheaths transition. We find this model more natural than the one of Refs. [31] and [32], where secondary electrons move freely from the wall to the center of the cross-section, where they are automatically transformed into trapped electrons for the other half-channel. This sudden thermalization is rather artificial and introduces an undesirable electric field around the cross-section center (see Fig. 1 of Ref.[32]). Another advantage of our radial model is to be compatible directly with axial models, where a single electron species is generally considered.

When solving the equations for the presheath and sheath, we will make use of the fundamental properties of this classical problem, like

(a) The two-scale analysis implies that the sheath is a layer discontinuity in the quasineutral scale of the presheath. The presheath has its own spatial structure, but with spatial gradients infinitely smaller than in the sheath. In particular, the ratio between the electric fields in presheath and sheath is $\lambda_d/d \ll 1$.

(b) On the presheath scale, the transition to the sheath corresponds, generally, to a turning point of the presheath solution (point Q in Fig. 4.2), that is, a point where derivatives of plasma variables become infinity; in particular, the electric field is *infinite* at point Q on the quasineutral scale. Indeed, the large gradients near the turning point are announcing the transition to the sheath with a much thinner spatial scale, the Debye length. The presheath turning point is identified by a certain condition on the plasma flow, which is known as the Bohm sonic condition.

(c) On the sheath non-neutral scale, the transition to the presheath corresponds to a *zero* electric field. In general, the sheath is semi-infinite in its own scale and the zero electric field is attained asymptotically.

4.2.1 The presheath

Equations are written for the half-channel $r_M < r < r_W$; the response in the other half-channel is symmetric. We assume the presheath to be constituted by two species only: free ions (i) and confined electrons(e). By definition, the presheath is quasineutral at every point:

$$n_i \simeq n_e.$$

In this issue we disagree with the following two statements of Stephens and Ordonez[31]: (i) quasineutrality is satisfied only globally in the presheath; and (ii) local quasineutrality at the presheath/sheath interface is the matching condition there (when the correct one is the Bohm sonic condition).

Based in 2D planar equations for ions, we define the following 1D radial model:

$$\frac{d}{dr} n_i v_{ri} = n_i \nu_w, \tag{4.1}$$

$$m_i v_{ri} \frac{dv_{ri}}{dr} + e\frac{d\phi}{dr} = -m_i v_{ri} \nu_r, \tag{4.2}$$

where

$$\nu_w = \nu_i - \frac{1}{n_i}\frac{\partial}{\partial x}(n_i v_{xi}) \tag{4.3}$$

is the frequency for net ion production in a radial section, which includes both ionization and the differential increment of the axial ion flux; and

$$\nu_r = \nu_i + \nu_{cx} + \frac{v_{xi}}{v_{ri}}\frac{\partial v_{ri}}{\partial x} \tag{4.4}$$

measures the 'friction' effect of collisional phenomena and axial transport on the radial velocity of the ions.

Ion equations (4.1)-(4.4) are completed with the electron equations

$$\begin{aligned} v_{re} &= v_{ri}, \\ 0 &\simeq -T_e \frac{dn_e}{dr} + en_e \frac{d\phi}{dr}. \end{aligned} \tag{4.5}$$

The first equation results from the zero-current condition at the lateral wall. In turn, this justifies neglecting the term $\nu_e m_e n_e v_{re}$ in the second equation and Coulomb collisions in Eq.(4.2). Also, the radial gradient of T_e (due to thermalization of secondary electrons, for instance) has been disregarded.

Operating with Eqs. (4.1), (4.2), and (4.5), the radial velocity satisfies

$$(T_e - m_i v_{ri}^2) \frac{dv_{ri}}{dr} = \nu_w T_e + \nu_r m_i v_{ri}^2. \tag{4.6}$$

The transition to the sheath, point Q, corresponds to the turning point of the presheath profiles. From Eq. (4.6), the transition (i.e. Bohm) condition is

$$v_{ri} = v_{riQ} \equiv \sqrt{\frac{T_e}{m_i}}. \tag{4.7}$$

To solve Eq.(4.6), the radial profiles of both frequencies must be specified. Here we will consider the plausible case

$$\nu_w(r) = \text{const}, \quad \nu_r(r) = \text{const}.$$

Then, the integration of Eq.(4.6) yields

$$\frac{1+\alpha}{\sqrt{\alpha}} \arctan(u\sqrt{\alpha}) - u = \frac{\nu_r}{v_{riQ}}(r - r_M), \tag{4.8}$$

where we called

$$u = v_{ri}/v_{riQ}, \quad \alpha = \nu_r/\nu_w.$$

The profiles for the density and the electric potential are then determined from Eqs. (4.1), (4.5) and (4.8),

$$\frac{e\phi_M - e\phi}{T_e} = \ln \frac{n_{iM}}{n_i} = \frac{1+\alpha}{2\alpha} \ln(1 + \alpha u^2). \tag{4.9}$$

Imposing the Bohm condition (4.7), i.e. $u = 1$, the potential drop $\phi_{QM} \equiv \phi_M - \phi_Q$, and the density change across the presheath are found to satisfy

$$\frac{e\phi_{QM}}{T_e} = \ln \frac{n_{iM}}{n_{iQ}} = \frac{1+\alpha}{2\alpha} \ln(1 + \alpha). \tag{4.10}$$

Also, setting $u = 1$ in Eq.(4.8) at $r_Q - r_M \simeq r_W - r_M = d/2$, we have

$$\begin{aligned} \frac{\nu_r}{\nu_0} &\equiv \tilde{\nu}_r(\alpha) = 2\Big(\frac{1+\alpha}{\sqrt{\alpha}} \arctan\sqrt{\alpha} - 1\Big), \\ \frac{\nu_w}{\nu_0} &\equiv \tilde{\nu}_w(\alpha) = \frac{\tilde{\nu}_r(\alpha)}{\alpha}, \end{aligned} \tag{4.11}$$

which is the parametric equation relating the two relevant frequencies of the radial problem. Here,

$$\nu_0 = \frac{1}{d}\sqrt{\frac{T_e}{m_i}} \tag{4.12}$$

is the frequency of reference for radial processes. Equation (4.11) expresses that the production/loss frequency is not free. The dielectric wall implies the presence of a non-neutral sheath, which forces the Bohm condition on the ion flow to the wall, and this makes ν_w not free. Its actual value depends on the acceleration process for ions and this is the meaning of the relationship $\nu_w(\nu_r)$. In the model of Ref. [12], where we assumed $\nu_r = 0$, ν_w was totally determined and equal to 4/3.

Figure 4.3 shows the profiles $\phi(r)$ for three values of $\tilde{\nu}_r$. On the presheath scale, the jumps of the different plasma variables across the sheath are vertical discontinuities starting at the turning point Q, and are to be determined from the sheath equations.

Figure 4.4 shows the evolution of $\tilde{\nu}_w$ and $e\phi_{QM}/T_e$ versus $\tilde{\nu}_r$, Eqs. (4.10) and (4.11). Asymptotic expressions for small and large values are

$$\begin{aligned} \tilde{\nu}_r \ll 1: &\qquad \tilde{\nu}_w \simeq \frac{4}{3}, &\qquad \frac{e\phi_{QM}}{T_e} \simeq \frac{1}{2}, \\ \tilde{\nu}_r \gg 1: &\qquad \tilde{\nu}_w \simeq \frac{\pi^2}{\tilde{\nu}_r}, &\qquad \frac{e\phi_{QM}}{T_e} \simeq \ln\frac{\tilde{\nu}_r}{\pi}. \end{aligned}$$

Physically, a large 'friction' implies a large potential drop to accelerate the ions to the Bohm velocity. As a consequence, n_{iQ}/n_{iM} is low, the plasma current to the wall is low, and $\tilde{\nu}_w$ is low.

4.2.2 The sheath

Both ion and electron dynamics present changes in the sheath. For $\lambda_d/d \to 0$ the sheath thickness is negligible compared to the channel width, the contribution of ν_w and ν_r to ion dynamics within the sheath is negligible, and Eqs.(4.1) and (4.2) yield the conservation of ion particles and energy. Within the sheath, electrons are classified into the main primary population (p), which diffuse towards the wall and causes secondary emission, and the population (s) of secondary electrons, which, after crossing the sheath, become trapped in the presheath, in a process not analyzed here. The set of macroscopic equations for the three species in the sheath are:

$$\begin{aligned} & n_i v_{ri} = \text{const} = g_i \equiv n_{iQ}\sqrt{T_e/m_i}, \\ & \tfrac{1}{2} m_i v_{ri}^2 + e\phi = \text{const} = \tfrac{1}{2} T_e + e\phi_Q, \\ & n_p v_{rp} = \text{const} = g_p = n_{pW}\sqrt{T_p/2\pi m_e}, \\ & n_p = n_{pQ} \exp\frac{e\phi - e\phi_Q}{T_p}, \\ & n_s v_{rs} = \text{const} = g_s, \\ & \tfrac{1}{2} m_e v_{rs}^2 - e\phi = \text{const} = \bar{T}_w. \end{aligned} \tag{4.13}$$

The value of the primary flux, g_p, was calculated assuming a Maxwellian distribution of temperature T_p. The mean energy of the population of secondary electrons when they leave the wall is $\bar{T}_w$, which can be assumed of the order of the wall temperature. Therefore, one expects

$$\bar{T}_w/T_p \ll 1,$$

which allows one to work in the asymptotic limit $\bar{T}_w/T_p \to 0$, except in the very vicinity of point W. Finally, the low value of $\bar{T}_w$ and the acceleration of the secondary electrons as they cross the sheath justifies neglecting thermal effects for them.

The flux of secondary electrons is assumed proportional to the flux of primary electrons:

$$g_s = -\delta_w g_p \quad (g_s < 0), \tag{4.14}$$

with δ_w the effective secondary emission yield. In addition, the zero-current condition at the wall relates the electron and ion fluxes,

$$g_i = g_p + g_s = (1 - \delta_w) g_p. \tag{4.15}$$

To compute the effective yield for secondary emission we start with the case of a monoenergetic electron beam. If E is the beam energy, we average over the different angles of incidence, and, for E low enough, we consider that δ_w satisfies

$$\delta_w(E) \simeq \left(\frac{E}{\bar{E}_w}\right)^p. \tag{4.16}$$

Here, $\bar{E}_w$ is the energy for 100% yield, and depends strongly on the wall material; the typical range, for the materials of interest in a Hall thruster, would be $\bar{E}_w \sim 20-100$ eV. The exponent p is around 0.5, for the same materials. Next, for a Maxwellian population of temperature T_p, the effective secondary emission yield can be computed by averaging the law (4.16) over the different electron energies. This yields[29]

$$\delta_w(T_p) \simeq \left(\frac{T_p}{E_w}\right)^p, \tag{4.17}$$

with

$$E_w = \frac{\bar{E}_w}{\Gamma(2+p)^{1/p}};$$

for $p = 0.5$, one has $E_w \simeq 0.57\bar{E}_w$. For $\bar{E}_w \simeq 30$ eV (Boron Nitride ceramic referenced in [12]) one obtains $E_w \simeq 16.64$ eV for $p = 0.576$, or $E_w \simeq 17.0$ eV for $p = 0.5$. For $\bar{E}_w \simeq 70.2$ eV (BNAIN ceramic referenced in [32]), one has $E_w \simeq 40.0$ eV for $p = 0.5$.

Plasma equations (4.13) are completed with Poisson equation

$$\frac{\epsilon_0}{e}\frac{d^2\phi}{dr^2} = n_p + n_s - n_i.$$

Integrating this equation together with Eqs.(4.13) and imposing that the electric field goes to zero asymptotically at point Q, that is

$$\left.\frac{d(e\phi/T_e)}{d(r/\lambda_d)}\right|_Q \to 0,$$

one finds the conservation equation

$$\frac{\epsilon_0}{2}\left(\frac{d\phi}{dr}\right)^2 = U(e\phi) - U(e\phi_Q), \tag{4.18}$$

where

$$U(e\phi) = n_p T_p + m_e n_s v_{rs}^2 + m_i n_i v_{ri}^2$$

is the Sagdeev's potential. Equation (4.18) expresses the balance of the dynamic and electric pressures of the whole plasma across the sheath. Notice that the first derivative of U measures the local electric charge: $U(e\phi)' = n_p + n_s - n_i$. Also, the electric field at the wall measures the total electric charge in the sheath:

$$-\frac{\epsilon_0}{2}\frac{d\phi}{dr}\bigg|_W = \int_Q^W (n_i - n_p - n_s) dr. \tag{4.19}$$

Two boundary conditions at point Q are related to $U(e\phi)$. First, plasma quasineutrality is achieved there,

$$U_Q' \equiv n_{pQ} + n_{sQ} - n_{iQ} = 0. \tag{4.20}$$

Second, with the presence of two electron populations in the sheath, the Bohm condition takes the form

$$U_Q'' \equiv \frac{n_{pQ}}{T_p} - \frac{n_{sQ}}{m_e v_{rsQ}^2} - \frac{n_{iQ}}{m_i v_{riQ}^2} = 0. \tag{4.21}$$

Finally, to match correctly the solutions of presheath and sheath, we must define the relationships among the magnitudes of the different electron populations at both sides of point Q. These conditions are

$$\begin{aligned} n_{eQ} &= n_{pQ} + n_{sQ}, \\ g_{eQ} &= g_{pQ} + g_{sQ} = (1-\delta_w) g_{pQ}, \\ \frac{n_{eQ}}{T_e} &= \frac{n_{pQ}}{T_p} - \frac{n_{sQ}}{m_e v_{rsQ}^2}. \end{aligned} \tag{4.22}$$

The last expression makes equivalent the two forms of the Bohm condition, Eqs.(4.7) and (4.21), and determines $T_e(T_p)$. One can see that $T_e > T_p$, as expected from the grouping of the primary and secondary populations into a single one.

Notice that $e-$ and $p-$ magnitudes coincide for $\delta_w = 0$, as it should be. Let us use this case to justify that the conditions defining the transition presheath/sheath (i.e. point Q) are unique. On the one hand, a solution for the presheath exists only for $v_{riQ} \leq \sqrt{T_e/m_i}$; on the other hand, a solution in the sheath, around point Q, requires that $U_Q'' \geq 0$, which (for $\delta_w = 0$) states that $v_{riQ} \geq \sqrt{T_e/m_i}$. Therefore, $v_{riQ} = \sqrt{T_e/m_i}$ is the only valid transition condition.

The sheath equations and boundary conditions have shown that δ_w, T_e, and n_{eQ} fully characterize the sheath solution (except for the marginal parameter $\bar{T}_w/T_e \ll 1$). Furthermore, using T_e and n_{eQ}, and the related Debye length

$$\lambda_d = \sqrt{\epsilon_0 T_e / e^2 n_{eQ}},$$

to non-dimensionalize the sheath equations, the dimensionless solution depends on just the secondary emission yield, δ_w. In particular, the inner spatial variable to be used is

$$y = \frac{r - r_W}{\lambda_d}. \tag{4.23}$$

Taking into account that $U'_Q, U''_Q = 0$, the potential around point Q comes from the expansion

$$\frac{\epsilon_0}{2}\left(\frac{d\phi}{dr}\right)^2 \simeq \frac{U'''_Q}{6}(e\phi - e\phi_Q)^3, \tag{4.24}$$

of Eq.(4.18), with $U'''_Q < 0$ for an ion-attracting sheath. For each δ_w, the potential profile $\phi(y)$ in the sheath is obtained by determining, first, the sheath potential jump, $\phi_{WQ} = \phi_Q - \phi_W$, and performing, then, a numerical quadrature of Eq.(4.18), from the vicinity of point Q towards point W, using the above expansion as initial condition.

Figure 4.5 shows the potential profile $\phi(y)$ in the sheath (between points W and Q, with $y_Q = -\infty$) for three values of δ_w. Thus, the whole potential profile, from the channel center to the wall, depends on the values of δ_w and $\tilde{\nu}_r$, and is obtained by matching the respective presheath and sheath profiles.

Figure 4.6 shows the evolution of the main sheath parameters with δ_w up to

$$\delta_w = \delta_w^* \simeq 0.983, \tag{4.25}$$

when the electric field at the wall boundary is zero, $d\phi/dy|_Q = 0$, which corresponds to the charge saturation limit (CSL), to be discussed below. Fig. 4.6 shows that n_{pQ}/n_{eQ} and T_{pQ}/T_{eQ} remain very near unity up to $\delta_w \sim 0.9$, and then the contribution of the secondary emission grows to a 10-15% for the CSL. This means that the properties of the electron population in the presheath are mainly determined by primary electrons, which adds reliability to our model of a unique electron population in the presheath.

For $\delta_w = 0$, the sheath potential is large, $e\phi_{WQ}/T_e \sim 5.28$. For $\delta_w > 0$, the sheath potential satisfies

$$\frac{e\phi_{WQ}}{T_p} = \ln\sqrt{\frac{m_i}{2\pi m_e}} + \ln(1 - \delta_w) + \ln\left[\frac{n_{pQ}}{n_{eQ}}\sqrt{\frac{T_p}{T_e}}\right]. \tag{4.26}$$

Since the last term on the right side is small for any δ_w, the first term on the right side dominates until the secondary yield satisfies $1 - \delta_w \sim 10^{-2}$, that is up to the vicinity of the charge saturation limit. This explains why the potential profile does not change significantly until δ_w does not approach the CSL. The potential drop in that limit is $e\phi^*_{WQ}/T_e \sim 0.88$.

4.2.3 The charge saturation regime

As the secondary emission yield increases, the electron density near the wall increases and the electric field at the wall decreases, as shown in Fig. 4.6, until it becomes zero at the CSL. From Eq.(4.18), the condition for charge saturation is

$$0 = U(e\phi_W) - U(e\phi_Q),$$

or, in terms of the dynamic pressures of the different species,

$$T_p(n_{pQ} - n_{pW}) + m_e g_s(u_{sQ} - u_{sW}) = m_i g_i(u_{iW} - u_{iQ}). \tag{4.27}$$

Since the electric field at the wall depends just on δ_w, the charge saturation limit corresponds to a certain value of that parameter, as we saw before.

To explain the value obtained for δ_w at the CSL, Eq.(4.25), let us recall the classical CSL problem for planar sheaths with $e\phi_{WQ}/T_p \gg 1$ and g_s independent of g_p. For them, Eq. (4.27) simplifies into $m_i g_i u_{iW} \simeq m_e g_s u_{sQ}$, where from the ion and electron counter-streaming fluxes satisfy

$$\left|\frac{g_i}{g_s}\right| \simeq \sqrt{\frac{m_e}{m_i}}, \tag{4.28}$$

which is known as the Langmuir condition. Physically, this law is explained by two facts: on the one hand, integrating Poisson equation the total electric charge in a charge-saturated sheath is zero, so the average densities of accelerated ions and electrons are the same; on the other hand, the average kinetic energies of ions and electrons are the same and of the order of the potential jump. For $e\phi_{WQ}/T_p = O(1)$, more terms in Eq.(4.27) will contribute to the fluxes ratio but we can expect the Langmuir condition (4.28) to be still verified, except for a factor of order one. In our case, applying both the Langmuir and the zero-current conditions, the CSL is expected to happen for

$$\sqrt{\frac{m_e}{m_i}} \sim \frac{g_i}{g_s} \sim \frac{1-\delta_w^*}{\delta_w^*} \sim 1 - \delta_w^*, \tag{4.29}$$

in agreement with the value given by Eq.(4.25).

Let us discuss now the plasma response once the CSL has been attained. For the real case $\bar{T}_w > 0$, a secondary emission yield larger than δ_w^* leads to a potential profile with a minimum near the wall (at a point W', let us say), which acts as a potential barrier to turn back to the wall the excess of secondary flux. The actual secondary flux, g_s', reaching the presheath is the flux at point W'. Since $d\phi/dy|_{W'} = 0$, the secondary flux between W' and Q satisfies CSL conditions, that is Eqs. (4.14) and (4.25)

$$g_s' = -\delta_w^* g_p.$$

The typical size of the potential barrier, to turn back the excess of flux, $|g_s' - g_s|$, is

$$e(\phi_W - \phi_{W'}) \sim \bar{T}_w.$$

Then, in the asymptotic limit $\bar{T}_w/T_p \to 0$, the region W'W is negligible and the CSL (in Fig. 4.6, for instance) instead of identifying a single operation point, identifies a whole domain of operation, the charge-saturated regime (CSR), satisfying $\delta_w = \delta_w^*$ at all operation points. Therefore, the unified expression of the secondary yield for the non-CSR and CSR is

$$\delta_w(T_p) = \min\left\{\delta_w^*, \left(\frac{T_p}{E_w}\right)^p\right\}. \tag{4.30}$$

Although Fig. 4.6 gives a complete information of the sheath solution for the two regimes, a clearer view of the change of behavior at the SCL is given by Fig. 4.7, which shows the evolution of ϕ_{WQ} with T_e for different E_w; one has

$$e\phi^*_{WQ}/T_e \sim 0.88$$

at all points of the CSR.

A final but very relevant consequence of the existence of the charge-saturation regime is that the electron-repelling sheath exists always, contrary to what we expected previously in Ref. [12]. The charge-saturated sheath will limit particle and heat losses in the high T_e range.

4.3 Wall-source terms in the axial model

Once the radial profiles are known, we can evaluate the source terms of Eqs.(2.21)-(2.24). The quasiplanar approximation will be used.

4.3.1 Particle losses

The ion and electron (negative) gains per unit of volume in a radial section are, Eq. (2.21),

$$\hat{S}_w \simeq -\frac{2}{d}[n_i v_{ri}]_M^W = -\frac{2}{d}g_i,$$

or, using Eq. (4.1),

$$\hat{S}_w \simeq -\frac{2}{d}\int_M^W n_i \nu_w dr = -\hat{n}_i \nu_w, \tag{4.31}$$

where $\hat{n}_i = \hat{n}_e$ is the average plasma density in a radial section. From the two above expressions one has

$$\frac{\hat{n}_i}{n_{iM}} = \frac{2}{\tilde{\nu}_w}\frac{n_{iQ}}{n_{iM}}, \tag{4.32}$$

and $\hat{n}_i/n_{iM}$ depends only on $\tilde{\nu}_r$ and is of order unity.

The production frequency satisfies

$$\nu_w = \nu_0 \tilde{\nu}_w(\tilde{\nu}_r), \tag{4.33}$$

with [Eq.(4.12)]

$$\nu_0 \simeq \left(\frac{15\text{mm}}{d}\right)\left(\frac{T_e}{E_i}\right)^{1/2} \times 2 \times 10^5 \text{ s}^{-1}$$

and $\tilde{\nu}_w(\tilde{\nu}_r)$ given by Eq. (4.11). The scaling law $v_{ri} \propto \sqrt{T_e}$, suggests to approximate $\tilde{\nu}_r$, defined in Eq. (4.4), by

$$\tilde{\nu}_r(x) \simeq \frac{1}{\nu_0}\left(\nu_i + \nu_{cx} + \frac{v_{xi}}{\sqrt{T_e}}\frac{\partial\sqrt{T_e}}{\partial x}\right), \tag{4.34}$$

an expression that can be made independent of r. The last term includes the ion Mach number of the axial flow which is large near the exit. Therefore the slope of $T_e(x)$ affects strongly the particle losses there.

The losses in plasma current (per unit of axial length) can be calculated from

$$-e\hat{S}_w A_c \simeq \Big(\frac{A_c}{40\text{cm}^2}\Big)\Big(\frac{\hat{n}_e}{10^{18}\text{m}^{-3}}\Big) \times \Big(\frac{\nu_w}{10^5\text{s}^{-1}}\Big) \times 0.64\text{A/cm},$$

with A_c the cross-section area of the channel (the reference values used here are typical of a SPT-100 thruster). Unless the friction parameter $\tilde{\nu}_r$ is large, particle losses are going to be high.

4.3.2 Near-wall conductivity

The gain per unit of volume in azimuthal momentum of the electrons in a radial section, due to the fluxes of primary and secondary electrons, Eq.(2.23), is

$$\hat{M}_{w\theta e} = -\frac{2}{d}[m_e n_e v_{re} v_{\theta e}]_M^W \simeq -\frac{2}{d} m_e g_p \hat{v}_{\theta e},$$

for $\bar{T}_w/T_p \to 0$.

The equations for electron current follow the closed drift approximation. Taking into account radial effects, they can be written as

$$0 = e\hat{n}_e \frac{d\hat{\phi}}{dx} - \frac{d}{dx}\hat{n}_e T_e + \omega_e m_e \hat{n}_e \hat{v}_{\theta e},$$

$$0 = -m_e \hat{n}_e(\omega_e \hat{v}_{xe} + \nu_e \hat{v}_{\theta e}) + \hat{M}'_{w\theta e},$$

where the azimuthal 'friction' force due to the walls, satisfies

$$\hat{M}'_{w\theta e} \equiv \hat{M}_{w\theta e} - m_e \hat{S}_{we} \hat{v}_{\theta e} = \nu_{wm} m_e \hat{n}_e \hat{v}_{\theta e}, \tag{4.35}$$

with

$$\nu_{wm} = \nu_w \beta_m(\delta_w), \tag{4.36}$$

the related frequency, and

$$\beta_m(\delta_w) = \frac{\delta_w}{1-\delta_w}$$

an enhancement function, shown in Fig. 4.8, due to secondary emission, which can multiply the production frequency by a factor up to 60 in the CSR.

The 'friction' frequency adds a second term to the electron axial current, which now satisfies

$$e\hat{n}_e \hat{v}_{xe} \simeq \frac{\nu_e + \nu_{wm}}{\omega_e^2} e\Big(e\hat{n}_e \hat{E}_x - \frac{d\hat{p}_e}{dx}\Big). \tag{4.37}$$

This contribution is the 'near-wall conductivity'(NWC) of Ref. [33]. Here, the NWC does not present radial oscillations along the cross-section, because ν_{wm} represents an average value.

Since typical values of ν_e are of order 10^7s^{-1}, the near-wall conductivity will be a marginal effect except for the charge-saturated regime and a large friction parameter, $\tilde{\nu}_r$.

4.3.3 Energy losses

The (negative) gain in electron internal energy, per unit of volume, due to wall interaction, satisfies

$$Q'_{we} \simeq -\frac{2}{d}\Big\{ \big[\frac{5}{2} n_e T_e v_{re} + q_{re}\big]_M^W - \int_M^W v_{re}\frac{\partial n_e T_e}{\partial r}dr \Big\}, \tag{4.38}$$

with q_{re} accounting formally for heat conduction. The computation of the different terms yields

$$\hat{Q}'_{we} = -\nu_{we}\hat{n}_e T_e, \tag{4.39}$$

where

$$\nu_{we} = \nu_w \left[\beta_e(\delta_w) + \beta'_e(\tilde{\nu}_r)\right] \tag{4.40}$$

is the related frequency, and

$$\beta_e(\delta_w) = \frac{T_p}{T_e}\Big(\frac{e\phi_{WQ}}{T_p} + \frac{2}{1-\delta_w}\Big),$$

$$\beta'_e(\tilde{\nu}_r(\alpha)) = \int_0^1 \Big(\frac{1+\alpha}{\alpha u^2+1}\Big)^{\frac{3\alpha+1}{2\alpha}} u^2 du$$

are two enhancement functions. The first one, $\beta_e(\delta_w)$, plotted in Fig. 4.8, depends on the sheath characteristics; it goes from $\beta_e \simeq 7.28$, for $\delta_w = 0$, $\beta_e = \beta_e^* \sim 104.5$, for $\delta_w = \delta_w^*$. The second one, $\beta'_e(\tilde{\nu}_r)$, depends on the presheath characteristics and has a lesser effect in Q'_{we}: we find $\beta'_e \ll \beta_e$ for $\tilde{\nu}_r = O(1)$, and $\nu_w\beta'_e \sim \nu_0(\ln\tilde{\nu}_r)/\tilde{\nu}_r^2 \ll \nu_0$ for $\tilde{\nu}_r \gg 1$. For the sake of clarity we suggest to use the expression

$$\beta_e(\delta_w) \sim 5.62 + \frac{1.65}{1-\delta_w}, \tag{4.41}$$

which approximates the exact function with an error less than 10%.

The losses in internal energy (per unit of axial length) can be calculated from

$$-\hat{Q}'_{we}A_c \simeq \Big(\frac{A_c}{40\mathrm{cm}^2}\Big)\Big(\frac{\hat{n}_e}{10^{18}\mathrm{m}^{-3}}\Big)\Big(\frac{\nu_{we}}{10^7\mathrm{s}^{-1}}\Big) \times \Big(\frac{T_e}{E_i}\Big)^{3/2} \times 774\mathrm{W/cm}.$$

Fig. 4.9 computes $|\hat{Q}'_{we}A_c|$ in terms of T_e for different values of the characteristic yield energy, E_w. As in the case of the sheath potential ϕ_{WQ}, Fig. 4.7, there is a change in behavior from the non-CSR to the CSR. For a given T_e and below the charge-saturation regime, energy losses increase with E_w decreasing. Within the charge-saturation regime energy losses are independent of E_w and grow with $T_e^{3/2}$. Figure 4.9 shows that the energy losses can be enormous if there is not a large ion friction, or any other phenomenon able to reduce significantly the electron current to the wall.

For wall heating considerations, the important magnitude is the total energy deposited by electrons, which is the sum of the heat loss, $\hat{Q}'_{we}$, and the loss of azimuthal energy, $m_e v_{\theta e}^2 \hat{n}_e \nu_w$.

4.4 Conclusions

We have presented a model of the radial structure of the plasma interaction with dielectric walls, supported in three pillars: (i) a two-scale asymptotic analysis; (ii) a new model to account for trapped secondary electrons; and (iii) the inclusion of ion radial 'friction', due to collisional processes and axial transport. The presheath properties depend on the ion friction parameter $\tilde{\nu}_r$, whereas the sheath properties depend on the effective secondary emission yield, δ_w. A large friction increases the presheath potential drop, and reduces the plasma current to the wall. The charge saturation limit is attained for $\delta_w \simeq 0.983$, and marks the transition to a charge-saturated regime, with a constant ratio for (sheath potential drop)/(plasma temperature). As a consequence, the electron-repelling sheath never disappears.

Particle exchanges at lateral walls lead to losses in particles, energy, and azimuthal momentum. The near-wall conductivity has been determined from the loss in azimuthal momentum. It seems to be a moderate effect except for operation near or under the charge-saturation regime. For typical thruster conditions the model predicts too large losses of particles and energy, unless a large ion 'radial friction' is assumed. The coupling of the radial and axial models, now underway, will show whether a large radial friction is attainable.

Total trapping of secondary electrons does not seem the case in practice, according to typical values of the total electron collision frequency. Partial trapping implies a double population of secondary electrons traveling freely from wall to wall. This more general case, now under study, will certainly modify the radial structure and could provide and additional mechanism to inhibit radial transport to the walls.

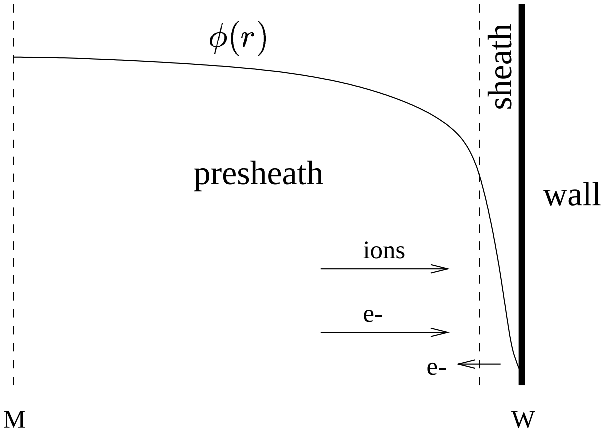

$\phi(r)$
sheath
presheath
wall
ions
e-
e-
M
W

Figure 4.1: Sketch of the radial model in the quasiplanar case. Point M represents the mid-plane of the channel. The sheath is the region of large gradients of $\phi(r)$.

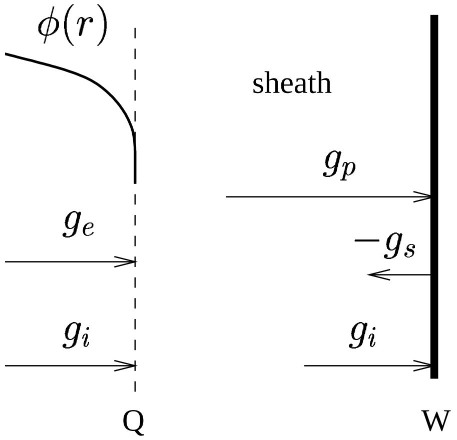

$\phi(r)$
sheath
g_p
g_e
$-g_s$
g_i
g_i
Q
W

Figure 4.2: Two-scale analysis: point Q is the presheath/sheath transition with $d\phi/dr \to \infty$ in the quasineutral scale. g_p and g_s are the fluxes of primary and secondary electrons at the wall; in the presheath, both populations are grouped in a single one with $g_e = g_p + g_s$.

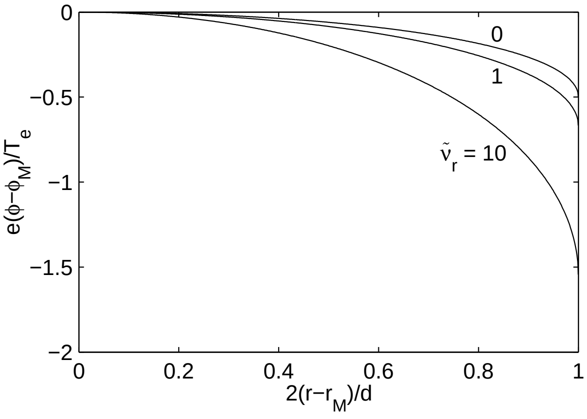

Figure 4.3: Presheath: Potential profile for different values of the dimensionless friction parameter.

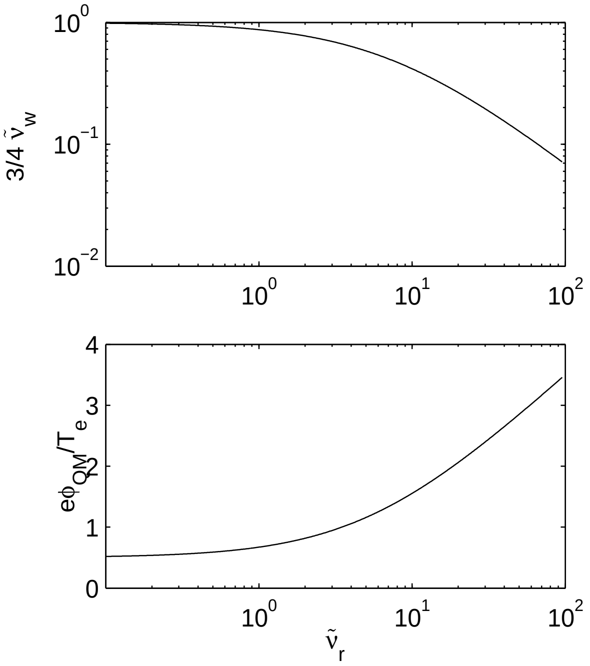

Figure 4.4: Presheath: Influence of the radial friction frequency on the production frequency and the potential drop across the presheath.

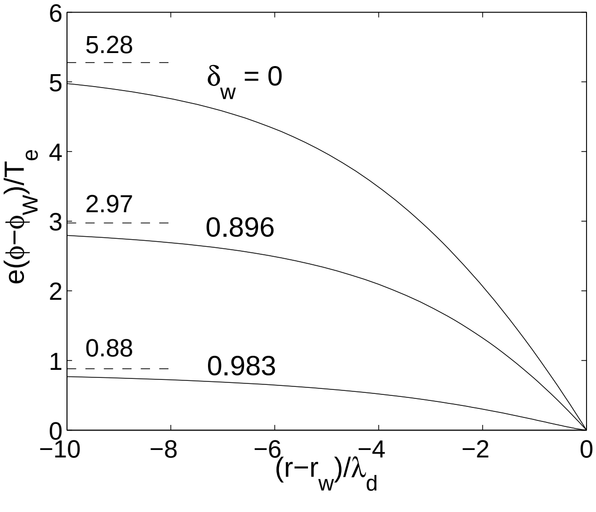

Figure 4.5: Sheath: Potential profile for different values of the secondary emission yield. For $\delta_w = \delta_w^* \simeq 0.983$ it is $d\phi/dy|_W = 0$, marking the charge-saturation limit. Point Q is here at $y_Q = -\infty$.

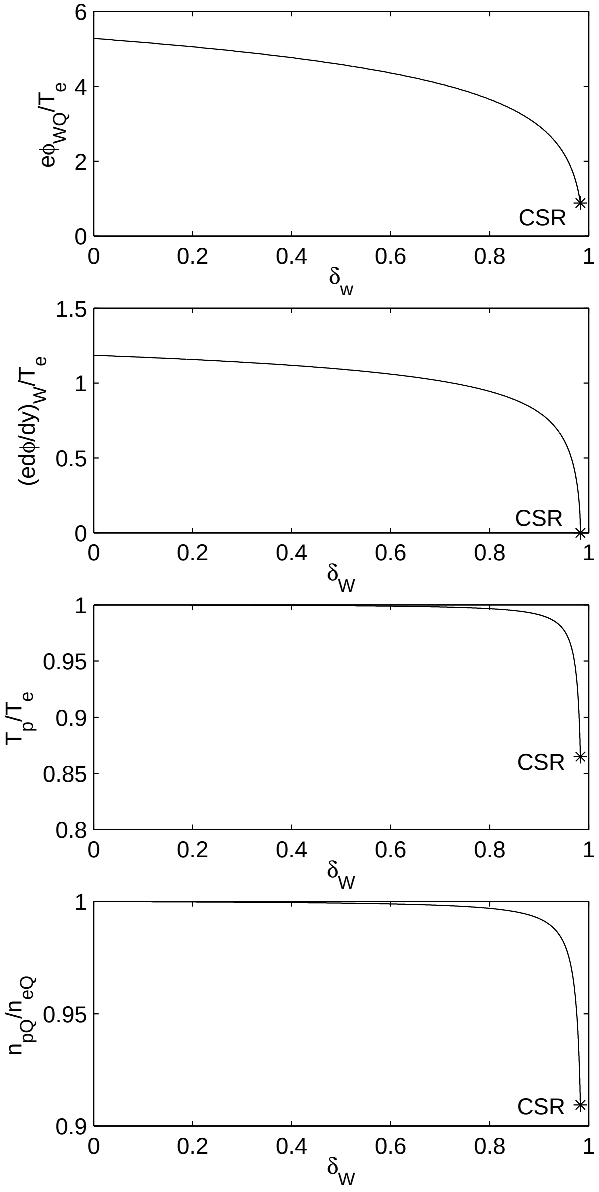

Figure 4.6: Sheath: Influence of the secondary emission yield on potential drop, electric field at the wall, and electron temperatures and densities. Point CSR represents the charge-saturation regime; $e\phi_{WQ}/T_e|_{CSR} \simeq 0.879$, $T_p/T_e|_{CSR} \simeq 0.865$.

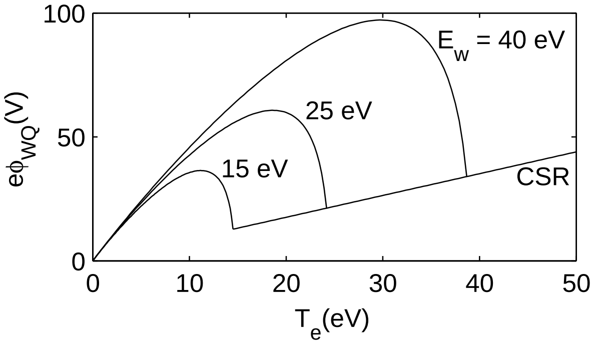

Figure 4.7: Evolution of the sheath potential drop with the plasma temperature for different ceramic materials (i.e. E_w). The straight line corresponds to the CSR.

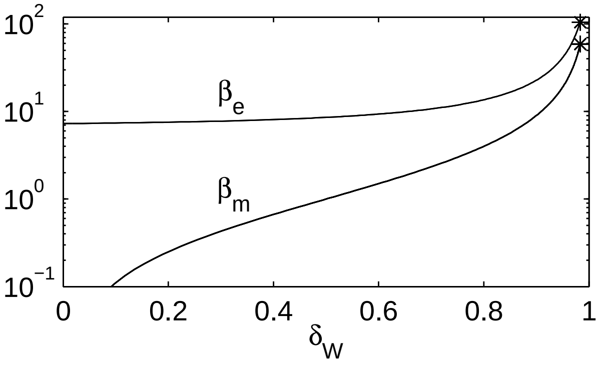

Figure 4.8: Enhancement functions for the effective frequencies accounting for near-wall-conductivity, ν_{wm}, and energy losses, ν_{we}.

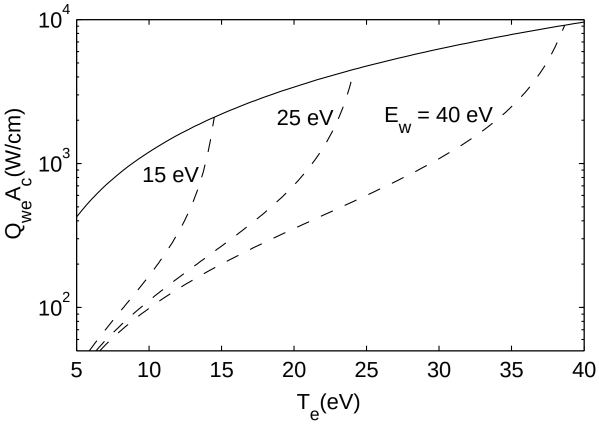

Figure 4.9: Energy losses per unit of channel length for different wall materials, $A_c = 40$ cm^2, $d = 15$mm, $\hat{n}_e = 10^{18}$m^{-3}, and $\tilde{\nu}_w = 1$. The solid line corresponds to the CSR. Energy losses are proportional to $\tilde{\nu}_w$.

Chapter 5

EFFECTS OF LATERAL LOSSES

5.1 Governing equations

Here we add the effects of the plasma interaction with the thruster walls, studied in the previous chapter, into the basic steady-state model treated in Ch. 3. For sake of clarity in the exposition and to avoid continuous references to previous chapters, we give a brief but complete account of the model equations.

The stationary, macroscopic equations for the quasineutral plasma between the entrance to the anode sheath (point B) and the external neutralization surface (point P) are

$$\frac{1}{A}\frac{d}{dx}(An_ev_{xi}) = \frac{1}{A}\frac{d}{dx}(An_ev_{xe}) = -\frac{1}{A}\frac{d}{dx}(An_nv_n) = n_e(\nu_i - \nu_w), \tag{5.1}$$

$$\frac{1}{A}\frac{d}{dx}(Am_in_ev_{xi}^2) = -en_e\frac{d\phi}{dx} + m_in_e(\nu_iv_n - \nu_wv_{xi}), \tag{5.2}$$

$$\frac{1}{A}\frac{d}{dx}(Am_in_nv_n^2) = m_in_e(\nu_wv_{nw} - \nu_iv_n), \tag{5.3}$$

$$0 = -\frac{d}{dx}n_eT_e + en_e\frac{d\phi}{dx} - \nu_dm_en_ev_{xe}, \tag{5.4}$$

$$\frac{1}{A}\frac{d}{dx}A\left(\frac{3}{2}T_en_ev_{xe}\right) = -n_eT_e\frac{dv_{xe}}{dx} + \nu_dm_en_ev_{xe}^2 - \nu_in_e\alpha_iE_i - \nu_{we}n_eT_e. \tag{5.5}$$

The ionization frequency follows

$$\nu_i = n_nR_i(T_e);$$

the axial diffusion frequency for the magnetized electrons satisfies

$$\nu_d = \frac{\omega_e^2}{\nu_e + \nu_{wm}}, \tag{5.6}$$

with

$$\nu_e = \nu_{en} + \nu_{ei} + \alpha_B\omega_e$$

the electron collision frequency, grouping contributions from $e-n$ and $e-i$ collisions, and Bohm anomalous diffusion; ν_w, ν_{wm} and ν_{we} are frequencies accounting for particle losses, near-wall conductivity, and energy losses at the lateral walls; and v_{nw} is the axial velocity of ions after wall recombination and accommodation.

The area $A(x)$ and thickness $d(x)$ of the plasma jet cylindrical cross-section, are constant within the channel and satisfy

$$\frac{da}{dx} = \frac{2}{d}\tan\delta, \quad x > L, \tag{5.7}$$

in the plume, with δ the local mean angle of divergence of each boundary, to be defined below and $a = \ln A + const = \ln d + \text{const}$.

The azimuthal components of the electron velocity and the heat flux follow

$$\frac{v_{\theta e}}{v_{xe}} \simeq \frac{q_{\theta e}}{q_{xe}} \simeq -\frac{\omega_e}{\nu_e}, \tag{5.8}$$

with $\omega_e/\nu_e \gg 1$.

5.1.1 Frequencies for wall-source terms

We summarize here the expressions obtained in Ch.4. To help solving the axial model, some approximations are made too. The particle loss frequency satisfies

$$\nu_w = \nu_0\tilde{\nu}_w, \quad \nu_0 = \frac{\sqrt{T_e/m_i}}{d}, \tag{5.9}$$

with ν_0 the reference frequency for the radial motion, and $\tilde{\nu}_w$ a dimensionless factor, which depends on the characteristics of the radial motion. In this work we will take the simplest case

$$\tilde{\nu}_w = \text{const}.$$

Future work will have to take into account the influence of the radial dynamics of ions and secondary electrons on $\tilde{\nu}_w$, that is the functional relation $\tilde{\nu}_w(\tilde{\nu}_r)$, discussed in Ch.4.

The frequencies for near-wall diffusion and heat losses are

$$\begin{aligned} \nu_{wm} &= \beta_m\nu_w, \quad && \beta_m(\delta_w) = \frac{\delta_w}{1-\delta_w}, \\ \nu_{we} &\simeq \beta_e\nu_w, \quad && \beta_e(\delta_w) \sim 5.62 + \frac{1.65}{1-\delta_w}, \end{aligned} \tag{5.10}$$

with β_m and β_e enhancement functions, which depend on the effective secondary emission yield $\delta_w(T_e)$. Assuming that the secondary emission yield for an impinging monoenergetic electron beam of energy E, follows the law

$$\bar{\delta}_w(E) \simeq \sqrt{E/\bar{E}_w},$$

the effective yield for the quasi-Maxwellian population of primary electrons, satisfies Eq.(4.30)

$$\delta_w(T_e) \simeq \min\left\{\delta_w^*, \sqrt{\frac{T_e}{E_w}}\right\},$$

with

$$E_w \sim \frac{2}{3}\bar{E}_w$$

the temperature leading to 100% secondary emission[36] and

$$\delta_w^* \simeq 0.983$$

the upper-bound value of δ_w, corresponding to the charge-saturated regime for the lateral sheaths. Therefore, the maximum values of the enhancement functions are

$$\beta_m^* \sim 60,\ \beta_e^* \sim 105,$$

and the charge-saturation regime corresponds to $T_e \geq 0.967E_w$.

5.1.2 Singular points and boundary conditions

Solving Eqs. (5.1)-(5.5) for the spatial derivatives we obtain a matrix relation of the form

$$(1-M^2)\frac{d\boldsymbol{Y}}{dx} = \boldsymbol{F}(\boldsymbol{Y}), \tag{5.11}$$

where $\boldsymbol{Y} = (T_e, n_e, n_n, v_{xi}, v_{xe}, v_n, \phi)$ groups the 7 plasma variables, $\boldsymbol{F}$ is a regular function and

$$M = \frac{v_{xi}}{\sqrt{5T_e/3m_i}} \tag{5.12}$$

is the Mach number for the ion axial flow. For instance, the equations for n_e and v_{xi} can be written as

$$\frac{1}{n_e}\frac{dn_e}{dx} = \frac{G}{P}\frac{dv_{xi}}{dx} = \nu_i - \nu_w - v_{xi}\Big(\frac{G}{P} + \frac{da}{dx}\Big), \tag{5.13}$$

with $P = T_e(1-M^2)$ and

$$v_{xe}G = \nu_i\Big[\frac{2}{5}\alpha_i E_i + T_e - \frac{3}{5}m_i v_{xe}(2v_{xi} - v_n)\Big] - \nu_d m_e v_{xe}^2 + \frac{3}{5}m_i v_{xi}^2 v_{xe}\frac{d\ln A}{dx} + \frac{2}{5}\nu_{we}T_e - \Big(T_e - \frac{3}{5}m_i v_{xi}v_{xe}\Big)\nu_w. \tag{5.14}$$

Sonic points and boundary conditions are discussed in Chap.3. The seven boundary conditions needed here are:

i)-ii) The injected flow of neutrals at the anode, $\dot{m}$, and their velocity, $v_{nB} = v_{nA}$, are known.

iii) The electron temperature at the neutralization surface, T_{eP}, is known.

iv) The potential drop between points A and P is the discharge voltage, $\phi_A - \phi_P = V_d$.

v) The presheath/sheath transition at point B requires $M_B = -1$, which is the Bohm sonic condition on the ion back-flow.

vi) The potential jump at the anode sheath satisfies Eq.(3.11)

$$\frac{e\phi_{AB}}{T_{eB}} = \ln\frac{\bar{c}_{eB}}{4|v_{xeB}|} > 0,$$

with $\bar{c}_e = \sqrt{8T_e/\pi m_e}$.

vii) There is a regular sonic point inside the channel (point S), which, according to Eq.(5.13), is characterized by

$$G_S = 0 \quad \text{at} \quad M_S = 1. \tag{5.15}$$

In addition, we must define an expression for the angle of divergence δ. Following Ref. [37] we take

$$\tan\delta = \frac{\sqrt{5T_{eE}/3m_i}}{v_{xi}}. \tag{5.16}$$

Notice that discharge current, I_d, position of forward sonic point, x_S, and divergence angle at the channel exit, δ_E, are part of the solution.

5.2 Axial plasma structure

Figure 5.1 shows the first complete results we have obtained with the preceding model of radial losses. Profiles of most plasma variables are shown for a SPT-100 type of thruster. The solution shown here presents moderate wall losses. However, the values selected for the parameters that determine radial losses: $\tilde{\nu}_w \sim 0.17$ and $E_w = 100eV$, were aimed mainly to test the possibility of obtaining valid solutions. Our procedure to obtain these solutions is to carry out a parametric continuation from the solution without wall losses $\nu_w = 0$. Actual values of E_w for BN-based materials are in the range $E_w \sim 2\bar{E}_w/3 \sim$ 15-40 eV. From Eq.(4.11) $\tilde{\nu}_w \sim 0.17$ corresponds to $\tilde{\nu}_r \simeq 50$, and $\nu_r \sim 10^7$Hz, which, from the definition of Eq.(2.59), seems too large; however, partial trapping, not investigated yet could reduce $\tilde{\nu}_w$. Attempts to increase $\tilde{\nu}_w$ and reduce E_w, beyond the case of Fig. 5.1, have encountered different convergence difficulties. One of them is the appearance of complex values for the plasma derivatives at point S preventing the launch of the integration.

The solution of Fig. 5.1 shows that energy losses at lateral walls smooth the temperature profile, the maximum temperature decreasing from about 90 eV with no wall losses, to about 68 eV now, which corresponds to a maximum secondary yield of $\delta_w \sim 0.82$, far (in terms of losses) from the charge-saturation value δ_w^*. Energy losses take place in the acceleration region, where T_e is high. On the contrary, losses in plasma current are concentrated in the rear part of the channel. The (relative) ion back-flow at the inner boundary of the ionization layer is $\eta_{iD} \simeq -0.37$, whereas at the anode is just $\eta_{iB} \simeq -0.05$, which means a current loss in the diffusion region of 1.2 A. The total plasma current deposited at lateral walls, $\int S_w dx$, with

$$S_w = en_e\nu_w A_c$$

plotted in Fig. 5.1, is 2.0 A, about a 38% of the discharge current, $I_d = 5.21$ A, and a 34% of the total ion production (about 5.8 A); Bishaev and Kim[1] estimate, in their experiments, relative current losses of similar magnitude. Notice that the plasma current lost in the lateral walls implies a larger ion production and eventually a larger discharge current, decreasing thus the thrust efficiency.

The electron energy deposited by conduction at lateral walls, $\int Q_w dx$, with

$$Q_w = T_e n_e \nu_{we} A_c$$

plotted in Fig. 5.1, is 144 W, which represents a 9% of the electric power, $I_d V_d \simeq 1.56$ kW; Ref. [1] estimates this energy loss around 20%.

The structure of the plasma discharge in Fig. 5.1 is similar to the one found when there were no lateral losses, Fig. 3.2. It consists of (see Fig. 2.1) anode sheath (AB), anode presheath(BC), diffusion region(CD), ionization layer(DH), acceleration region(HE) and near-plume (EP). Delimiting points inside the channel are $x_A = 0$, $x_C \simeq 0.5$ mm, $x_D \simeq 11.5$ mm, $x_H \simeq 14$ mm. The regular sonic point is downstream the ionization layer, at $x_S \simeq 18.2$ mm. In the acceleration region, volume ionization and ion recombination at lateral walls are rather low, keeping the ionization fraction $\eta_i(x)$ almost constant.

Notice in Eq.(5.14) for G that the presence of two terms for lateral losses gives more flexibility to the balance necessary for a smooth sonic transition (i.e. $G_S = 0$). The drift of point S away from the ionization layer, when lateral losses are included, indicates that electron diffusion (i.e. Joule heating) and lateral energy losses dominate the balance at the sonic transition, that is we have

$$\frac{2}{5}\nu_{we} T_e \sim \nu_d m_e v_{xe}^2$$

at point S.

Potential drops in the different plasma regions are $\phi_{AB} \simeq 1.2$ V, $\phi_{CD} \simeq 0.02$ V, $\phi_{DS} \simeq -61.9$ V, $\phi_{SE} \simeq -137.6$ V, $\phi_{EP} \simeq -101.5$ V, $\phi_{P\infty} \simeq 10$ V. Notice that the potential drop in the ionization layer is moderate and follows the law[37] $\phi_{DH} \sim \frac{5}{6} T_{eH}$.

The thrust, defined as

$$F = (m_i n_i v_i^2 + p_e)_E A_c,$$

is $F = 90.6$ mN and the thrust efficiency (using the definition of Ref. [37]) is $\eta \simeq 0.50$, which comes from the product of utilization efficiency $\eta_u \simeq 0.90$, (electric) current efficiency $\eta_c \simeq 0.73$, energy efficiency $\eta_e \simeq 0.97$, and plume efficiency $\eta_p \simeq 0.86$.

5.3 Influence of control/design parameters

Figures 5.3 to 5.6 show this influence for different parameters. These plots have been obtained from continuation routines, departing from the solution of Fig. 5.1. They can be compared with Figs. 3.3 to 3.8 for zero-losses at the walls, Sec. 3.6. Since wall losses are not very large, most features coincide. We observe that:

1. Influence of the mass flow, Fig. 5.3: Discharge current and thrust increase linearly with the mass flow –in agreement with experiments [25, 38, 39, 2]–. In addition, $\dot{m}$ is one of the few parameters affecting weakly the reverse flow (i.e. η_{iB}). All these features make $\dot{m}$ a very suitable parameter for thruster control. Although wall losses increase with $\dot{m}$ too, the trade-off for thrust efficiency and specific impulse favors larger mass flows.

2. Influence of the discharge voltage, Fig. 5.4: Both thrust and specific impulse grow like $V_d^{1/2}$ –in agreement with experiments [25, 38, 39, 40]–. Experiments [39, 40] show that η presents a maximum for V_d around 300 V. The region of positive slope for low potentials. is not found here, possibly because it corresponds to a regime of partial ionization. The efficiency decrease for large V_d would be due to a larger acceleration region and, as a consequence, larger energy losses to the walls.

3. Influence of the magnetic field strength, Fig. 5.5: larger B_m means an inhibition of axial transport, leading to a larger ionization efficiency and, eventually, a lower discharge current and a larger thrust efficiency favored by lower lateral losses too). Experimentally, B_m is increased until a non-stationary regime is attained[5]; our results suggest that this would correspond to the limit $\eta_{iB} \simeq 0$.

4. Influence of the magnetic field slope Fig. 5.6: The increase of η with L_m indicates that it is the average magnetic field strength what influences basically the plasma response.

5. Influence of the cathode position, Fig. 5.7: it is relevant for short values only. Since we do not have a clear criterion to choose x_P, we suggest to avoid small values.

6. Influence of the channel length, Fig. 5.5: Thrust and efficiency increase moderately with the channel length, mainly because the plasma leaves the thruster more supersonic. Experiments ?? show the function $\eta(L)$ having a maximum. We could not reproduce it here, possibly because wall losses have not increased enough here.

7. Influence of the thruster size, Fig. 5.9: Here, large wall losses make the efficiency to present a maximum for an intermediate size. Notice, however that thruster operating conditions are not optimized for each size.

   Figure 5.10 shows how the pair of parameters (V_d, B_m) should evolve to keep $\eta_{iB} \simeq -0.05$. We expected that increasing both discharge voltage and magnetic strength, η would grow. However, the increase of wall losses keeps the efficiency almost unchanged, but thrust increases.

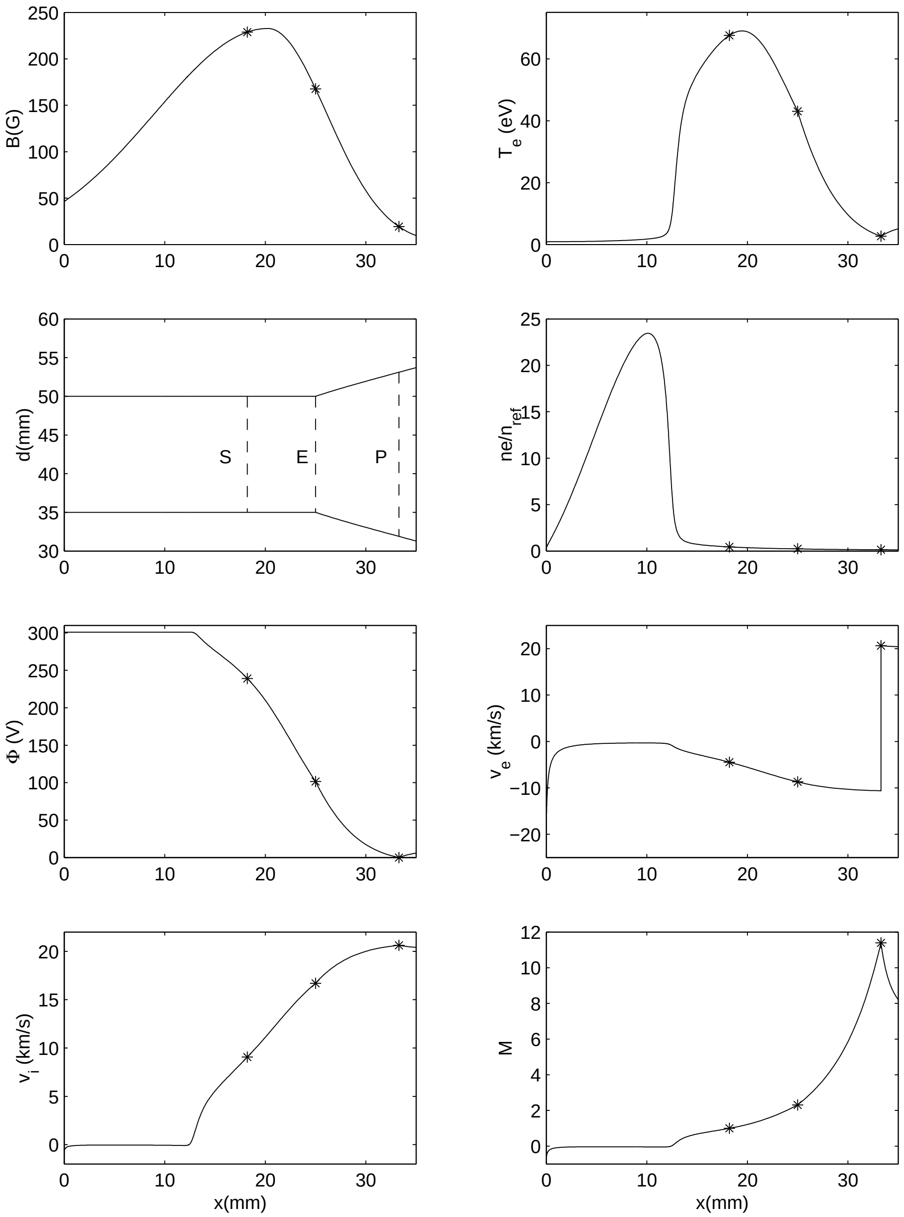

Figure 5.1: Axial structure of the plasma discharge for $L = 25\text{mm}$, $L_{EP} = 8.3\text{mm}$, $A_c = 40.1\text{cm}^2$, $V_d = 300\text{V}$, $\dot{m} = 5.2\text{mg/s}$, $T_{eP} = 2.7\text{eV}$, $16\alpha_B \sim 0.21$, $E_w = 100\text{eV}$, $\tilde{\nu}_w(x) \sim 0.17$, $v_{nw} = v_i$, and $n_{ref} \simeq 4.3 \cdot 10^{18}\text{m}^{-3}$. (continues in Fig.5.2)

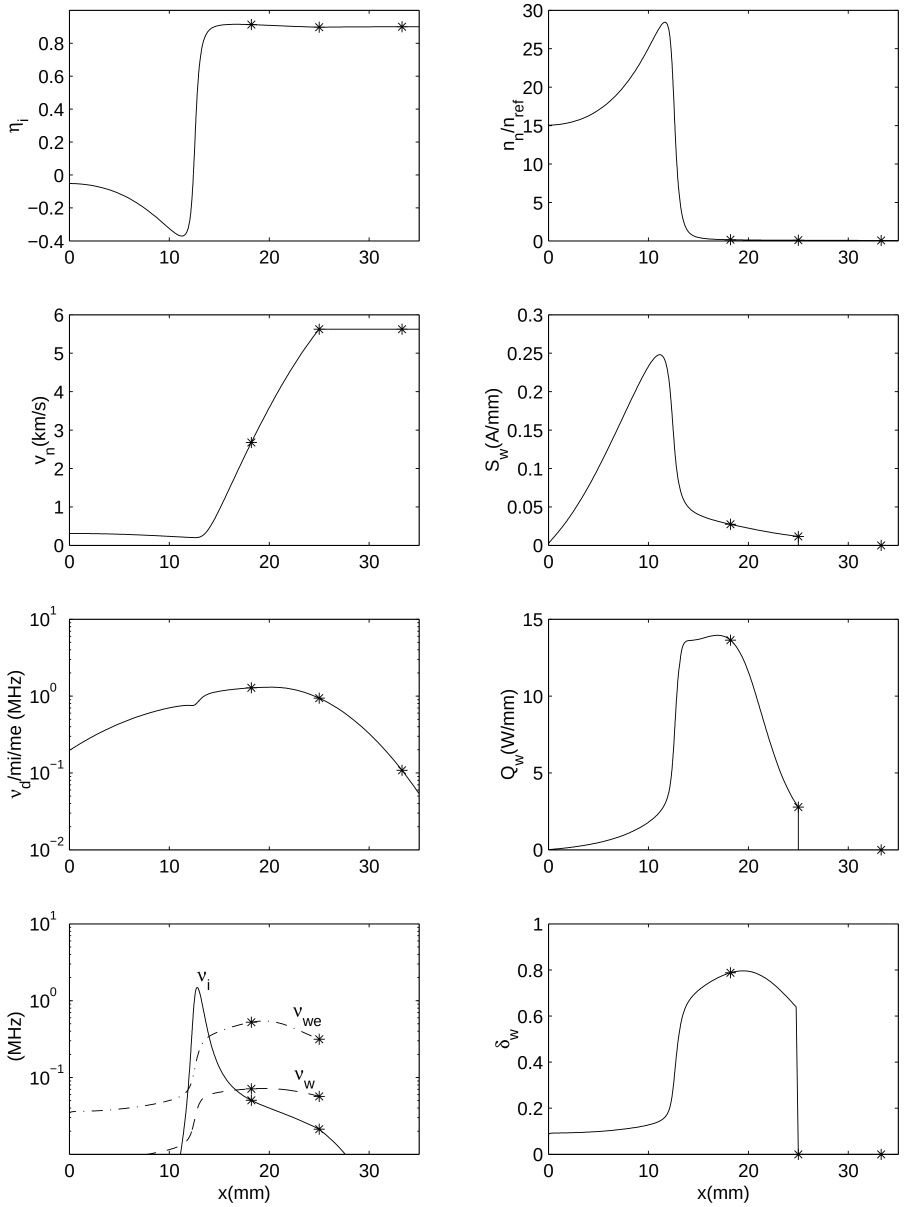

Figure 5.2: Continuation of Fig.5.1.

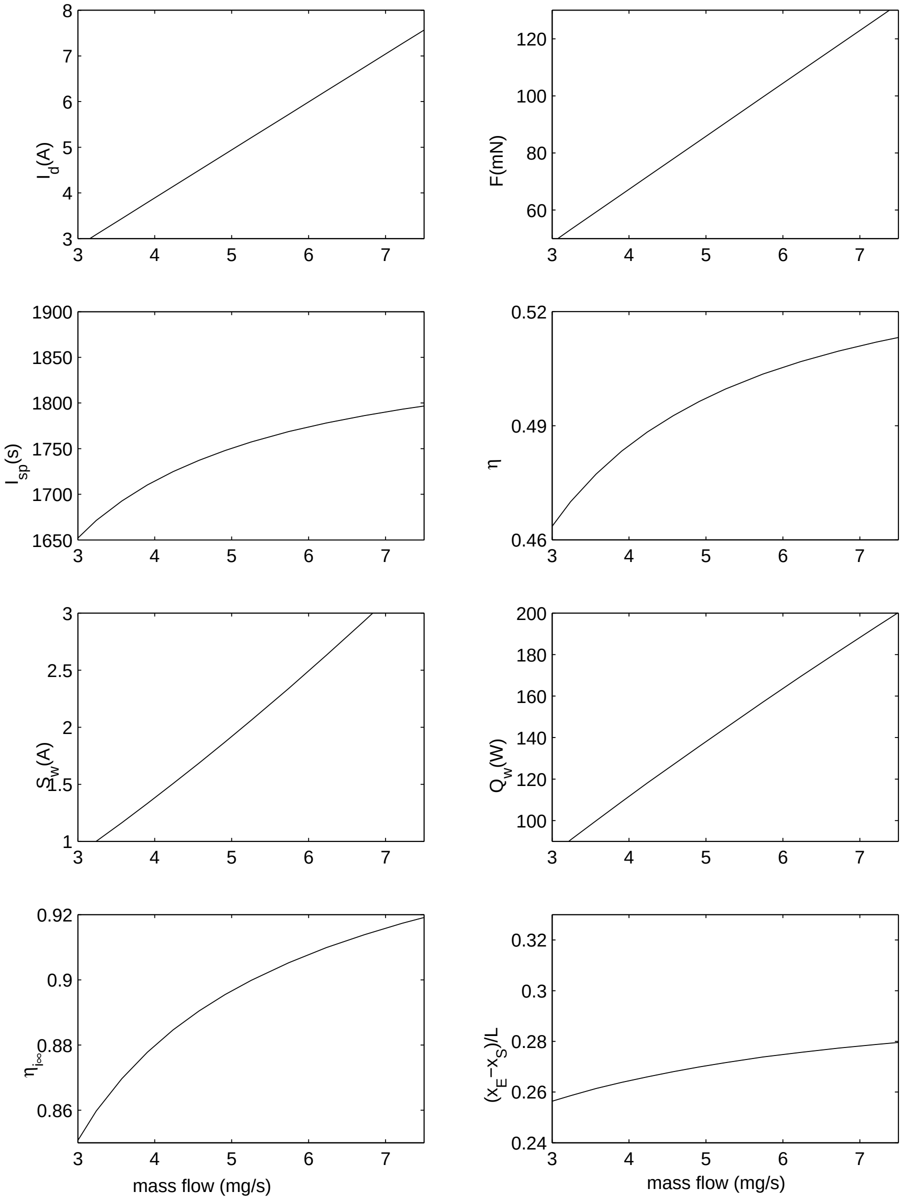

Figure 5.3: Influence of the mass flow. Rest of parameters as in Fig. 5.1.

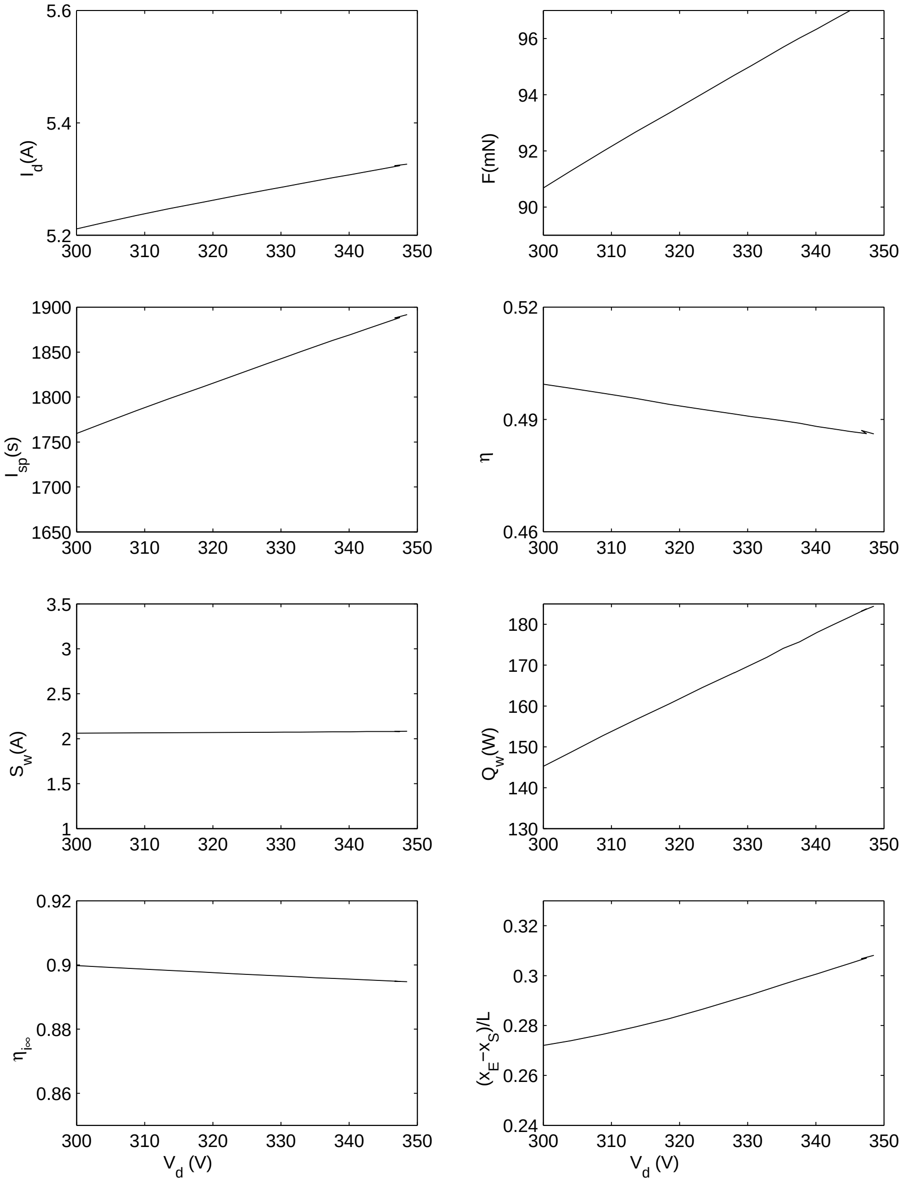

Figure 5.4: Influence of the discharge voltage. Rest of parameters as in Fig. 5.1.

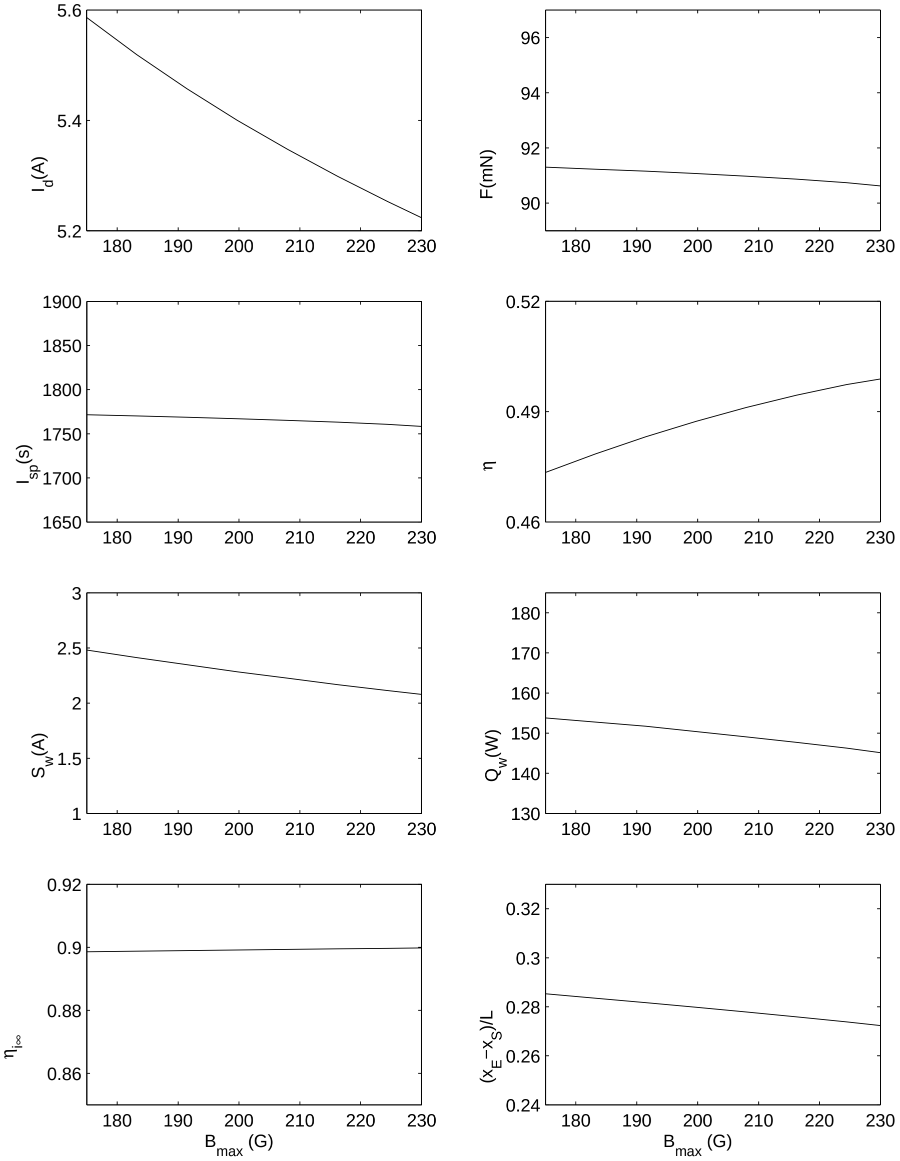

Figure 5.5: Influence of the magnetic field strength B_{max}. Rest of parameters as in Fig. 5.1.

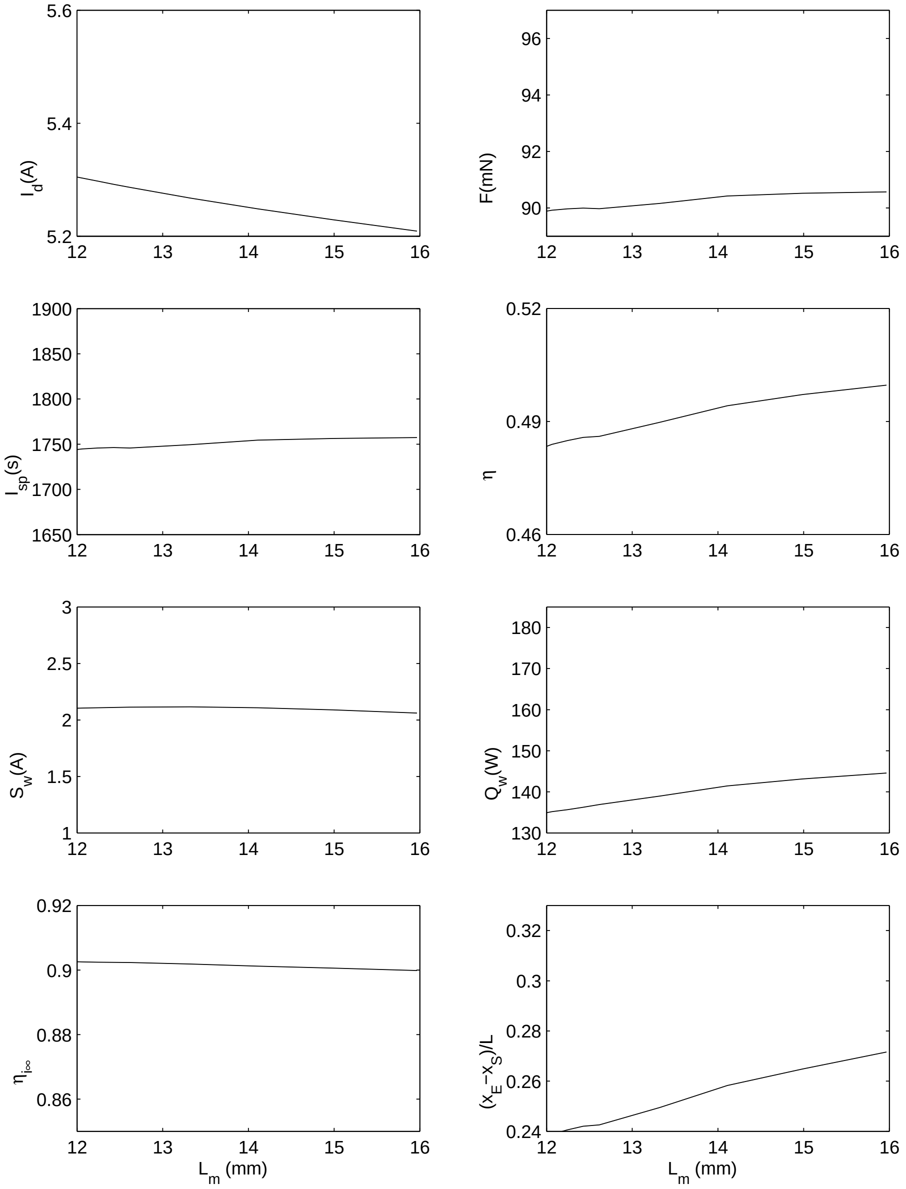

Figure 5.6: Influence of the slope of the magnetic field profile, as defined in Eq.(3.1). Rest of parameters as in Fig. 5.1.

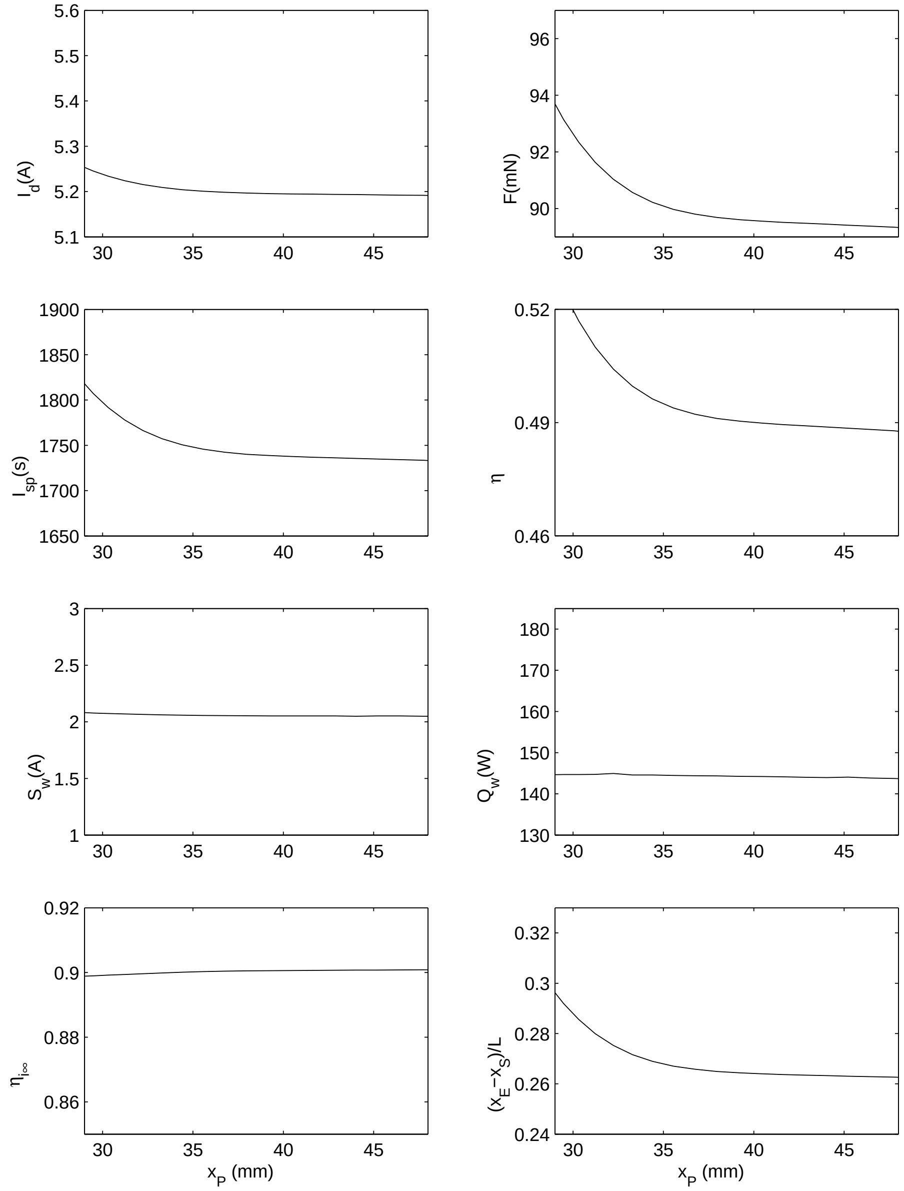

Figure 5.7: Influence of the cathode position x_P. x_A, x_m, and x_E are kept constants. Rest of parameters as in Fig. 5.1.

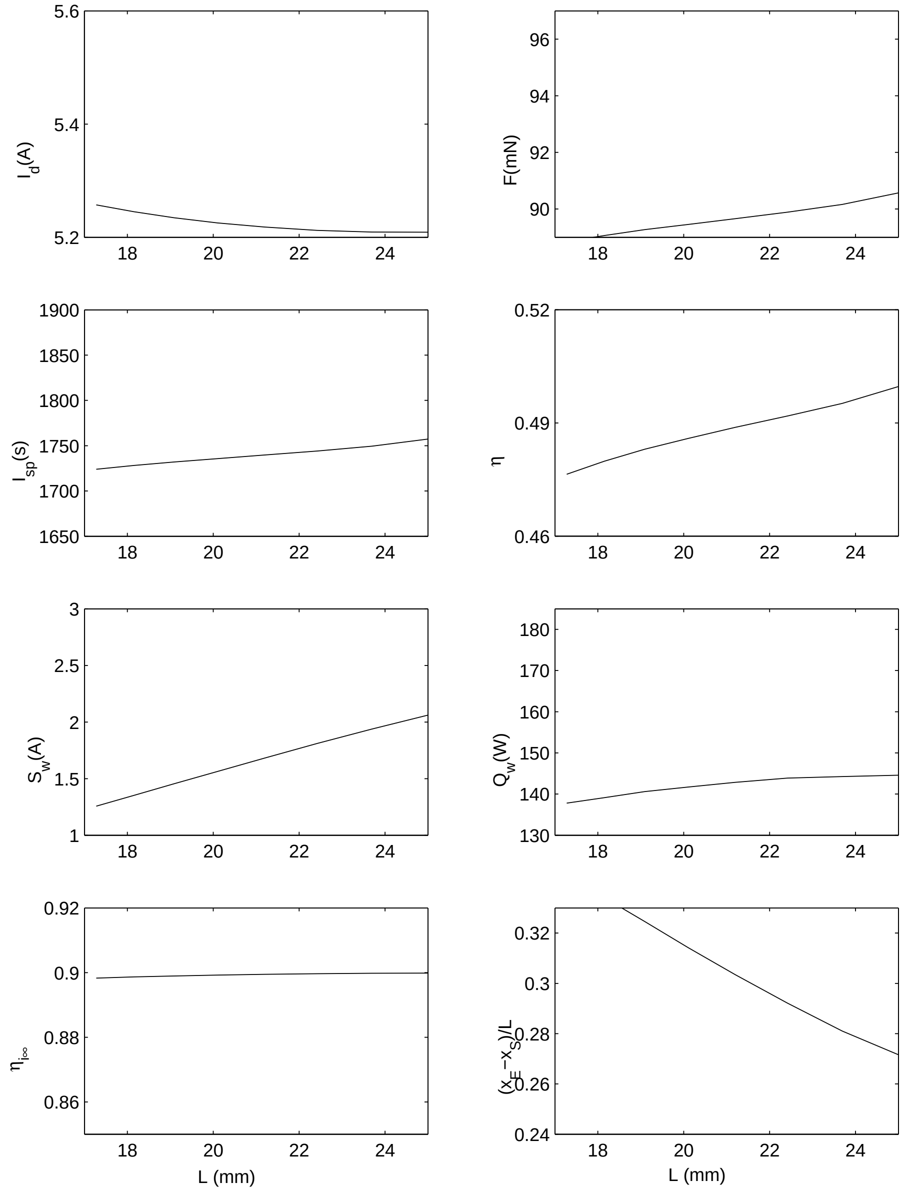

Figure 5.8: Influence of the anode position (i.e. the channel length $L = x_E - x_A$). Here, x_A is moved, while x_m, x_E and x_P are kept fixed. Rest of parameters as in Fig. 5.1.

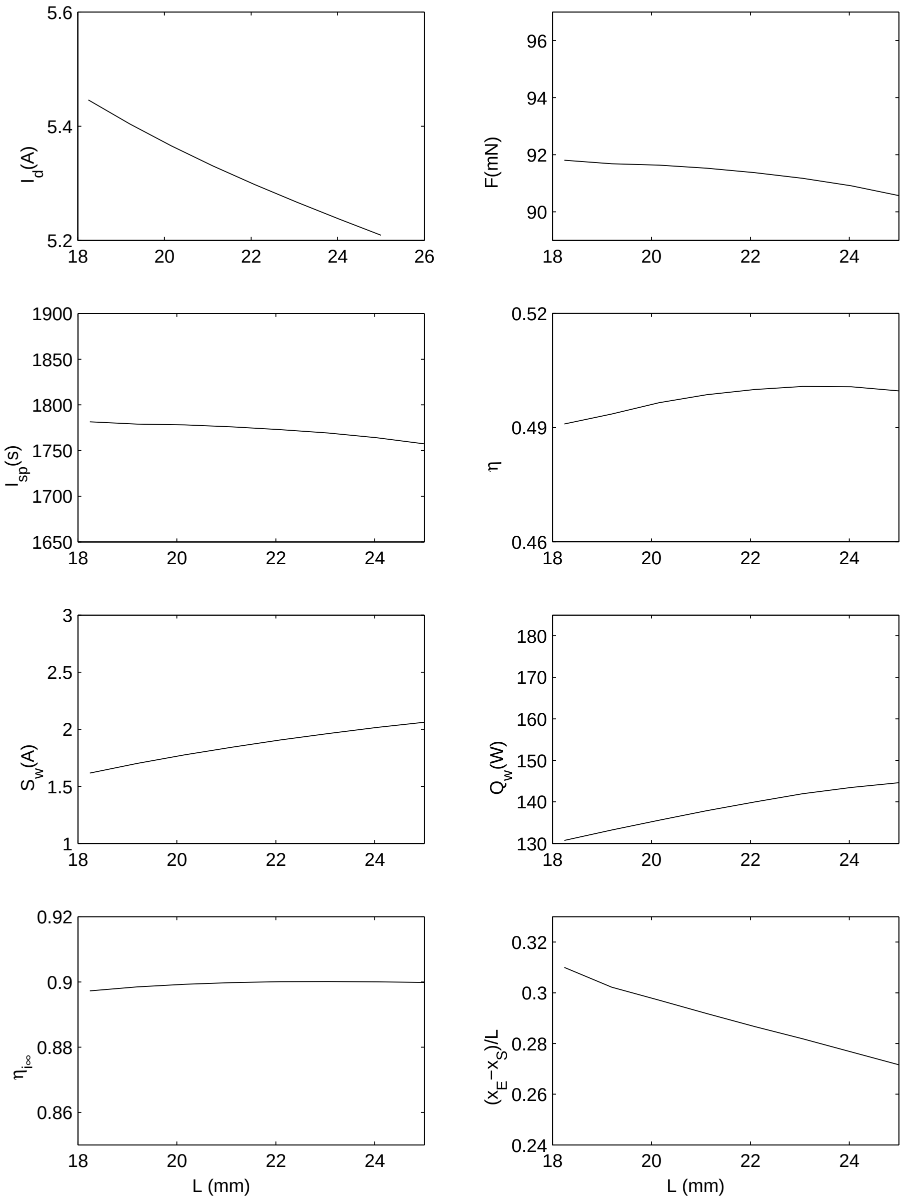

Figure 5.9: Influence of the thruster size. Axial magnitudes L_B, and $x_E - x_m$ are scaled with $L = x_E - x_A$; d is constant. Rest of parameters as in Fig. 5.1.

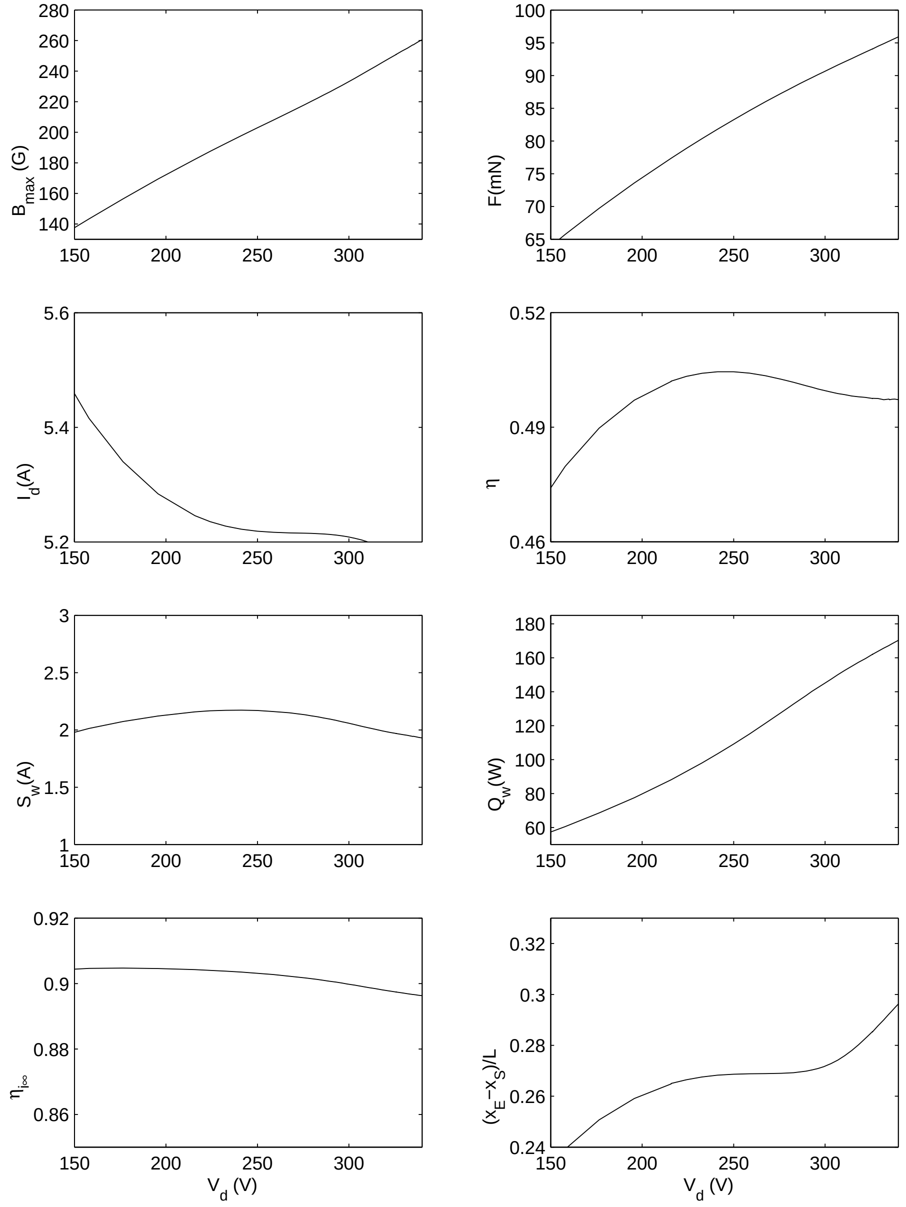

Figure 5.10: Design optimization. Plot on the top-left shows the evolution of the pair (V_d, B_m) to keep η_{iB} close to 0; rest of parameters as in Fig. 5.1. Rest of plots show thruster performances

Chapter 6

EFFECTS OF HEAT CONDUCTION

6.1 Governing equations

Here we add the effect of heat conduction into the basic steady-state model treated in Ch. 3. Wall losses are neglected, i.e. $\tilde{\nu}_w = 0$. Again, for sake of clarity in the reading we give an almost complete account of the model equations.

We consider now the set of equations We consider the same stationary model of Chapter 3 but including heat conduction effects. The governing equations are

$$
\begin{aligned}
&\frac{d}{dx}(An_e v_{xi}) = \frac{d}{dx}(An_e v_{xe}) = -\frac{d}{dx}(An_n v_n) = An_e \nu_i,\\
&v_n = \text{const},\\
&\frac{1}{A}\frac{d}{dx}(Am_i n_e v_{xi}^2) = -en_e\frac{d\Phi}{dx} + m_i n_e \nu_i v_n,\\
&0 = en_e\frac{d\Phi}{dx} - \frac{dn_e T_e}{dx} - m_e \nu_d n_e v_{xe},\\
&\frac{1}{A}\frac{d}{dx}A\left(\frac{3}{2}T_e n_e v_{xe} + q_{xe}\right) = -n_e T_e \frac{dv_{xe}}{dx} + \nu_d n_e m_e v_{xe}^2 - \nu_i n_e \alpha_i E_i,\\
&\frac{dT_e}{dx} = -\frac{2m_e \nu_d}{5n_e T_e} q_{xe}.
\end{aligned}
\tag{6.1}
$$

6.1.1 Singular points and boundary conditions

Solving Eqs.(6.1) for the spatial derivatives we obtain again a matrix equation of the form of Eq.(5.11)

$$
(1 - M^2)\frac{d\boldsymbol{Y}}{dx} = \boldsymbol{F}(\boldsymbol{Y}), \quad \boldsymbol{Y} = (n_e, v_{xi}, T_e, ...), \tag{6.2}
$$

where now $\boldsymbol{Y} = (n_e, v_{xi}, T_e, q_{xe}, ...)$ groups 8 plasma variables, $\boldsymbol{F}$ is a regular function (different from the one in the zero conduction model), and M is the isothermal Mach number,

$$M = \frac{v_{xi}}{\sqrt{T_e/m_i}}.$$

For instance, the ion velocity follows Eq.(5.13),

$$\frac{dv_{xi}}{dx} = \nu_i - \frac{v_{xi}}{T_e}\frac{G}{1-M^2},$$

but now function G is

$$G = -\nu_d\left[m_e v_{xe} - \frac{2m_e q_{xe}}{5n_e T_e}\right] - \nu_i m_i(2v_{xi} - v_n) + m_i v_{xi}^2 \frac{d\ln A}{dx}. \tag{6.3}$$

The eight boundary conditions for this model are the seven ones of the no-conduction model plus a condition for the heat flow deposited by the electrons into the anode sheath (at point B), already discussed in Sec. 2.6. Summarizing, the eight boundary conditions for a solution with supersonic-exit are

i)-iv) $\dot{m}$, v_{nA} , T_{eP}, and $V_d = \Phi_A - \Phi_P$ are known.

v)-vii) At point B:

$$v_{xiB} = -\sqrt{T_{eB}/m_i},$$

$$\frac{e(\Phi_B - \Phi_A)}{T_{eB}} = \frac{e\Phi_{sh}}{T_{eB}} = \ln\frac{\bar{c}_{eB}}{4|v_{xeB}|} = \ln\left(\frac{\Gamma_{iB}}{\Gamma_{eB}}\sqrt{\frac{m_i}{2\pi m_e}}\right), \tag{6.4}$$

$$\frac{q_{xeB}}{n_{eB}v_{xeB}T_{eB}} = \frac{e\Phi_{sh}}{T_{eB}} - \frac{1}{2}.$$

viii) At point S one has $M_S = 1$ and $G_S = 0$, that is

$$\frac{m_i\nu_{iS}}{m_e\nu_{dS}} = \frac{\Gamma_d - \Gamma_{iS}}{2\Gamma_{iS}} + \frac{q_{xeS}A_c}{5T_{eS}\Gamma_{iS}} \quad \text{at} \quad v_{xiS} = \sqrt{\frac{T_{eS}}{m_i}}. \tag{6.5}$$

In dimensionless terms, Eq. (6.5) becomes

$$\eta_{iS}(1-\eta_{iS})\frac{m_i\nu_i^*}{m_e\nu_{dS}} = i_d - \eta_{iS} + \frac{2q_{xeS}A_c}{5T_{eS}\Gamma_m} \quad \text{with} \quad \nu_i^* = \frac{\Gamma_m}{v_n}R_{iS}, \tag{6.6}$$

which can be compared with the corresponding condition for the non-conduction problem, Eq. (3.16).

The presence of an additional differential equation for q_{xe} implies a new mathematical model, with a different sound velocity for the ion fluid and, therefore, different singular/sonic points. The consequence is that the model with heat conduction requires its own integration algorithms and cannot be solved from adding extra terms to the no-conduction model and performing a parametric continuation on solutions computed previously. nevertheless, the integration procedure tries to be similar to the non-conduction case. Independent integrations are launched from point S towards points B and P. As before, region BS poses the main restrictions to the existence of solutions. An additional difficulty now is that the solution launched from S must meet condition (6.4) on q_{xeB}, which requires iteration on the new 'initial' parameter q_{xeS}. Indeed, due to convergence problems, it is easier to launch solutions from points B and S and to match them in an intermediate point.

6.1.2 Restriction on the ion backflow

One new feature of the conduction model is the restriction of the relative ion back-flow, η_{iB}, to a narrow range. The matching of the quasineutral solution with the anode sheath requires (i) the anode sheath to be ion-attracting and (ii) the ion back-flow to accelerate towards the anode. The first condition means $\phi_{AB} > 0$. From Eq.(3.12), the second condition implies that $G_B > 0$ in Eq.(3.12), or, using Eq.(6.3) with $\nu_i \simeq 0$,

$$\left.\frac{2q_{xe}}{5n_eT_ev_{xe}}\right|_B < 1. \tag{6.7}$$

Using now Eqs. (3.11) and (2.61), the two conditions yield the double restriction

$$0 < \ln\frac{\bar{c}_{e_B}}{4|v_{xeB}|} < 3, \tag{6.8}$$

or, in terms of the ion back current,

$$5\cdot 10^{-3} < \frac{|I_{iB}|}{I_d} < 0.114, \tag{6.9}$$

with $I_i = en_iv_{xi}A_c$. However, difficulties found in the numerical convergence around point B near the limit $\phi_{AB} = 0$, have forced us to exchange that limit for the close one, $q_{xeB} = 0$, where $e\phi_{AB}/T_{eB} = 0.5$. This moves the lower bound of the ion back-current to $|I_{iB}|/I_d \sim 8\cdot 10^{-3}$.

6.2 Solution for zero-ionization regions

Since the ionization region is relatively thin, it is of interest to know how is the solution in the regions where ionization is negligible. Making $\nu_i = 0$ in Eqs.(6.1) one has

$$\begin{aligned} &An_\alpha v_\alpha = \text{const} \quad (\alpha = i, e, n),\\ &\frac{1}{2}m_iv_{xi}^2 + e\Phi = \text{const},\\ &\frac{5}{2}T_e - e\Phi + \frac{q_{xe}}{n_ev_{xe}} = \text{const},\\ &m_in_ev_{xi}\frac{dv_{xi}}{dx} + \frac{dn_eT_e}{dx} = -\nu_dm_en_ev_{xe}. \end{aligned} \tag{6.10}$$

These equations together with the equation for dT_e/dx yield a second order differential equation for T_e and $\hat{q}_{xe} = q_{xe}/n_ev_{xe}T_e$:

$$\begin{aligned} &\frac{1}{T_e}\frac{dT_e}{d\xi} = \hat{q}_{xe},\\ &\left(\frac{T_e}{m_iv_{xi}^2} - 1\right)\frac{d\hat{q}_{xe}}{d\xi} = 1 + \left(\frac{3}{5} - \frac{T_e}{m_iv_{xi}^2}\right)\hat{q}_{xe} + \frac{2}{5}\left(1 - \frac{T_e}{m_iv_{xi}^2}\right)\hat{q}_{xe}^2 + \frac{1}{A}\frac{dA}{d\xi},\\ &\frac{dx}{d\xi} = -\frac{T_e}{\nu_dm_ev_{xe}}. \end{aligned} \tag{6.11}$$

The (dimensionless) auxiliary variable ξ is used for convenience and to show the spatial scale of the problem.

The equation for $d\hat{q}_{xe}/d\xi$ shows that a regular sonic transition is possible now even without ionization. Sonic point S is regular if $G_S = 0$ becomes here

$$\hat{q}_{xeS} = \frac{5}{2}, \qquad \text{that is} \qquad q_{xeS} = \frac{5}{2}(n_e v_{xe} T_e)|_S, \tag{6.12}$$

a result that can be obtained from Eq.(6.5) also. Therefore, now, a regular sonic point can exist even in a region of negligible ionization. This is a novelty with respect to the non-conduction model.

A particular solution of these equations for $A = \text{const}$ is

$$T_e, \Phi = \text{const}, \quad v_{xi}, q_{xe} = 0, \tag{6.13}$$

which corresponds to the asymptotic behavior of the diffusion region, point C.

6.3 Plasma structure and thruster performances

Figure 4 shows the axial profiles of main plasma variables for an SPT-100 type of thruster. Design and control parameters are similar to the case of Fig. 3. The plasma structure presents similar trends to the no-conduction solution of Ref.[37] (with no lateral losses), but heat conduction smoothes the temperature profile in two ways: first, the peak temperature is reduced from about 90 eV to 65 eV; second there is a smoother transition between the diffusion and ionization regions, leading to a shorter diffusion region, and a larger ionization layer. The reduction in the maximum temperature is not enough to agree with experimental values where, for $V_d \sim 300$ V, maximum temperatures are in the range $20 - 30 eV$. Therefore, wall losses need to be considered still.

Plasma equations and boundary conditions seem to force an almost monotonic profile of q_{xe} between B and S. Then, the heat flux at point S, q_{xeS}, is large. In the present model, Eq. (6.3) shows that a regular sonic transition implies to balance Joule heating, conductive heat flow, and ionization losses. The large value of q_{xeS} means this balance to take place mainly between heat conduction and Joule heating,

$$q_{xe} \sim \frac{5}{2} n_e T_e v_{xe},$$

and, therefore, point S is outside (downstream, in fact) the ionization layer. In turn, the point of maximum temperature, where $q_{xe} = 0$, is going to be downstream of point S, what justifies that we could not find valid solutions with the point of maximum temperature well inside the channel.

For the case of Fig. 4, Fig. 5(a)-(c) measure different phenomena in the electron dynamics. This is aimed to evaluate the validity of the hypotheses supporting our model. Figure 5(a) shows the different contributions to the total collision frequency of electrons, Eq.(2.57). Bohm diffusion provides the main contribution from the ionization layer towards the exit, whereas e-i collisions (instead of the e-n collisions) dominate in the diffusion region. This last feature is justified by the high plasma density and low temperature there, and needs further investigation. Figure 5(b) shows the axial profiles of the ionization frequency, with its peak marking the ionization region, and the effective axial frequency for electron diffusion, Eq.(134); the dominance of Bohm diffusion makes $\nu_d \propto B(x)$, approximately, in most of the channel. Figure 5(c) shows that the electron mean azimuthal energy (main contribution to the electron mean kinetic energy) is totally negligible compared to the thermal energy, except perhaps within a small region near the anode.

Performance parameters for the case plotted in Fig. 4 are: $F \simeq 90.6$mN, $I_d \simeq 4.51$A, ($i_d = 1.17$), and $\eta \simeq 57.5\%$. The influence of the plasma discharge V_d and the magnetic field B_m on thruster performances have been computed from parametric continuation of the solution of Fig. 4. The consequence of the narrow interval for η_{iB} in Eq.(6.9), is a narrow range too of the control parameters where our model yields stationary solutions (with large ionization). As an example, Fig. 6(a) shows the band of of parameters (V_d, B_m), where solutions are found is dramatically small; only variations of about 10% are permitted. Figures 6(b)-6(d) plot the corresponding performance bands for thrust, discharge current, and efficiency; for F, the band reduces practically to a line. These plots show that larger thrust and efficiency are obtained with larger V_d and B_m.

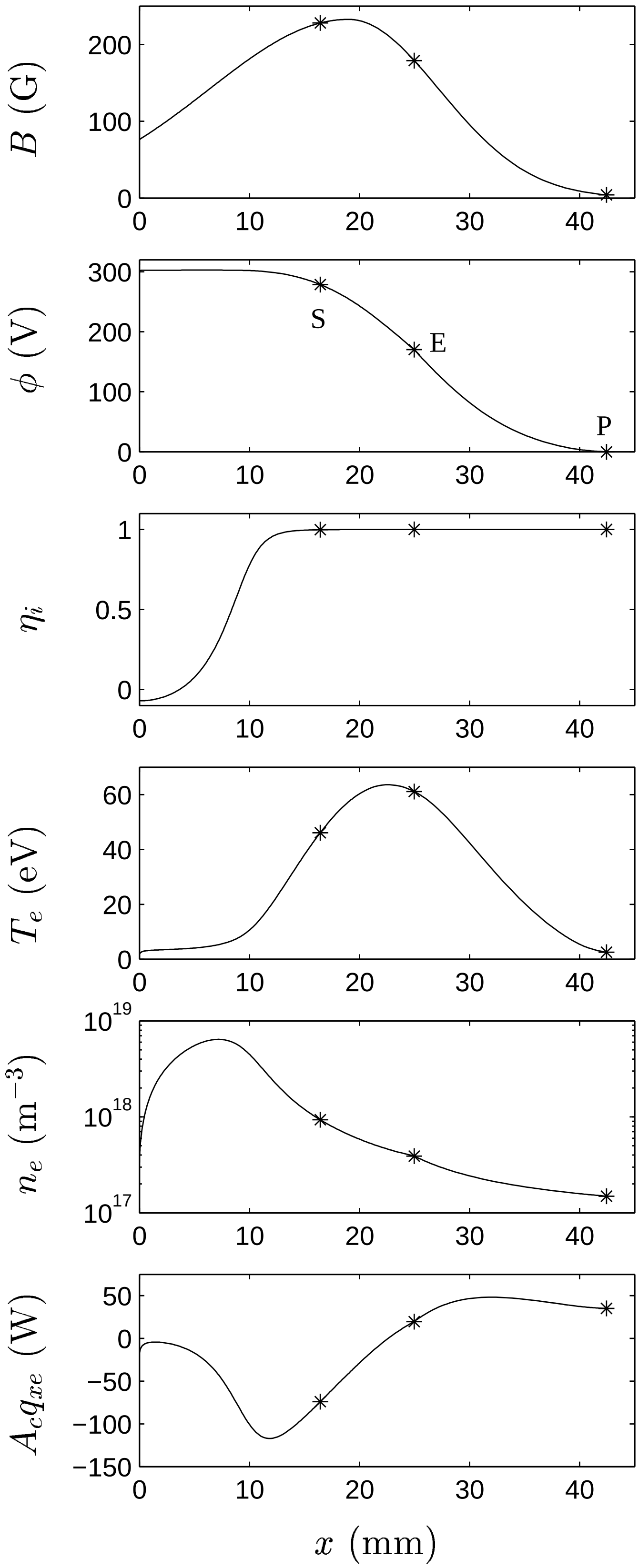

Figure 6.1: Model with heat conduction (and no wall losses). Axial structure of the plasma discharge for: $L = 25\text{mm}$, $L_{EP} = 21.1\text{mm}$, $A_c = 45\text{cm}^2$, $V_d = 300\text{V}$, $\dot{m} = 5.2\text{mg/s}$, $T_{eP} = 2.5\text{eV}$, $16\alpha_B \sim 0.067$.

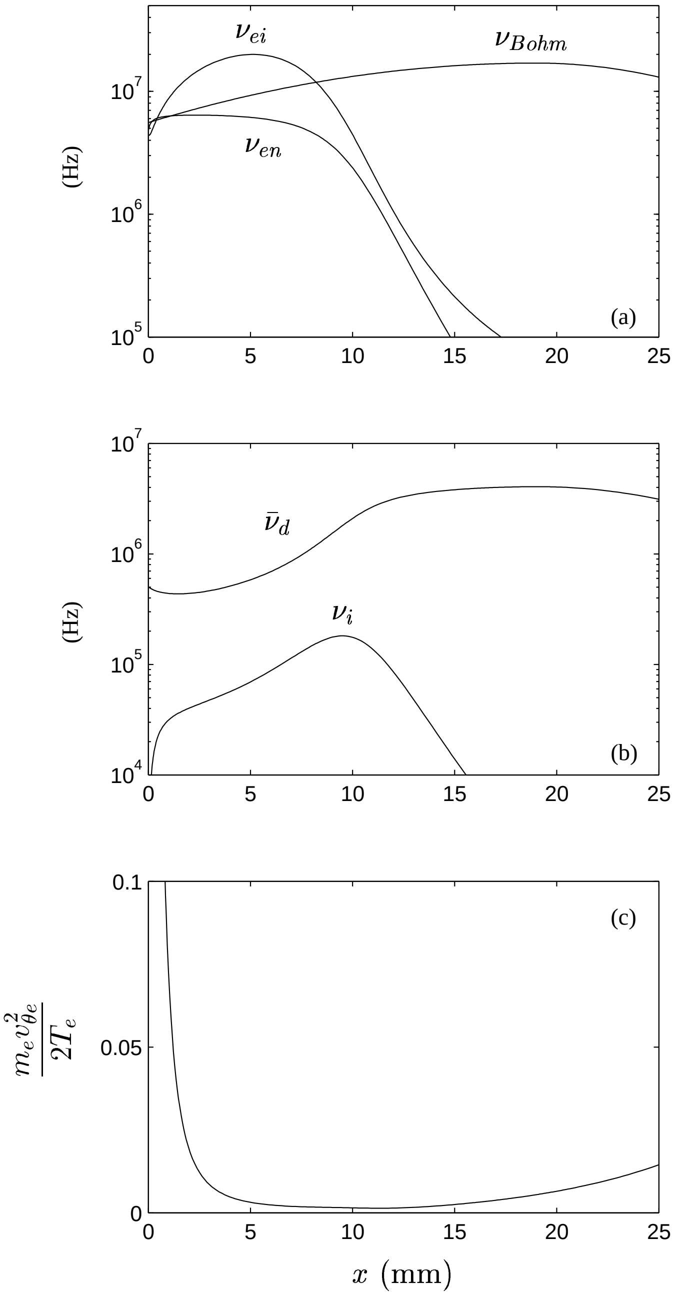

Figure 6.2: Model with heat conduction (and no wall losses). Same case of Fig. 5. (a) Contributions of different processes to the electron collision frequency ν_e. (b) Axial diffusion frequency ($\bar{\nu}_d = \nu_d\sqrt{m_e/m_i}$) and ionization frequency along the channel. (c) Ratio of electron mean kinetic energy to electron temperature.

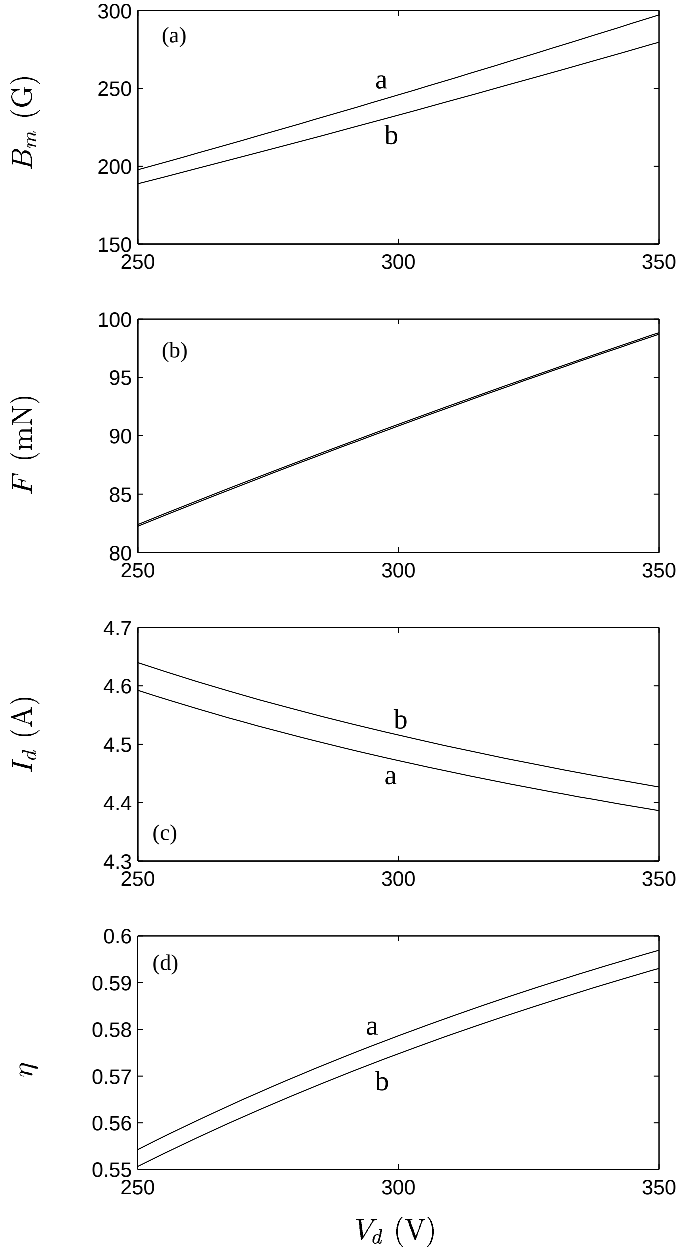

Figure 6.3: Model with heat conduction (and no wall losses). (a) Band of input parameters (V_d, B_m) where stationary solutions have been found; rest of parameters as in Fig. 4. Line 'a' corresponds to $G_B = 0$, and line 'b' to $\phi_{AB} = 0$. Bands for (b) thrust, (c) discharge current, and (d) efficiency, corresponding to the (V_d, B_m) band.

Chapter 7

SELF-OSCILLATIONS

7.1 Perturbation equations

The oscillatory behavior of Hall thrusters is here approached by investigating the stability of the steady-state plasma structure studied in previous chapters. The linear stability analysis is based in the plasma response to small temporal perturbations. Equations and results are presented here for the no-conduction model with wall losses of Chap. 5.

Since temporal derivatives affect to the perturbation terms only, it is convenient to solve plasma equations (2.55) for the spatial derivatives. This yields

$$
\begin{aligned}
&P\frac{\partial h_e}{\partial x} = G \qquad (h_e \equiv \ln n_e),\\
&\frac{\partial v_{xi}}{\partial x} = -v_{xi}\frac{\partial h_e}{\partial x} + \nu_i - \nu_w - v_{xi}\frac{\partial a}{\partial x} - \frac{\partial h_e}{\partial t},\\
&\frac{\partial v_{xe}}{\partial x} = -v_{xe}\frac{\partial h_e}{\partial x} + \nu_i - \nu_w - v_{xe}\frac{\partial a}{\partial x} - \frac{\partial h_e}{\partial t},\\
&\frac{\partial T_e}{\partial x} = -m_i v_{xi}\frac{\partial v_{xi}}{\partial x} - T_e\frac{\partial h_e}{\partial x} - \nu_d m_e v_{xe} + \nu_i m_i (v_n - v_{xi}) - m_i\frac{\partial v_{xi}}{\partial t},\\
&e\frac{\partial \phi}{\partial x} = \frac{\partial T_e}{\partial x} + T_e\frac{\partial h_e}{\partial x} + \nu_d m_e v_{xe},\\
&n_n v_n\frac{\partial v_n}{\partial x} = -n_n\frac{\partial v_n}{\partial t} + n_e\nu_w (v_{xi} - v_n),\\
&v_n\frac{\partial n_n}{\partial x} = -n_n\frac{\partial v_n}{\partial x} - n_e(\nu_i - \nu_w) - n_n v_n\frac{\partial a}{\partial x} - \frac{\partial n_n}{\partial t},
\end{aligned}
\tag{7.1}
$$

with

$$
\begin{aligned}
P &= T_e - \frac{3}{5} m_i v_{xi}^2, \\
\bar{G} \equiv v_{xe} G &= \nu_i \Big[\frac{2}{5}\alpha_i E_i + T_e - \frac{3}{5} m_i v_{xe}(2v_{xi} - v_n)\Big] - \nu_d m_e v_{xe}^2 + \Big(\frac{3}{5} m_i v_{xe} v_{xi} - T_e\Big)\nu_w \\
&+ \frac{2}{5}\nu_{we} T_e + \frac{3}{5} m_i v_{xi}^2 v_{xe} \frac{\partial a}{\partial x} + \frac{3}{5} m_i v_{xe}\Big(v_{xi}\frac{\partial h_e}{\partial t} - \frac{\partial v_{xi}}{\partial t}\Big) + \frac{3}{5}\frac{\partial T_e}{\partial t} - \frac{2}{5} T_e \frac{\partial h_e}{\partial t}.
\end{aligned}
\tag{7.2}
$$

The equation for the area variation in the plume must be added:

$$
v_{xi}\frac{\partial a}{\partial x} = \begin{cases} 0, & x < L, \\ 2c_p/d, & L < x, \end{cases}
\tag{7.3}
$$

with $a = \ln d$.

7.2 Model of linear perturbations

To be definite, let us assume a small perturbation in the channel discharge voltage,

$$
V_d(t) = V_{d0} + \Re\Big\{V_{d1}\mathrm{e}^{-\mathrm{i}\omega t}\Big\},
$$

with $V_{d1} \ll V_{d0}$ and $\omega = \omega_{re} + \mathrm{i}\omega_{im}$ the (complex) frequency of the perturbation mode. Then, in the linear approximation, the plasma response is

$$
Y(x,t) \simeq Y_0(x) + \Re\Big\{Y_1(x;\omega)\exp(-\mathrm{i}\omega t)\Big\},
$$

with $Y(x,t)$ the vector of plasma variables, $Y_0(x)$ the solution obtained from the stationary model of Chapter 5 (subscript 0 is added now to stationary variables), and $Y_1(x;\omega)$ the linear perturbation response, which is proportional to V_{d1}.

From the expansion of Eqs.(7.1) and the substitution

$$
\partial/\partial t \to -\mathrm{i}\omega,
$$

the linear equations for each perturbation mode in ω are

$$
\begin{aligned}
P_0 v_{xe0}\frac{\partial h_{e1}}{\partial x} &= \bar{G}_1 - \Big(P_0 v_{xe1} + P_1 v_{xe0}\Big)\frac{\partial h_{e0}}{\partial x}, && (7.4)\\
\frac{\partial v_{xi1}}{\partial x} &= -v_{xi1}\frac{\partial h_{e0}}{\partial x} - v_{xi0}\frac{\partial h_{e1}}{\partial x} + \nu_{i1} - \nu_{w1} - v_{xi1}\frac{\partial a_0}{\partial x} - v_{xi0}\frac{\partial a_1}{\partial x} + \mathrm{i}\omega h_{e1}, && (7.5)\\
\frac{\partial v_{xe1}}{\partial x} &= -v_{xe0}\frac{\partial h_{e1}}{\partial x} - v_{xe1}\frac{\partial h_{e0}}{\partial x} + \nu_{i1} - \nu_{w1} - v_{xe1}\frac{\partial a_0}{\partial x} - v_{xe0}\frac{\partial a_1}{\partial x} + \mathrm{i}\omega h_{e1}, && (7.6)\\
\frac{\partial T_{e1}}{\partial x} &= -m_i v_{xi1}\frac{\partial v_{xi0}}{\partial x} - m_i v_{xi0}\frac{\partial v_{xi1}}{\partial x} - T_{e1}\frac{\partial h_{e0}}{\partial x} - T_{e0}\frac{\partial h_{e1}}{\partial x} && (7.7)\\
&\quad + \nu_{i1} m_i(v_{n0} - v_{xi0}) + \nu_{i0} m_i(v_{n1} - v_{xi1}) - \nu_{d1} m_e v_{xe0} - \nu_{d0} m_e v_{xe1} + \mathrm{i} m_i \omega v_{xi1}, && (7.8)\\
\frac{\partial e\phi_1}{\partial x} &= \frac{\partial T_{e1}}{\partial x} + T_{e0}\frac{\partial h_{e1}}{\partial x} + T_{e1}\frac{\partial h_{e0}}{\partial x} + m_e(\nu_{d0} v_{xe1} + \nu_{d1} v_{xe0}), && (7.9)
\end{aligned}
$$

$$n_{n0}v_{n0}\frac{\partial v_{n1}}{\partial x} = -(n_{n0}v_{n1} + n_{n1}v_{n0})\frac{\partial v_{n0}}{\partial x} \tag{7.10}$$

$$+ (n_{e1}\nu_{w0} + n_{e0}\nu_{w1})(v_{xi0} - v_{n0}) + n_{e0}\nu_{w0}(v_{xi1} - v_{n1}) + \mathrm{i}\omega n_{n0}v_{n1}, \tag{7.11}$$

$$v_{n0}\frac{\partial n_{n1}}{\partial x} = -v_{n1}\frac{\partial n_{n0}}{\partial x} - n_{n0}\frac{\partial v_{n1}}{\partial x} - n_{n1}\frac{\partial v_{n0}}{\partial x} - n_{e0}(\nu_{i1} - \nu_{w1}) \tag{7.12}$$

$$- n_{e1}(\nu_{i0} - \nu_{w0}) - (n_{n1}v_{n0} + n_{n0}v_{n1})\frac{\partial a_0}{\partial x} - n_{n0}v_{n0}\frac{\partial a_1}{\partial x} + \mathrm{i}\omega n_{n1}, \tag{7.13}$$

with

$$P_1 = T_{e1} - \frac{6}{5}m_i v_{xi0}v_{xi1}, \tag{7.14}$$

$$\begin{aligned}\bar{G}_1 = {} & -\nu_{d1}m_e v_{xe0}^2 - 2\nu_{d0}m_e v_{xe1}v_{xe0} + \nu_{i0}\Big[T_{e1} - \frac{3}{5}m_i v_{xe1}(2v_{xi0} - v_{n0}) - \frac{3}{5}m_i v_{xe0}(2v_{xi1} - v_{n1})\Big] \\ & + \nu_{i1}\Big[\frac{2}{5}\alpha_i E_i + T_{e0} - \frac{3}{5}m_i v_{xe0}(2v_{xi0} - v_{n0})\Big] + \Big(\frac{3}{5}m_i v_{xe0}v_{xi1} + \frac{3}{5}m_i v_{xe1}v_{xi0} - T_{e1}\Big)\nu_{w0} \\ & + \Big(\frac{3}{5}m_i v_{xe0}v_{xi0} - T_{e0}\Big)\nu_{w1} + \frac{2}{5}\nu_{we1}T_{e0} + \frac{2}{5}\nu_{we0}T_{e1} + \frac{3}{5}m_i v_{xi0}^2 v_{xe0}\frac{\partial a_1}{\partial x} \\ & + (\frac{6}{5}m_i v_{xi1}v_{xi0}v_{xe0} + \frac{3}{5}m_i v_{xi0}^2 v_{xe1})\frac{\partial a_0}{\partial x} + \mathrm{i}\omega\Big[\frac{3}{5}m_i v_{xe0}(v_{xi1} - h_{e1}v_{xi0}) - \frac{3}{5}T_{e1} + \frac{2}{5}T_{e0}h_{e1}\Big],\end{aligned} \tag{7.15}$$

plus the equation for the area variation

$$v_{xi0}\frac{\partial a_1}{\partial x} = \begin{cases} 0, & x < L, \\ -(a_1 v_{xi0} + v_{xi1})\dfrac{\partial a_0}{\partial x} + 2\dfrac{c_{p1}}{a_0} & L < x \end{cases} \tag{7.16}$$

with $a_0 = \ln d_0$, $d_1 = d_0 a_1$. Finally, the linear expansions for ν_{d1}, ν_{i1}, ν_{w1}, and ν_{we1} must be added to these equations.

7.2.1 Boundary conditions

Like the stationary equations, the perturbation equations are singular at $P_0 = 0$. The appropriate set of seven boundary conditions for the perturbation problem is:

i)-iv) $\dot{m}_{1A}$, v_{n1A}, T_{e1P}, and $\phi_{1P} = -V_{d1}$ are known.

v) To fulfill $h_{e1B} \ll h_{e0B}$, the singularity at point B for the perturbed response cannot be of higher order than for the stationary response. Therefore, it must be

$$P_{1B} = 0. \tag{7.17}$$

vi) Taking $\phi_{1A} = 0$, from Eq.(3.11), the perturbation of the sheath potential is

$$e\phi_{1B} = e\phi_{0B}\frac{T_{e1B}}{T_{e0B}} + T_{e0B}\Big(\frac{\Gamma_{i1B}}{\Gamma_{i0B}} - \frac{\Gamma_{e1B}}{\Gamma_{e0B}}\Big). \tag{7.18}$$

vii) For the perturbed solution to be regular at point S, the right side of Eq.(7.4) must be zero. Considering that $P_{0S} = G_{0S} = 0$, the regularity condition at point S is

$$0 = \Big[\bar{G}_1 - P_1 v_{xe0}\frac{\partial h_{e0}}{\partial x}\Big]_S \equiv \bar{G}_{1S} - P_{1S}\frac{\partial \bar{G}_0/\partial x|_S}{\partial P_0/\partial x|_S}. \tag{7.19}$$

7.2.2 Integration procedure

The perturbation of point S, x_{S1}, is part of the solution. From the expansions of $P_S = 0$ and $G_S = 0$, one has

$$x_{S1} = -\frac{P_{1S}}{\partial P_0/\partial x|_S} = -\frac{\bar{G}_{1S}}{\partial \bar{G}_0/\partial x|_S}. \tag{7.20}$$

The compatibility of these two relations is assured by condition (7.19).

The perturbation of the discharge current, Γ_{d1}, is part of the solution also. It satisfies

$$\Gamma_{i1}(x) - \Gamma_{e1}(x) = \Gamma_{d1} = \text{const}, \tag{7.21}$$

However, the mass flow perturbation changes along the channel,

$$\Gamma_{i1}(x) + \Gamma_{n1}(x) = \Gamma_{m1}(x) \neq \text{const}.$$

The numerical integration of this perturbation problem is performed again with a Runge-Kutta algorithm from point S towards points B and E. However, there appear new, delicate issues in the region BS, related to singular points B and S. These are

1) To obtain the spatial derivatives of perturbed variables at point S requires to know the second derivatives of G_0 and P_0.

2) These second derivatives must be used now on the 0th order solution as well, for a smooth matching of the spatial profiles in the vicinity of point S.

3) A perturbation solution launched from point S is unbounded (i.e. tends to infinity) at point B. Therefore, it must be stopped before point B and be matched to an independent solution launched from point B, at an intermediate point (here chosen as $M_0 = -0.2$). This increases the number of 'fundamental modes' (each one proportional to a 'fundamental parameter') constituting the general solution, but, since the problem is linear, it avoids completely any subsequent iteration.

The solution of the perturbation problem is thus written in the form

$$Y_1(x) = \sum_j c_{1j} Y_{1j}(x) + \sum_l b_{1l} Y_{1l}(x), \tag{7.22}$$

where

$$C_1 \equiv [c_{11}, ..., c_{19}] = [n_{e1S}, n_{n1S}, v_{xe1S}, v_{n1S}, n_{e1S}, \phi_{1S}, n_{e1B}, v_{xe1B}, T_{e1B}\ ] \tag{7.23}$$

is a vector of unknown parameters, $[b_{11}, b_{12}] = [v_{n1A}, \Gamma_{m1A}]$ are known parameters, and Y_{1j} and Y_{1l} constitute eleven 'fundamental modes', which depends on $\tilde{\omega}$ and the vector $\tilde{C}_0$ of parameters defining the stationary solution (tildes mean dimensionless magnitudes).

Next we impose the continuity of the solution at the intermediate point and the values T_{e1P} and ϕ_{1P} for the temperature and the potential at point P. In total, these constitute nine linear relations that we can write in the form

$$MC_1 = B_1, \tag{7.24}$$

where: B_1 includes five zeros and the perturbations of four control parameters: v_{n1A}, Γ_{m1A}, T_{e1P} and ϕ_{1P}; and M is a square matrix, obtained from the fundamental modes, which depends on $\tilde{\omega}$ and $\tilde{C}_0$.

7.3 Self-excited modes

Linear self-excited modes are singular solutions of the perturbation problem for homogeneous boundary conditions, i.e. $B_1 = 0$. The frequencies of the self-excited modes are the solutions of the global dispersion relation

$$D(\tilde{\omega}; \tilde{C_0}) \equiv \det M = 0. \tag{7.25}$$

The self-excited modes are unstable if $\tilde{\omega}_{im} > 0$.

Fig. 7.1 shows the frequencies of the main five self-excited modes corresponding to the steady-state solution of Fig. 5.1. Notice that only Mode 1 is unstable for this case. Self-excited modes are difficult to obtain since the zeros of $detD$ are very sharp. This makes advisable to solve both $D_{re} = 0$ and $D_{im} = 0$ instead of just $detD = 0$; indeed, Noguchi[41] failed to find unstable modes because he used this last method.

The five self-frequencies of Fig. 7.1 are:

– Mode 0: $\omega(\text{kHz}) = 0 - 7.2\text{i}7.2$
– Mode 1: $\omega(\text{kHz}) = 45.2 + 17.2\text{i}$
– Mode 2: $\omega(\text{kHz}) = 142.3 - 23.2\text{i}$
– Mode 3: $\omega(\text{kHz}) = 51.7 - 75.3\text{i}$
– Mode 4: $\omega(\text{kHz}) = 119.5 - 90.4\text{i}$

Figures 7.2-7.8 show the spatial profiles of some perturbation variables for the five modes, and contour plots for Modes 1 and 2. These two modes seem to be the main ones with respect to stability (Mode 2 has been found unstable for other steady-state solutions). The five self-excited modes present several similarities. First, in all modes, unstable and stable, perturbations are stronger in the ionization layer. This is the consequence of spatial gradients being larger there. Large ionization fluctuations are found also in the dynamic response to regular perturbations, –that is solutions with $B_1 \neq O$ in Eq. (7.24)–. Therefore, ionization waves should not be considered the mark characterizing self-excited modes, as suggested by some people. Other common features of self-excited modes are that ion and neutrals acoustic waves are launched in both directions within the subsonic region of the channel, whereas the acceleration region and the plume seem to have a minor role in the dynamic response.

Contour plots in Figs. 7.4 and 7.6 show that neutral perturbations are forward traveling waves (indeed they are standing waves mounted on the stationary neutral flow), while ion perturbations form a backward traveling wave. Electron perturbations are controlled by quasineutrality and fulfill Eq. (7.21). The main differences between Modes 1 and 2 are observed in the wavelengths and phase velocities of the ion and neutral waves. This seems to indicate that the self-excitation is related to the coupling between ionization and acoustic waves in the diffusion region, with a secondary role for the acceleration region. However, further work is necessary to understand the sequence of mechanisms that feed the self-excited modes.

Figures 7.9-7.11 show the influence of B_m, V_d and $\dot{m}$ in the self-frequency of Mode 1. Relative variations are of order one and the instability persists in the parametric range shown there. No general conclusions should be drawn, from this particular case, about the stabilizing or unstabilizing effect of those parameters.

Finally, the comparison of self-excited modes of steady-state solutions with and without wall losses does not show significant differences.

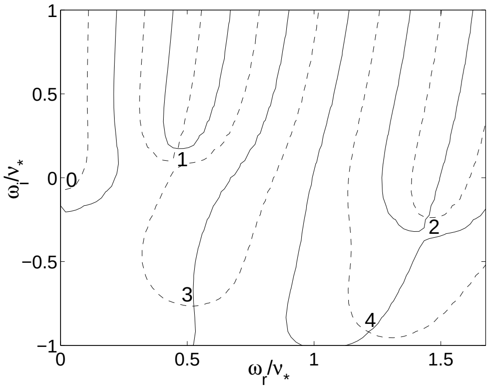

Figure 7.1: First self-excited modes for the stationary solution of Fig. 3.2. Solid lines: $D_{re} = 0$; dash-dot lines: $D_{im} = 0$. Modal frequencies are given by the intersection of both lines Dashed lines are contour lines for $|D|$ constant and small.

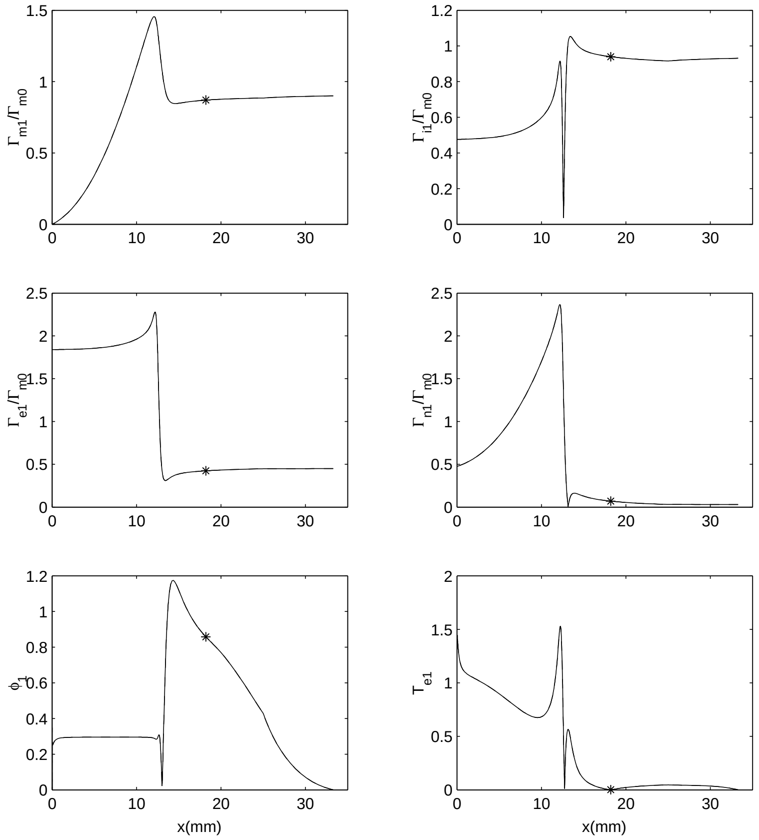

Figure 7.2: Mode 0 (of Fig. 7.1): Spatial profiles of different perturbation magnitudes [say $\boldsymbol{Y}_1(x,t) = \boldsymbol{Y}_1(x)\exp(-\mathrm{i}\omega_1 t)$] normalized with $\Gamma_{d1}/\Gamma_{d0} = 1$. Solid line: envelope of perturbation amplitude [i.e. $|\boldsymbol{Y}_1(x)|$]; Dashed line: perturbation at a fixed time [i.e. $|\Re\{\boldsymbol{Y}_1(x)\}|$]

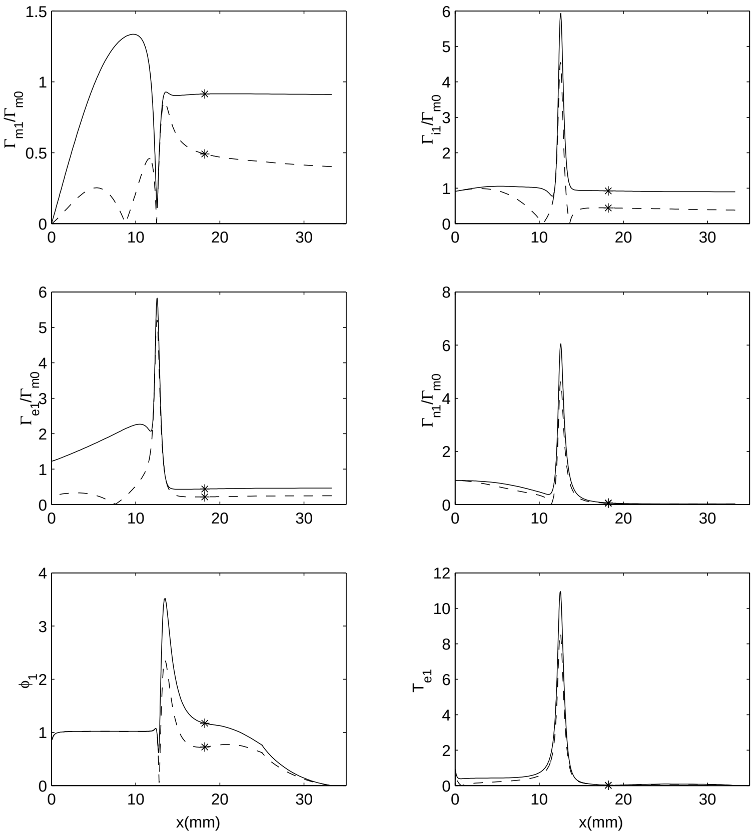

Figure 7.3: Mode 1 (of Fig. 7.1): spatial profiles for $\Gamma_{d1}/\Gamma_{d0} = 1$.

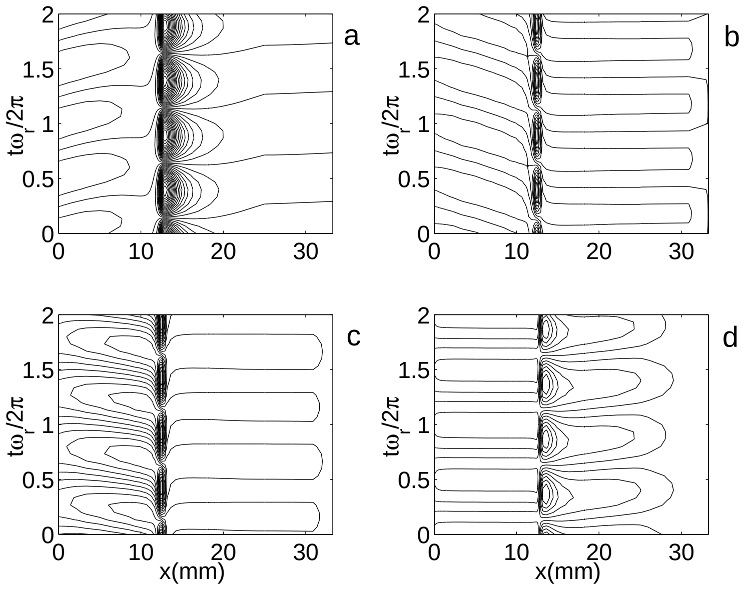

Figure 7.4: Mode 1: Contour plots of (a) n_n1, (b)Γ_{i1}, (c)Γ_{e1}, and (d)ϕ_1.

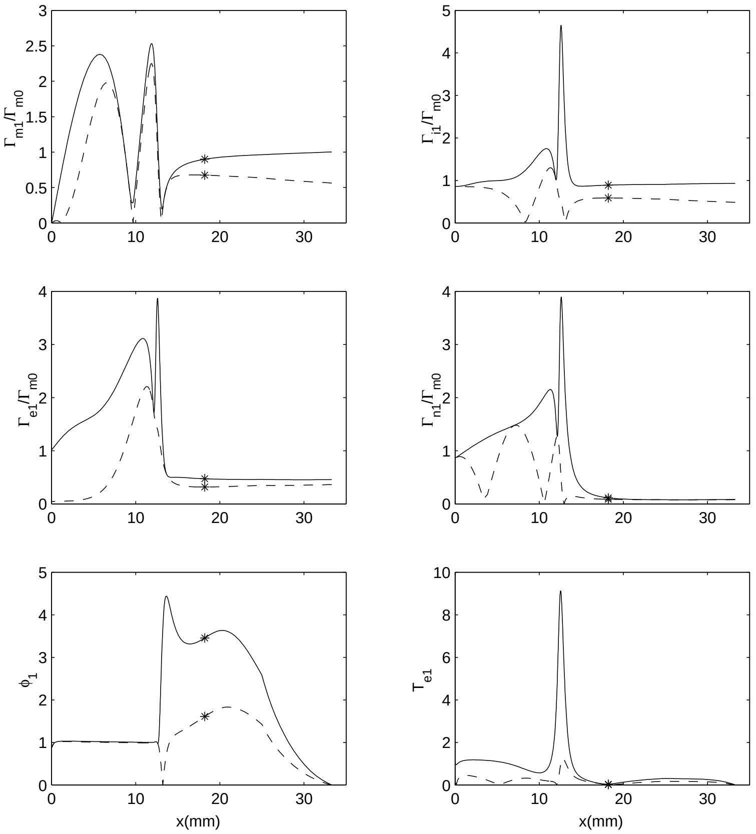

Figure 7.5: Mode 2: spatial profiles for $\Gamma_{d1}/\Gamma_{d0} = 1$.

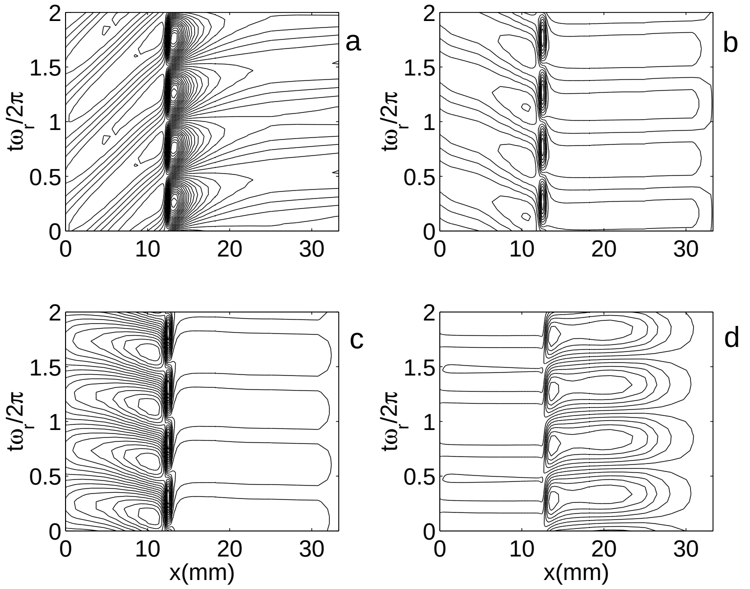

Figure 7.6: Mode 2: Contour plots of (a) n_n1, (b)Γ_{i1}, (c)Γ_{e1}, and (d)ϕ_1. .

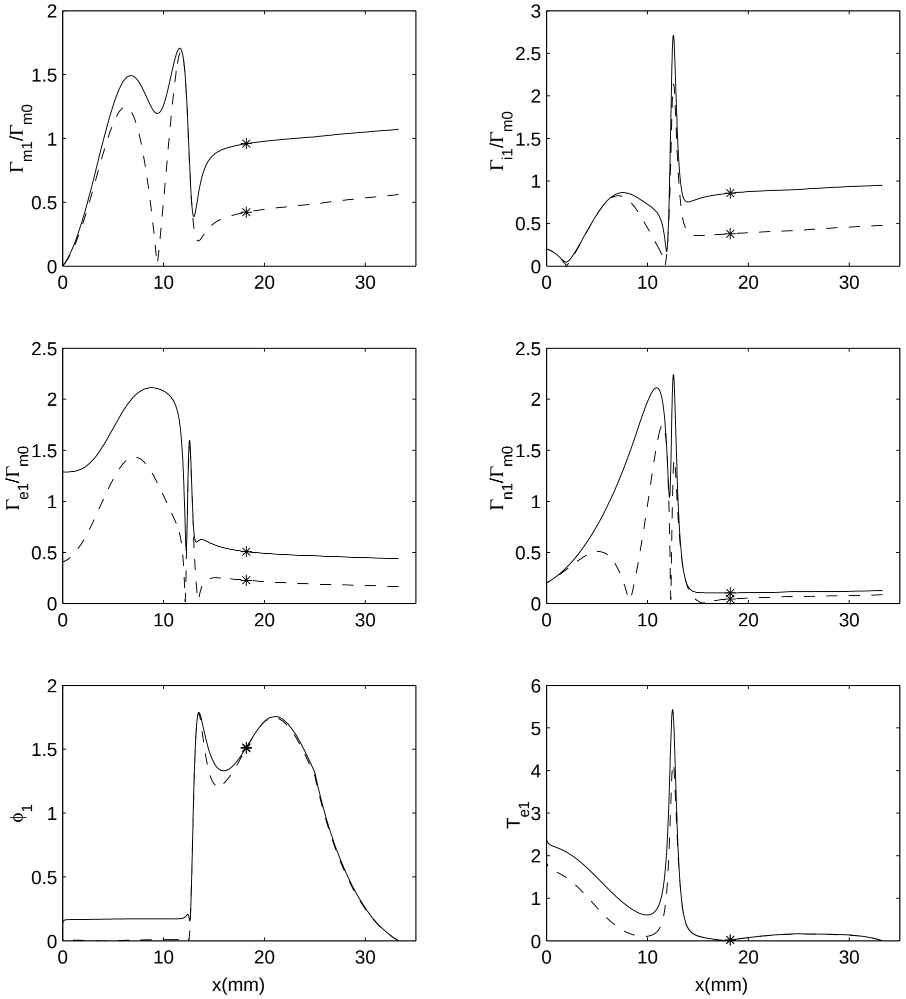

Figure 7.7: Mode 3: spatial profiles for $\Gamma_{d1}/\Gamma_{d0} = 1$.

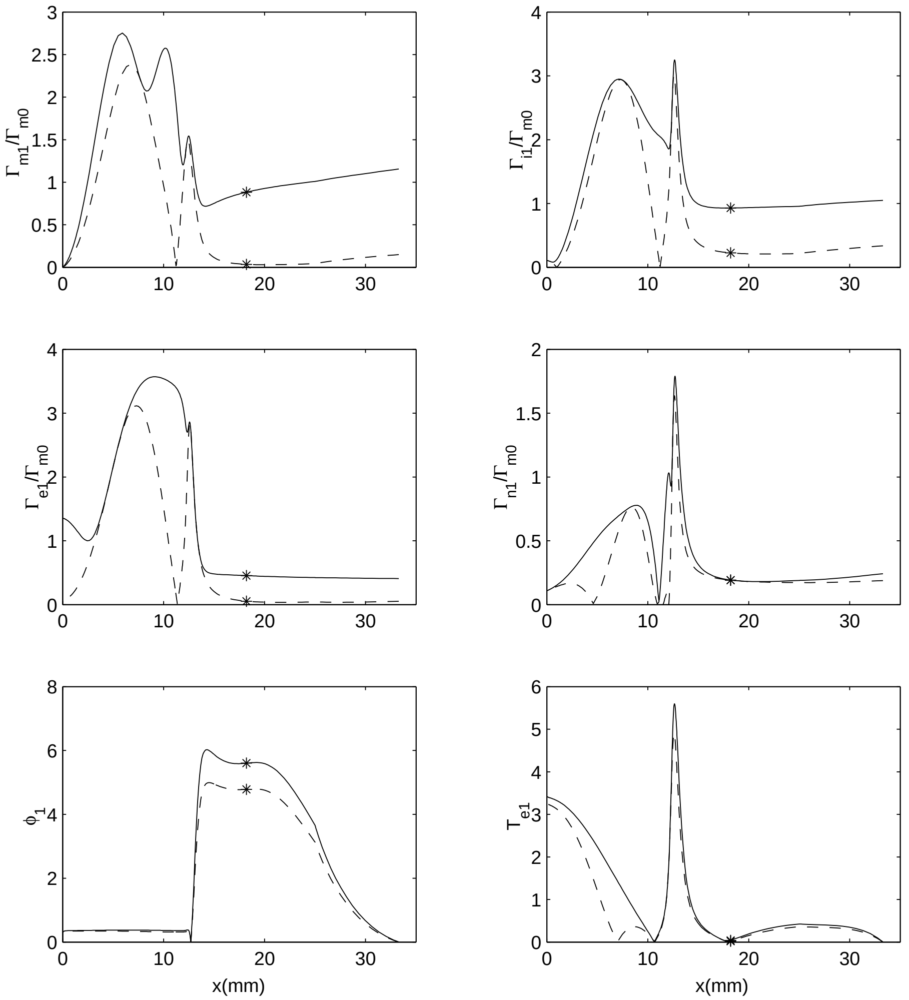

Figure 7.8: Mode 4: spatial profiles for $\Gamma_{d1}/\Gamma_{d0} = 1$.

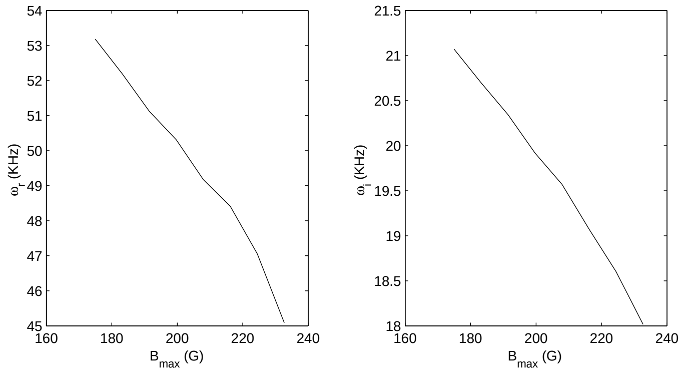

Figure 7.9: Evolution of the complex frequency of Mode 1 with B_m. The rest of 0th order parameters as in Fig. 3.2.

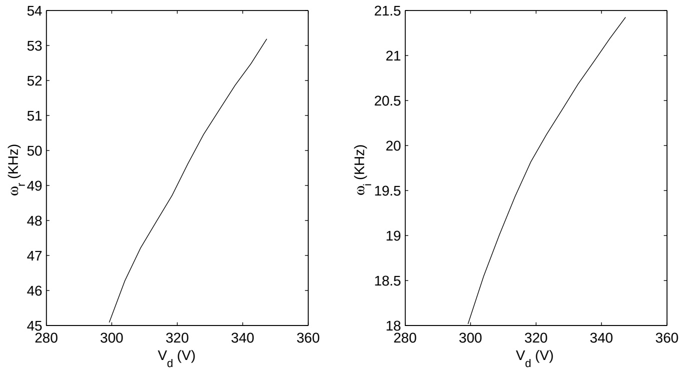

Figure 7.10: Evolution of the complex frequency of Mode 1 with V_d. The rest of 0th order parameters as in Fig. 3.2.

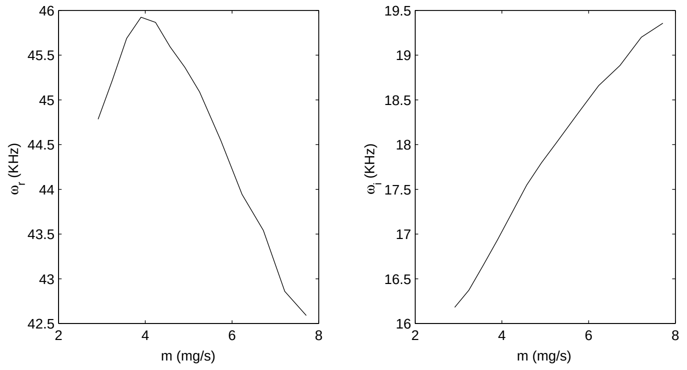

Figure 7.11: Evolution of the complex frequency of Mode 1 with $\dot{m}$. The rest of 0th order parameters as in Fig. 3.2.

Chapter 8

SUMMARY

This work has presented, through successive stages grouped in Chaps. 2 to 7, a semi-analytical macroscopic model of the plasma discharge in a Hall thruster. In Chap. 2 we have formulated the general model for the plasma discharge both inside the thruster and in the near-plume. Plasma equations, collisional processes, simplifying hypotheses, spatial scales, and other issues have been discussed and evaluated.

Chapter 3 presents what can be called the 'core model', which ignores electron heat conduction and the interaction of the plasma with the channel lateral walls. Since both thruster channel, near-plume, and neutralizer are included in the model, we could analyze the complete response of the plasma in terms of actual control/design parameters. The main achievement of the core model is the reproduction of the different regions of the rich plasma structure observed experimentally, and the understanding of many of the discharge basic physics. Other accomplishments here have been (i) to show that optimum operation conditions correspond to solutions with an internal sonic transition, and (ii) to find that the domain where stationary solutions exist is limited.

In Chap. 4 we discussed a radial model for the interaction of the plasma with the dielectric walls of the thruster channel. The model includes, in a consistent way, wall-emitted, plasma-trapped electrons, explains the transition to a regime with charge-saturated sheaths, and solves the presheath/sheath radial structure totally. Finally, losses of plasma current and energy, and gains in electron azimuthal momentum (leading to near-wall conductivity), in the channel, have been evaluated.

Chapters 5 and 6 were dedicated to improve the core model. In Chap. 5 we included the effects of the radial plasma/wall interaction into the axial model. Results obtained until now show very large losses of plasma current and energy, unless some mechanism, not well identified yet, inhibits the radial fluxes to the walls. On the contrary, near-wall conductivity is found marginal, for inhibited flows, at least. However, few cases have been run still and further research is needed before reliable conclusions can be formulated.

In Chap. 6 we modified the core model by considering heat conduction effects (but radial interaction was ignored). The differences in the mathematical formulation for the heat-conduction model has required to adapt the integration procedure. The new stationary solutions present smoother temperature profiles, more according to experimental ones, but heat conduction is found insufficient by itself to reduce the peak temperature to experimental values. The general plasma structure is maintained with a shorter diffusion region and the sonic transition away from the ionization layer outer bound. Finally, the most worrying conclusion of this conductive model is the dramatic reduction in the parametric domain of stationary solutions (of known ones, at least).

In Chap. 7 we undertook a linear stability analysis of the steady-state plasma structure. The analysis is classical but the formulation and solving of the perturbation model is rather sophisticated due to the rich stationary structure and the presence of singular points. Longitudinal self-excited modes, some of them are stable and other ones unstable, are found in the same frequency range than experiments (10-100 kHz), Self-oscillations are far from being simple and well understood. They consist of local ionization waves and ion and neutral acoustic waves counter-traveling along the subsonic part of the channel. Coupling of the different fundamental waves takes place at the ionization layer and the anode sheath, and through collisional processes. Electron perturbations are governed by quasineutrality, and the regions of supersonic acceleration, including the plume, have a marginal role in these modes. An unfinished parametric investigation have not shown ways to reduce effectively the unstable modes yet.

Different parts of this work have been presented in recent International Conferences and published in technical papers and in Physics of Plasmas [42, 37, 43, 36, 44].

Future research should deal with:

1) A model of radial interaction with partial-trapping of secondary emission and cylindrical effects. Partial-trapping is expected to obstruct charge-saturation of the radial sheath and, therefore, to reduce energy losses. Cylindrical effects should produce an asymmetry between the two thruster walls with possible effects on electron trapping and flow inhibition.

2) A unified model with heat conduction and losses at lateral walls. This means to add the radial model of Chap. 4 (or an improved version) into the conductive model of Chap. 6.

3) A comparative study of the results of these 1D macroscopic models with those of 2D PIC-based models. This comparison could provide relevant clues to evaluate and improve both types of models and to use them in combination for thruster design and analysis.

4) Progresses in the study of thruster oscillations. This should include both a better understanding of the unstable modes, and investigation of whether the parametric domain with no stationary solutions corresponds to thruster oscillatory behaviors observed experimentally.

Appendix A

Expansion around sonic points

A.1 Stationary model

A.1.1 Singular sonic point

At a singular sonic point one has $P_0 = 0$ and $G_0 \neq 0$. Around this point and for $\partial/\partial t = 0$, Eqs.(7.1) yield the expansion

$$\begin{aligned} G_0 dx &= P_0 dh_{e0}, \\ dh_{e0} &= -dv_{xi0}/v_{xi0}, \\ dT_{e0} &= (T_{e0}/v_{xi0} - m_i v_{xi0}) dv_{xi0}. \end{aligned}$$

Taking v_{xi0} as independent variable, and differentiating once more, one has

$$d^2 x \simeq \frac{8}{5G_0} dv_{xi0}^2, \tag{A.1}$$

and the velocity profile around the singular point is

$$\Delta v_{xi0} = \sqrt{\frac{5}{4} G_0 \Delta x}. \tag{A.2}$$

The profiles of T_{e0} and h_{e0} are obtained from the above linear relations with v_{xi0}. From Eq.(A.2), a valid spatial solution with points B and S singular, must have $\bar{G}_B < 0$ and $\bar{G}_S > 0$.

A.1.2 Regular sonic point

In a regular point S, one has $\bar{G}_{0S} = 0$ and $P_{0S} = 0$, so the derivatives of the plasma variables in Eqs.(7.1) are not determined and the numerical integration cannot proceed directly from point S. To determine them, it is convenient to use the auxiliary variable ξ defined by

$$\lambda dx/d\xi \equiv \lambda x' = P_0 v_{xe0}, \tag{A.3}$$

with λ any constant. Then, the equation for h'_{e0} in Eqs.(7.1) becomes (for $A(x) = \text{const}$ around point S)

$$\lambda h'_{e0} = \bar{G}_0 \tag{A.4}$$

and Eqs.(7.1) can be written as

$$
\begin{aligned}
v'_{xi0} &= -v_{xi0}h'_{e0} + \nu_{i0}x', && \text{(A.5)}\\
T'_{e0} &= -m_i v_{xi0}v'_{xi0} - T_{e0}h'_{e0} + m_i\Big(\nu_{i0}(v_{n0}-v_{xi0}) - \nu_{d0}m_e v_{xe0}\Big)x', && \text{(A.6)}\\
v'_{xe0} &= -v_{xe0}h'_{e0} + \nu_{i0}x', && \text{(A.7)}\\
e\phi'_0 &= T'_{e0} + T_{e0}h'_{e0} + m_e\nu_{d0}v_{xe0}x', && \text{(A.8)}\\
v'_{n0} &= 0, && \text{(A.9)}\\
v_{n0}n'_{n0} &= -n_{e0}\nu_{i0}x'. && \text{(A.10)}
\end{aligned}
$$

Notice that point S is now a 'stationary point' of the above equations in ξ.

The expansion of the RHS of Eqs. (A.3) and (A.4) around point S is

$$
\lambda x' \simeq T'_{e0} - \frac{6}{5}m_i v_{xi0}v'_{xi0} + \text{HOT}, \tag{A.11}
$$

$$
\begin{aligned}
\lambda h'_{e0} \simeq{}& \frac{3}{5}m_i(\nu_{w0}-2\nu_{i0})v_{xe0}v'_{xi0} + (\nu_{i0}-\nu_{w0}+\frac{2}{5}\nu_{we0})T'_{e0} - m_e v^2_{xe0}\nu'_{d0}\\
&+\left[\frac{3}{5}m_i v_{xe0}(v_{n0}-2v_{xi0}) + \frac{2}{5}\alpha_i E_i + T_{e0}\right]\nu'_{i0} + \left(\frac{3}{5}m_i v_{xi0}v_{xe0} - T_{e0}\right)\nu'_{w0} + \frac{2}{5}T_{e0}\nu'_{we0} + \text{HOT},
\end{aligned} \tag{A.12}
$$

or, in matrix notation,

$$
\lambda\begin{bmatrix} x' \\ h'_{e0}\end{bmatrix} \simeq M_1\begin{bmatrix} v'_{xi0} \\ T'_{e0}\end{bmatrix} + M_2\begin{bmatrix}\nu'_{i0}\\ \nu'_{d0}\\ \nu'_{w0}\\ \nu'_{we0}\end{bmatrix} + \text{ HOT.} \tag{A.13}
$$

The derivatives of the diverse frequencies can be written, in matrix form, as

$$
\begin{bmatrix}\nu'_{i0}\\ \nu'_{d0}\\ \nu'_{w0}\\ \nu'_{we0}\end{bmatrix} = M_3\begin{bmatrix} x' \\ h'_{e0}\end{bmatrix} + M_4\begin{bmatrix} v'_{xi0} \\ T'_{e0}\end{bmatrix}. \tag{A.14}
$$

Then, Eqs. (A.5)-(A.6) provide a matrix relation

$$
\begin{bmatrix} v'_{xi0} \\ T'_{e0}\end{bmatrix} = M_5\begin{bmatrix} x' \\ h'_{e0}\end{bmatrix}. \tag{A.15}
$$

Neglecting now HOT in Eq. (A.13), one has, at point S,

$$
\lambda\begin{bmatrix} x' \\ h'_{e0}\end{bmatrix} = A\begin{bmatrix} x' \\ h'_{e0}\end{bmatrix}, \tag{A.16}
$$

with

$$
A \equiv \begin{bmatrix} a & b \\ c & d\end{bmatrix} = (M_1 + M_2M_4)M_5 + M_2M_3. \tag{A.17}
$$

The two possible slopes of $dh_{e0}/x'|_S$ correspond to the eigenvectors of matrix A. These eigenvectors are real for

$$(a-d)^2 + 4bc \geq 0, \tag{A.18}$$

so only the parametric domain verifying this condition must be studied.

A.2 Perturbation model

A.2.1 Singular sonic point

To depart from point B, the quantity

$$Y'_1 \equiv P_0 v_{xe0} \frac{\partial Y_1}{\partial x}\bigg|_{E,B}$$

must be known, which means to solve the indetermination P_1/P_0 in Eq.(7.4). Expanding the perturbation equations, the problem reduces to solve three linear equations for h'_{e1}, v'_{xe1}, and T'_{e1},

$$h'_{e1} = \bar{G}_1 - \Big(\frac{v_{xe1}}{v_{xe0}} + \frac{T'_{e1} - \frac{6}{5}v_{xi0}v'_{xi1} - \frac{6}{5}v'_{xi0}v_{xi1}}{T'_{e0} - \frac{6}{5}v_{xi0}v'_{xi0}}\Big)\bar{G}_0, \tag{A.19}$$

$$v'_{xi1} = -v_{xi1}\bar{G}_0 - v_{xi0}h'_{e1}, \tag{A.20}$$

$$T'_{e1} = -v_{xi1}v'_{xi0} - v_{xi0}v'_{xi1} - T_{e1}\bar{G}_0 - T_{e0}h'_{e1}, \tag{A.21}$$

with

$$v'_{xi0} = -v_{xi0}\bar{G}_0, \qquad T'_{e0} = (v^2_{xi0} - T_{e0})\bar{G}_0. \tag{A.22}$$

A.2.2 Regular sonic point

Equations need to be expanded twice to determine

$$Y'_1 = \partial Y_1/\partial x|_S.$$

Differentiating in Eq. (5.5) for h_{e0}, one has

$$P_0 v_{xe0} h''_{e0} + P'_0 v_{xe0} h'_{e0} + P_0 v'_{xe0} h'_{e0}, = \bar{G}'_0 \quad [182] \tag{A.23}$$

and, particularizing at point S,

$$P'_{0S} v_{xe0S} h'_{e0S} = \bar{G}'_{0S}. \tag{A.24}$$

Differentiating in Eq.(A.23) and particularizing at point S, one has

$$2P'_{0S} v_{xe0S} h''_{e0S} = \bar{G}''_{0S} - (P''_{0S} v_{xe0S} + 2P'_{0S} v'_{xe0S})h'_{e0S} \tag{A.25}$$

Finally, differentiating Eq.(7.4),

$$\begin{aligned} &P_0 v_{xe0} h''_{e1} + P'_0 v_{xe0} h'_{e1} + P_0 v'_{xe0} h'_{e1} = \\ &\quad \bar{G}'_1 - (P_0 v_{xe1} + P_1 v_{xe0}) h''_{e0} - (P'_0 v_{xe1} + P'_1 v_{xe0} + P_0 v'_{xe1} + P_1 v'_{xe0}) h'_{e0} \end{aligned}$$

and particularizing at point S, one has

$$P'_{0S} v_{xe0S} h'_{e1S} = \bar{G}'_{1S} - P_{1S} v_{xe0S} h''_{e0S} - (P'_{0S} v_{xe1S} + P'_{1S} v_{xe0S} + P_{1S} v'_{xe0S}) h'_{e0S}. \qquad \text{(A.26)}$$

Equations for P'_0, P''_0, $\bar{G}'_0$, $\bar{G}''_0$, P'_1, and $\bar{G}'_1$ include first and second derivatives of the different plasma variables. Once all the equations are added we have three set of linear equations to determine Y'_{0S}, Y''_{0S}, and Y'_{1S}.

Bibliography

[1] A.M. Bishaev and V. Kim. Local plasma properties in a Hall-current accelerator with and extended acceleration zone. *Sov. Physics-Tech. Physics*, 23(9):1055–1057, 1978.

[2] G. Guerrini, C. Michaut, M. Dudeck, A.N. Vesselovzorov, and M. Bacal. Characterization of plasma inside the SPT-50 channel by electrostatic probes. In *25th International Electric Propulsion Conference, Cleveland, OH*, IEPC Paper No. 97-053. Electric Rocket Propulsion Society, Cleveland, Ohio, 1997.

[3] J.M. Haas and A.D. Gallimore. Characterization of the internal plasma structure of a 5kw Hall thruster. In *26th International Electric Propulsion Conference, Kytakyushu, Japan*, IEPC Paper No. 99-078. Electric Rocket Propulsion Society, Cleveland, Ohio, 1999.

[4] J.M. Fife and M. Martínez-Sánchez. Two-dimensional hybrid particle-in-cell (PIC) modelling of Hall thrusters. In *24th International Electric Propulsion Conference, Moscow, Russia*, IEPC Paper No. 95-240. Electric Rocket Propulsion Society, Cleveland, Ohio, 1995.

[5] V. Kim. Main physical features and processes determining the performance of stationary plasma thrusters. *J. Propulsion Power*, 14(5):736–743, 1998.

[6] J. M. Fife. *Hybrid-PIC Modeling and Electrostatic Probe Survey of Hall Thrusters.* PhD thesis, Massachusetts Institute of Technology, 1998.

[7] J. J. Szabo. *Fully kinetic numerical modeling of a plama thruster.* PhD thesis, Massachusetts Institute of Technology, 2001.

[8] C.A. Lentz and M. Martínez-Sánchez. Transient one dimensional numerical simulation of Hall thrusters. In *29th Joint Propulsion Conference, Monterey, CA*, AIAA Paper No. 93-2491. American Institute of Aeronautics and Astronautics,Washington, DC, 1993.

[9] K. Komurasaki, K. Mikami, and Y. Arakawa. Two-dimensional numerical model of plasma flow in a Hall thruster. *J. Propulsion Power*, 11(6):1317–1323, 1995.

[10] A. Fruchtman and N.J. Fisch. Modelling the Hall Thruster. In *34th Joint Propulsion Conference, Cleveland, OH*, AIAA Paper No. 98-3500. American Institute of Aeronautics and Astronautics,Washington, DC, 1998.

[11] J.P. Boeuf and L. Garrigues. Low frequency oscillations in a stationary plasma thruster. *J. Applied Physics*, 84(7):3541–3554, 1998.

[12] E. Ahedo and M. Martínez-Sánchez. One-dimensional plasma structure in Hall thruster. In *34th Joint Propulsion Conference, Cleveland, OH*, AIAA Paper No. 98-8788. American Institute of Aeronautics and Astronautics,Washington, DC, 1998.

[13] M. Martínez-Sánchez, E. Ahedo, and R. Noguchi. Linear 1-D analysis of oscillations in Hall thrusters. In *26th International Electric Propulsion Conference, Kitakyushu, Japan*, IEPC Paper No. 99-105. Electric Rocket Propulsion Society, Cleveland, Ohio, 1999.

[14] D. Rapp and W.E. Francis. Charge exchange between gaseous ions and atoms. *Journal of Chemical Physics*, 37(11):2631–2645, 1962.

[15] R.J. Goldston and P.H. Rutherford. *Introduction to Plasma Physics.* Institute of Physics Publishing, Bristol, 1995.

[16] D.L. Book. *Plasma Formulary.* Naval research Laboratory, Washington, 1986.

[17] A.I. Morozov, Y.V. Esipchuk, G.N. Tilinin, A.V. Trofimov, Y.A. Sharov, and G.Y.Shchepkin. Plasma accelerator with closed electron drift and extended acceleration zone. *Soviet Physics-Tech. Physics*, 17(1):38–45, 1972.

[18] N.B. Meezan and M.A. Capelli. Electron density measurements for determining the anomalous electron mobility in a coaxial Hall discharge plasma. In *36th Joint Propulsion Conference, Huntsville, AL*, AIAA Paper No. 2000-3420. American Institute of Aeronautics and Astronautics,Washington, DC, 2000.

[19] J.V. Dugan and R.J. Sovie. Volume ion production costs in tenuous plasmas: A general atom theory and detailed results for helium, argon, and cesium. Technical report, NASA TN D-4150, ??

[20] J.A. Bittencourt. *Fundamentals of Plasma Physics.* Pergamon, Oxford, 1986.

[21] M. Keidar and I.D. Boyd. Effect of a magnetic field on the plasma plume from Hall thrusters. *J. Applied Physics*, 86(9):4786–4791, 1999.

[22] J.E. Pollard and E.J. Beiting. Ion energy ion velocity, and thrust vector measurements for the SPT-140 Hall thruster. In *SP-465: 3rd Spacecraft Propulsion Conference, Cannes(Francia)*, pages 789–796, Noordwijk, The Netherlands, 2000. European Space Agency.

[23] D. Rapp and P. Englander-Golden. Total cross sections for ionization and attachment in gases by electron impact. I. Positive ionization. *J. Chemical Physics*, 43:1464–1479, 1965.

[24] D. Mathur and C. Badrinathan. Ionization of xenon by electrons: Partial cross sections for single, double, and triple ionization. *Physical Review A*, 35:1033–1042, 1987.

[25] J.M. Sankovic, J.A. Hamley, and T.W. Hang. Performance evaluation of the russian spt-100 thruster at nasa lerc. In *24th International Electric Propulsion Conference, Moscow, Russia*, IEPC Paper No. 93-094. Electric Rocket Propulsion Society, Cleveland, Ohio, 1993.

[26] R.M. Myers and D.H. Manzella. Stationary Plasma Trhuster Plume Characteristics. In *23rd International Electric Propulsion Conference, Seattle, WA*, IEPC Paper No. 93-096. Electric Rocket Propulsion Society, Cleveland, Ohio, 1993.

[27] F. Darnon. The SPT-100 plasma plume and ist interaction with a spacecraft, from modeling to ground and flight characterization. In *36th Joint Propulsion Conference, Huntsville, AL*, AIAA Paper No. 2000-3525. American Institute of Aeronautics and Astronautics,Washington, DC, 2000.

[28] Y. Raitses, J. Ashkenazy, and G. Appelbaum. Experimental investigation of the effect of channel material on Hall thruster characteristics. In *25th International Electric Propulsion Conference, Cleveland, Ohio*, IEPC Paper No. 97-056. Electric Rocket Propulsion Society, Cleveland, Ohio, 1997.

[29] J.M. Fife, M. Martínez-Sánchez, and J. Szabo. A Numerical Study of Low-Frequency Discharge Oscillations in Hall Thrusters. In *33rd Joint Propulsion Conference, Seattle, WA*, AIAA Paper No. 97-3052. American Institute of Aeronautics and Astronautics,Washington, DC, 1997.

[30] J.M. Fife and S. Locke. Influence of channel insulator material on Hall thruster discharges: a numerical study. AIAA Paper No. 2001-1137. American Institute of Aeronautics and Astronautics, Washington, DC, 2001.

[31] K.F. Stephens and C.A. Ordonez. Sheath and presheath potentials for anode, cathode and floating plasma-facing surfaces. *J. Appl. Physics*, 85:2522–2527, 1999.

[32] L. Jolivet and J.-F. Roussel. Effects of the secondary electron emission on the sheath phenomenon in a Hall thruster. In *3rd Int. Conference on Spacecraft propulsion, Cannes.* ESA/CNES, 2000.

[33] A.I. Bugrova, A.I. Morozov, and V.K.Kharchevnikov. Experimental investigation of near wall conductivity. *Sov. J. Plasma Physics*, 16(12):849–856, 1990.

[34] J.T. Scheuer and G.A. Emmert. A fluid treatment of the plasma presheath for collisionless and collisional plasmas. *Physics of Fluids B*, 2:445–451, 1990.

[35] L. Tonks and I. Langmuir. A general theory of the plasma of an arc. *Physical review*, 34:876–922, 1929.

[36] E. Ahedo, P. Martínez-Cerezo, and M. Martínez-Sánchez. Model of plasma-wall interaction effects in a Hall thruster. In *37th Joint Propulsion Conference, Salt Lake City, UT*, AIAA Paper No. 2001-3323. American Institute of Aeronautics and Astronautics,Washington, DC, 2001.

[37] E. Ahedo, P. Martínez-Cerezo, and M. Martínez-Sánchez. One-dimensional model of the plasma flow in a Hall thruster. *Physics of Plasmas*, 8:3058–3068, 2001.

[38] Jr. W. Hargus, J. M. Fife, L. Mason, R. Jankovsky, T. Haag, L. Pinero, and J.S. Snyder. Preliminary Performance Results of the High Performance Hall System SPT-140. In *36th Joint Propulsion Conf., Huntsville, Alabama*, number AIAA Paper No. 2000-3250. American Institute of Aeronautics and Astronautics,Washington, DC, 2000.

[39] J.M. Sankovic, T.W. Haag, and D.H. Manzella. Operating characteristics of the russian D-55 thruster with anode layer. In *30th Joint Propulsion Conference, Indianapolis, IN*, AIAA Paper No. 94-3011. American Institute of Aeronautics and Astronautics,Washington, DC, 1994.

[40] S. Béchu, C. Pérot, N. Gascon, P. Lasgorceix, A. Hauser, and M. Dudeck. Operating mode investigation of a laboratory stationary plasma thruster. In *35th Joint Propulsion Conference, Los Angeles, CA*, AIAA Paper No. 99-2567. American Institute of Aeronautics and Astronautics,Washington, DC, 1999.

[41] Reid A. Noguchi. Linear 1-d analysis of oscillation instabilities in stationary plasma thrusters. Master's thesis, Massachusetts Institute of Technology, 1999.

[42] E. Ahedo, P. Martínez-Cerezo, and M. Martínez-Sánchez. 1-D performance analysis of a Hall thruster. In *SP-465: 3rd Spacecraft Propulsion Conference, Cannes(Francia)*, pages 323–330, Noordwijk, The Netherlands, 2000. European Space Agency.

[43] E. Ahedo, P. Martínez-Cerezo, J.M. Gallardo, and M. Martínez-Sánchez. Modelling the plasma flow in a Hall thruster. In *7th Spacecraft Charging Technology, Noodrwijk, The Netherlands*, Noordwijk, The Netherlands, 2001. European Space Agency.

[44] E. Ahedo, P. Martínez-Cerezo, J.M. Gallardo, and M. Martínez-Sánchez. Characterization of the plasma in a Hall thruster. In *27th International Electric Propulsion Conference, Pasadena, CA*, IEPC Paper No. 01-17. Electric Rocket Propulsion Society, Cleveland, OH, 2001.